Hematite-breccia Hosted Iron Oxide Copper-Gold Deposits Require Magmatic Fluid Components Exposed to Atmospheric Oxidation: Evidence from Prominent Hill, Gawler Craton, South Australia

Journal Article

Author(s):
Schlegel, Tobias U.; Wagner, Thomas; Wälle, Markus; Heinrich, Christoph A. (iD)

Hematite-breccia hosted iron oxide–copper–gold deposits require magmatic fluid components exposed to atmospheric oxidation:
Evidence from Prominent Hill, Gawler craton, South Australia

Tobias U. Schlegel[1],*, Thomas Wagner[2], Markus Wälle[1],# and Christoph A. Heinrich[1,3]

[1]Institute of Geochemistry and Petrology, ETH Zürich, 8092 Zürich, Switzerland
[2]Institute of Applied Mineralogy and Economic Geology, RWTH Aachen University, Germany
[3]Also at: Faculty of Mathematics and Natural Sciences, University of Zürich, Switzerland

Corresponding author: Tobias U. Schlegel

* Present address: Institute of Applied Mineralogy and Economic Geology
RWTH Aachen University
Wüllnerstrasse 2, 52062 Aachen, Germany
E-Mail: tobias.schlegel@emr.rwth-aachen.de
Phone: +49 241 8095566

Present address: CREAIT, CRC and CFI Services (CCCS)
Memorial University of Newfoundland and Labrador
    230 Elizabeth Ave, St Johns NL, Canada A1C5S7

Abstract

The Prominent Hill deposit is a large iron oxide Cu–Au (IOCG) resource located in the Olympic IOCG province of South Australia. The deposit is hosted by brecciated sedimentary rocks and structurally underlying lavas of the ca. 1.6 Ga old Gawler Range Volcanics. Both rock units are altered and mineralized, forming characteristic hematite breccias. They are located in the footwall of the Southern Overthrust separating the host rock package in the footwall from Paleoproterozoic metasedimentary rocks in the hanging wall. The metasedimentary rocks were intruded by the Hiltaba Suite granites, which are co-magmatic with the Gawler Range Volcanics and show widespread magnetite-rich alteration. Economic mineralization was formed through a two-stage process. Early pyrite and minor chalcopyrite were deposited from moderately reduced fluids during sulfide stage I and are hosted in subeconomic magnetite skarns and in the brecciated sedimentary host rocks. This pre-ore stage was overprinted by the economically important stage II sulfides, deposited from hypogene, oxidized fluids ultimately sourced from the paleo-surface. The high-grade Cu ores contain dominantly chalcocite, bornite, chalcopyrite and gangue minerals including fluorite, barite and minor quartz, hosting mineralization-related fluid inclusion assemblages.
Petrography, microthermometry and LA-ICP-MS microanalysis were used to characterize pre-, syn- and post-mineralization fluid inclusion assemblages. The results permit discrimination

of four fluid end-members (A, B, C and D). Fluid A is the main ore fluid and hosted in fluorite and barite intergrown with Cu-sulfides in the breccia matrix. It is weakly saline (≤ 10 wt.% eqv. NaCl) and contains low concentrations of K, Pb, Cs, and Fe (600 ppm), but is rich in Cu (1000 ppm) and U (0.5–40 ppm). A magmatic origin of the salinity is supported by the low molar Br/Cl ratio of 0.003. We suggest that the solute inventory was derived from shallow fluid exsolution and degassing of late Gawler Range Volcanics, and subsequent complete oxidation of the fluid via contact with atmospheric oxygen. Fluid A migrated through oxidized aquifers to the site of the Prominent Hill deposit, where it became the main driver of stage II copper mineralization. Fluid B occurs in fluid inclusions in siderite + quartz-bearing veins crosscutting the hematite breccia. It is the most saline fluid with a total NaCl + CaCl$_2$ concentration of 36 to 45 wt.% and a low Ca/Na mass ratio of 0.3. Fluid B is rich in K, Fe, Pb, and Cs, and contains modest Cu (~70 ppm). Its composition is typical of a moderately reduced magmatic-hydrothermal brine, modified by fluid–rock interaction. Fluid C is hosted by fluid inclusions in fluorite and barite within bornite + chalcocite bearing ores. It is a calcic-sodic brine with 16–28 wt.% NaCl + CaCl$_2$ and has an elevated Ca/Na (0.6) and high Br/Cl ratios characteristic of basin brines of residual bittern origin. It is quite rich in Cu (~200 ppm), and likely contributed metals to economic mineralization. Fluid D is hosted by inclusions in fluorite in late veins crosscutting the hematite breccia. The total NaCl + CaCl$_2$ salinity ranges between 19 and 30 wt.%, and the concentrations of K, Mn, Cs and Pb are similar to those of fluid C. Fluid D is a basement brine with characteristically high Ca/Na ratios of around 2 and contains modest Cu (~100 ppm).

The high-grade copper mineralization in the Prominent Hill deposit originated dominantly from magmatic components, including both the metal inventory (Cu, minor Au and U) and sulfur. The essential factor controlling the high-grade IOCG mineralization was wholesale oxidation of magmatic Cu and S from Gawler Range Volcanic eruptions: volcanic gases reacted with atmospheric oxygen at or near the Earth's surface, for example in an acidic volcanic lake environment. Oxidized surface fluids charged with Cu, U and sulfate and high acidity then infiltrated the host rocks at Prominent Hill and became reduced by ferrous iron in residual magmatic brine, in non-magmatic basin brine and by ferrous iron-bearing minerals. Copper sulfides and hematite precipitated in a zone of fluid mixing, and by interaction of the fluids with acid-neutralizing host rock strata. Limited sulfide for the low-sulfidation ore mineral assemblage was supplied, to presently unknown proportions, from magmatic-hydrothermal pyrite derived in a pre-ore stage of mineralization and from magmatic sulfate reduced by aqueous Fe^{2+} to precipitate hematite.

Exploration-relevant factors for Prominent Hill style high-grade copper ores are the combination of (1) active volcanism during the late stages of the Gawler Range Volcanic Province, (2) a fluid mixing interface between deep brines and an acidic, surface-oxidized but magmatically-charged water as the main ore fluid, and (3) a mappable gradient of acid neutralization in brecciated and chemically reactive host rocks, ideally containing carbonates and some earlier pyrite.

1. Introduction

Iron oxide copper–gold (IOCG) deposits are large, commonly breccia-hosted orebodies containing tens of percent of magnetite or hematite, with variable amounts of copper, gold, uranium and rare-earth elements. Their greatest economic attraction for mineral exploration is the generally high grade of copper, ranging between 0.2 and 4.0 wt.% (on average 1 wt.%), compared to 0.2 to 1.5 wt.% (on average 0.5 wt.%) in porphyry Cu deposits (Williams et al., 2005; Singer et al., 2008, Sillitoe, 2010). In addition, IOCG deposits may contain significant co-product metals such as gold, silver and particularly uranium. Therefore, IOCG deposits rank among the largest and richest copper, uranium and gold resources (Souza and Vieira, 2000; Williams et al., 2001; Marschik and Fontboté, 2001; Mark et al. 2006; Ehrig et al., 2012). Deposits of this broadly-defined ore deposit type share aspects of mineral association (e.g. oxidized but low sulfidation assemblages) and geological environment (continental setting with felsic

magmatism; Hitzman et al., 1992; Williams et al., 2005; 2010; Barton, 2014). However, two central questions regarding their origin have not been answered satisfactorily: (1) how are tens of percent and commonly massive magnetite or hematite introduced and precipitated in the ore, as the defining characteristic of IOCG deposits; and (2) why do only some iron oxide-rich deposits contain high but variable concentrations of economic metals such as Cu, Au, U, and/or REE. The chemical characteristics, the sources and the flow paths of the mineralizing fluids must hold the key to understanding the formation and location of IOCG deposits (Williams and Skirrow, 2000; Sillitoe, 2003; Williams et al., 2010).

The presence of complex Na–Ca brines appears to be a major difference between IOCG deposits and porphyry–epithermal systems (Barton 2014; Heinrich and Candela, 2014), and calcic-sodic alteration may be a connecting feature in areas where both deposit types are associated (e.g. Yerington, Nevada; Dilles et al., 2000). Published fluid inclusion data and mineralogical evidence indicate that ore-forming IOCG fluids include oxidized, variably saline, generally sulfide-poor, and commonly Na–Ca–K–Fe- and/or CO_2-rich brines (Hitzman et al., 1992; Oreskes and Einaudi, 1992; Barton and Johnson, 1996; Pollard, 2000; Williams et al., 2005; Chiaradia et al., 2006; Davidson et al., 2007; Dreher et al., 2008; Chen, 2013; Barton, 2014). Questions concerning IOCG-mineralizing fluids need to address the origin of their complex salinity, and the source(s), transporting conditions and precipitation reactions of Fe and Cu as well as of Au and U that are enriched in the ores. Regarding the origin of salinity, essentially all possible scenarios have been proposed: highly saline fluids may be of (1) magmatic origin (Pollard, 2000; 2006; Sillitoe, 2003; Chiaradia et al., 2006), (2) evaporitic origin via halite dissolution or derived from residual bittern brines (Haynes et al., 1995; Barton and Johnson, 1996; Dilles et al., 2000; Xavier et al., 2008), or (3) metamorphic origin by leaching of meta-evaporites at high temperatures (Oliver, 1995; Barton and Johnson, 1996; Fisher and Kendrick, 2008). Interaction of multiple fluid types has been suggested as critical in IOCG ore formation, including mixing of magmatic brines with evaporite-reacted surface fluids (Haynes et al., 1995; Baker et al., 2006; 2008; Benavides et al., 2007), or mixing of magmatic fluids or other deep-sourced fluids with variably evolved sedimentary basin brines or seawater (Oreskes and Einaudi, 1990; Dilles et al., 2000; Skirrow and Walshe 2002; Bastrakov et al., 2007; Davidson et al., 2007; Kendrick et al., 2007; Baker et al., 2008; de Haller and Fontboté, 2009). The presence of distinctly Ca-bearing brines was observed in numerous microthermometric studies of fluid inclusions in IOCG deposits (e.g. summaries in Chen, 2010; Williams et al., 2010; Barton, 2014), but salinity data have been typically reported as NaCl equivalent (eqv.), limiting their quantitative interpretation in terms of fluid–rock reactions and fluid mixing trends.

The Olympic Dam deposit, arguably the world's largest metallic orebody and mined for Cu, Au and U, gave its name to the Olympic IOCG province located in the Archean to Proterozoic Gawler craton in South Australia (Fig. 1). Previous melt and fluid inclusion studies have suggested that interaction of a fluorine-enriched (McPhie et al., 2011a; Agangi et al., 2012) magmatic fluid with a non-magmatic brine was involved for IOCG–(U-REE) mineralization in the Olympic IOCG province (Oreskes and Einaudi, 1992; Bastrakov et al., 2007; Davidson et al., 2007). Oreskes and Einaudi (1992) inferred, based on oxygen isotope data, that the hematite + sericite assemblages at Olympic Dam formed between 200° and 400°C and recorded an input of surficial water. Bastrakov et al. (2007) compared fluid inclusions from hematite-bearing (Emmie Bluff, Torrens Dam) and magnetite-rich prospects (Murdie-Murdie, Titan; Fig. 1). They concluded that fluids responsible for magnetite alteration are of magmatic-hydrothermal or leached igneous rock origin, and that reactions among fluids and igneous as well as metasedimentary rocks modified the fluid composition. By contrast, fluids involved in hematite-rich Cu–Au mineralization were interpreted as oxidized and presumably surface-derived meteoric-hydrothermal waters that subsequently equilibrated with igneous rocks (Bastrakov et al., 2007). Similarly at Oak Dam East, very saline (about 24–48 wt.% eqv. NaCl) brines were associated with early magnetite formation, whereas weakly to very saline (1.4–25 wt.% eqv. NaCl) fluids were related to later hematite alteration and chalcopyrite precipitation, induced by fluid mixing at more oxidized conditions (Davidson et al., 2007).
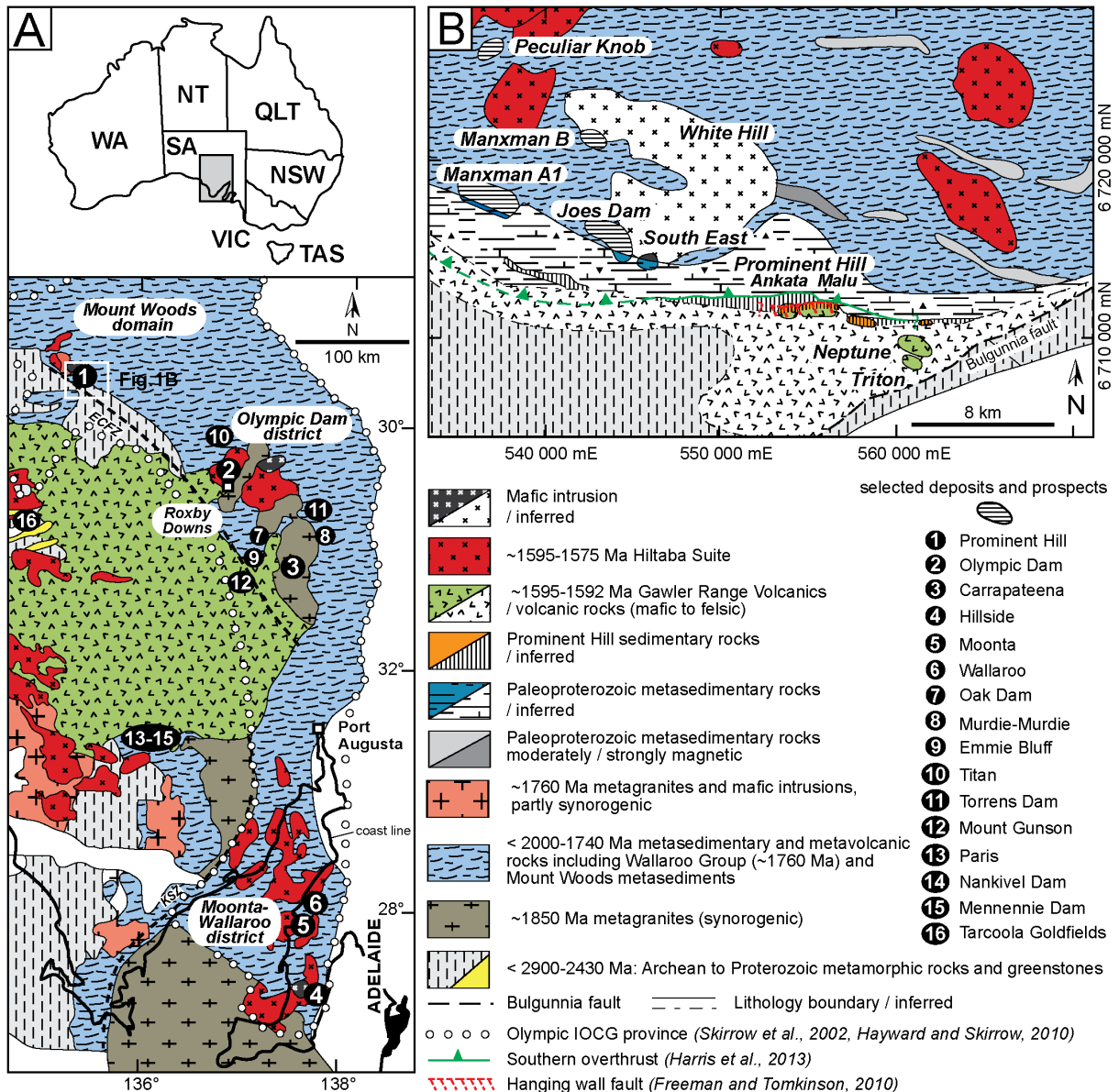
Fig. 1. (**A**) Interpreted geology of the eastern Gawler craton (South Australia) showing the extent of the Olympic IOCG province (modified from Skirrow et al., 2002; Hayward and Skirrow, 2010). (**B**) Interpreted geology of the southern Mount Woods domain (modified from Betts et al., 2003; Freeman and Tomkinson, 2010; Harris et al., 2013; Schlegel and Heinrich, 2015).

Fluid inclusion studies of IOCG deposits worldwide face the difficulties of relating any transparent gangue minerals to the ore-forming process and later metamorphic overprint. Luckily, the Cu (-Au) mineralized hematite breccias at the Prominent Hill deposit contain abundant fluorite and barite as an integral part of high-grade Cu-ore. Moreover, they are unmetamorphosed (Freeman and Tomkinson, 2010; Schlegel and Heinrich, 2015) in contrast to the syn- or even pre-metamorphic formation of IOCG deposits in northern Australia and Brazil, for example. These two facts were decisive in our selection of Prominent Hill for the first quantitative micro-analytical fluid inclusion study of an IOCG deposit, aimed at defining the composition of ore-forming fluids, interpreting the sources of fluids, and identifying the critical factors for mineral deposition. This paper integrates new fluid inclusion results with previous documentation of detailed geology, mineral paragenesis and alteration geochemistry (Schlegel and Heinrich, 2015) and a microanalytical study of texturally-constrained sulfur isotope variations (Schlegel et al., 2017). Rigorous petrography of fluid inclusion assemblage(s) (FIA), microthermometry and quantitative fluid inclusion analysis by laser-ablation inductively-coupled plasma-mass spectrometry (LA-ICP-MS), and improved quantification methods for Ca–

4

Na brines (Schlegel et al., 2012) constrain the process of economic ore formation at Prominent Hill. By integration of these data, we show how essential characteristics of hematite-rich IOCG breccia deposits can be explained by a distinct process that combines genetic elements of porphyry-type Cu and sediment-hosted Cu deposits.

2. Geological setting of the Prominent Hill deposit

2.1. General structure, major units and their relations to regional geology

The Prominent Hill deposit is located in the Paleoproterozoic basement of the southern Mount Woods domain (Flint and Benbow, 1977; Ambrose and Flint, 1981; Betts et al., 2003; Freeman and Tomkinson, 2010; Forbes et al., 2011; 2012; Allen at al., 2016) and is the second-largest mine in the Olympic IOCG province of South Australia (Fig. 1A). It is located south of a regional domain boundary fault, the Southern Overthrust (Betts et al., 2003; Harris et al., 2013), separating metamorphosed rock domains in the north from units of barely- to unmetamorphosed host rocks in the south (Fig. 2; Belperio et al., 2007; Freman and Tomkinson, 2010; Harris et al., 2013; Williams et al., 2017a, b). The Southern Overthrust converges with the so-called hanging wall fault (reverse to late sinistral strike-slip movement) in the Malu pit area, where they isolate calc silicate metasedimentary rocks in the hanging wall from siliciclastic, sedimentary rocks, tectonic breccias and mafic to intermediate lavas in the footwall (Fig. 2). The hanging wall rocks were correlated to the ca. 1750 Ma Wallaroo Group (Freeman and Tomkinson, 2010) and are altered to a magnetite skarn-like mineral assemblage, which is intruded by a dacite porphyry with a crystallization age of 1586 ± 12 Ma (LA-ICP-MS U-Pb dating of zircon; Bowden et al., 2017). The age is consistent with a period of extensive magmatic activity in the Gawler craton forming the Gawler Range Volcanics between 1604 ± 11 Ma and 1583 ± 16 Ma (Fanning et al., 1988, 2007; Creaser 1995, 1996) and plutons of the comagmatic (Giles, 1988; Creaser and White, 1991) and bimodal (Flint et al., 1993) Hiltaba Suite between 1594 ± 11 Ma and 1574 ± 5 Ma (e.g. Fanning et al., 1988; 2007; and references therein).

The sedimentary host rocks have a maximum depositional age of ca. 1750 Ma (LA-ICP-MS U-Pb data of detrital zircon) and were correlated to the Wallaroo Group as well (Freeman and Tomkinson, 2010; Bull et al., 2015; Williams et al., 2017a). Tectonic brecciation was initiated by boudinage of thinly interbedded carbonate and argillite beds (Schlegel and Heinrich, 2015; Allen et al., 2016). Basalts in the footwall show distinct similarities in most of their trace element compositions with gabbros from the Joes Dam SE prospect (Williams et al., 2017b). The gabbros are located in peripheral parts of the large White Hill mafic intrusion (Fig. 1B) and have a U-Pb zircon crystallization age of 1562 ± 14 Ma (Allen at al., 2016; Williams et al., 2017b, Fig. 2). The age is consistent within its uncertainty with a) the final stages of the Gawler Range Volcanics (ca. 1604 Ma to 1583 Ma), b) Hiltaba Suite magmatism in the Mount Woods inlier (Balta Granite, 1584 ± 14 Ma, U-Pb data of zircon; Fanning, 1997), c) regional N–S compression (cf. Page et al., 2005; Betts et al., 2006; Giles et al., 2006; Armit et al., 2014), and d) exhumation of the metasedimentary rocks north of Prominent Hill along the Southern Overthrust (Harris et al., 2013) starting between ca. 1592 and ca. 1582 Ma (Forbes et al., 2011; 2012). In addition, the dated gabbros show miarolitic cavities, pyrite-bearing exsolutions dominated by quartz, phlogopite and magnetite, and pegmatitic segregations as indicators of fluid saturation during crystallization (Schlegel et al. 2017, Fig. 2).
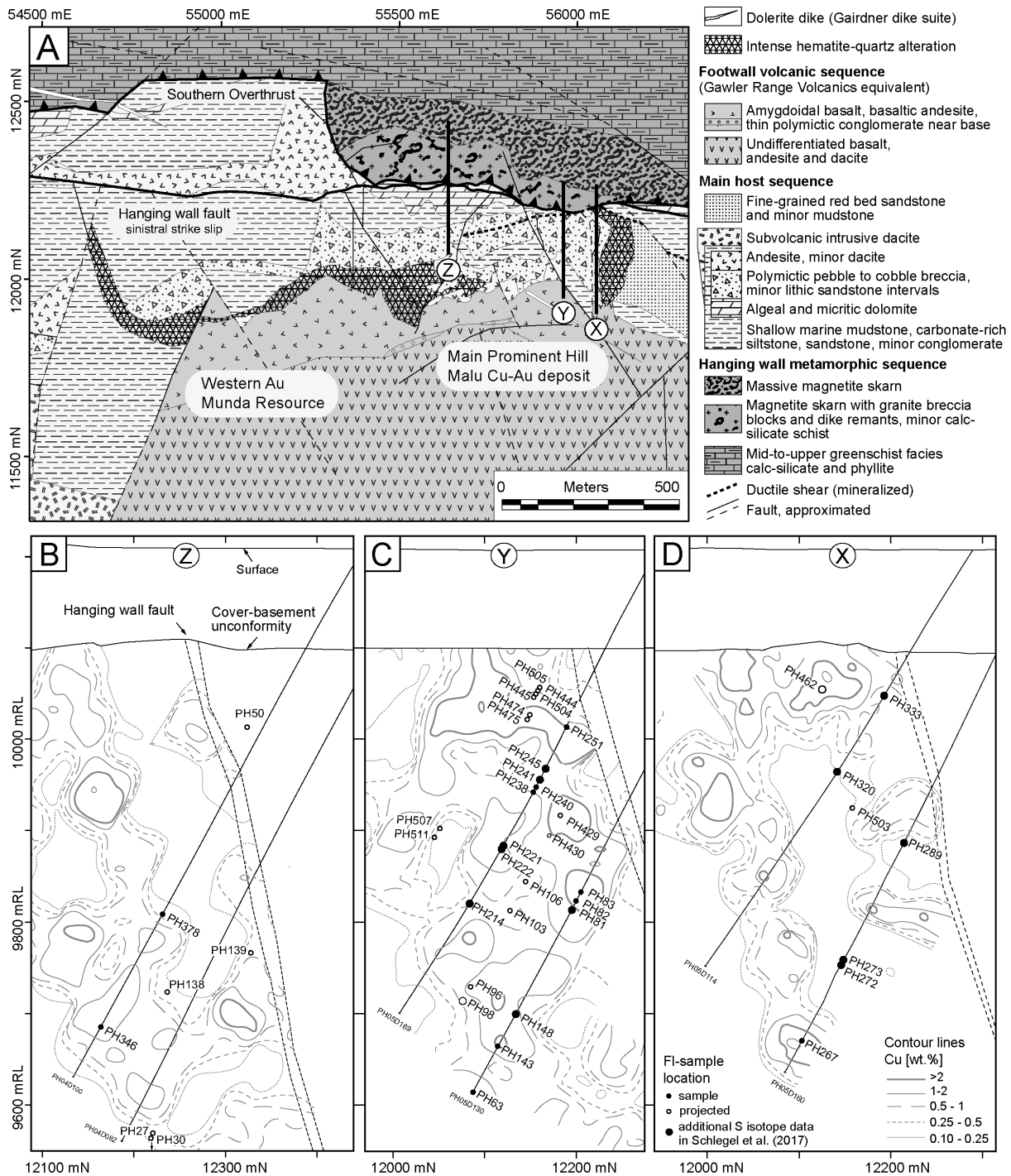
Fig. 2. (**A**) Simplified geological map of the Prominent Hill area below the cover sequence (modified from Williams et al., 2017a) showing the locations of cross-section X: 56050 mE, Y: 55950 mE, and Z: 55650 mE (in mine grid, UTM, zone 53 with easting reduced by 500000). (**B-D**) Cross-sections X, Y and Z with Cu-grade distribution in the footwall, traces of drill holes and locations of the samples used in this study. Large symbols indicate samples for which sulfur isotope data is available from Schlegel et al. (2017). Note Cu-poor but pervasively altered core zone in section 56050 mE (D), next to the Au-rich hematite-quartz breccia shown in (A).

2.2.   Geology of the Prominent Hill deposit

The Malu Cu–Au orebody is entirely hosted by hematite-altered sedimentary and volcanic rocks in the footwall (Belperio et al., 2007; Freeman and Tomkinson, 2010; Schlegel and Heinrich, 2015; Bull et al., 2015; Schlegel et al., 2017; Williams et al., 2017a, b). The sedimentary host rocks include mono- and polymictic, pebble and cobble breccias, coarse-grained clastic to

finely laminated argillaceous rock types with volcaniclastic components and variable, but frequently dominant, carbonate content (Fig. 2, Belperio et al., 2007; Freeman and Tomkinson, 2010; Schlegel and Heinrich, 2015; Allen et al., 2016; Williams et al., 2017a). The protoliths to this succession were sandstones, graywackes, shallow carbonate reefs, and turbidities grading into interlayered hemipelagic sedimentary rocks (Bull et al 2015). Today, the sedimentary rock package is overturned and separated from structurally underlying (stratigraphically overlying) lavas by subaerial, high-energy, clastic sediments including a volcanic clast conglomerate (red beds), which were deposited in an alluvial to fluvial plain. The plain was interpreted as an unconformity separating the Gawler Range Volcanics and red beds from an underlying sedimentary rock package (Bull et al., 2015). Bull et al. (2015) further interpret that sedimentation after the hiatus was disturbed by extrusive volcanism damming the plain, resulting in the formation of a lake. The red beds have a maximum age of ca. 1590 Ma (Allen et al., 2016; Williams et al., 2017b). The lavas are dominantly amygdaloidal to massive basaltic andesites and andesites, and equivalent to the Gawler Range Volcanics based on geochemical similarity and geochronological constraints described above (Belperio et al., 2007; Fremman and Tomkinson, 2010; Bull et al., 2015; Williams et al., 2017a, b).

Hematite-dominated alteration and economic Cu-(Fe) sulfide mineralization occurred during and after rotation of the brecciated host rock package as evident from geopetal markers in the high-grade breccia (Schlegel and Heinrich, 2015). Further support for this sequence of events comes from the fact that (premineralization) dikes intruded the overturned sedimentary rocks and breccias. These dikes are altered, sometimes mineralized but generally not brecciated (Schlegel and Heinrich, 2015). The latest dikes crosscut all lithologies and postdate the iron oxide alteration and mineralization. They may represent equivalents of the Neoproterozoic Gairdner Dike swarm (Freeman and Tomkinson, 2010).

Sulfides were introduced in two stages (Schlegel et al., 2017). Pyrite and minor chalcopyrite in the magnetite altered metasedimentary rocks characterize sulfide stage I. Texturally early pyrite and chalcopyrite also occur in the hematite breccias and the sedimentary host rocks. These early sulfides may have formed as part of a regional magnetite-rich alteration, as pyrite-rich halos extending beyond the limits of magnetite alteration (Schlegel et al., 2017). Another part of early pyrite shows a Re-Os age of 1734 ± 9 Ma and may be of detrital origin (Allen et al., 2016). Importantly, all early sulfides in rocks of the footwall show sulfur isotope compositions that are indistinguishable from sulfides in rocks of the magnetite altered hanging wall.

The economic mineralization was formed during sulfide stage II and is characterized by a highly oxidized but low-sulfidation mineralogy with highly variable sulfur isotope compositions consistent with derivation from SO_2 degassing of the Gawler Range Volcanics at the paleo-surface (Schlegel et al., 2017). In addition, there is no geologic or isotopic evidence for a significant sulfur contribution from seawater or a sedimentary sulfate-source in the recorded mineralization stages (Schlegel et al., 2017).

2.3.   Subeconomic stage I mineralization in the hanging wall

Mid-to-upper greenschist-facies metamorphosed calcareous, siliciclastic, calc silicate metasedimentary rocks are altered to a massive magnetite skarn-like mineral assemblage also containing phlogopite + chlorite + pyrite + chalocpyrite + actinolite-tremolite + serpentine + talc + scapolite (magnetite skarn; Belperio et al., 2007; Freeman and Tomkinson, 2010; Schlegel and Heinrich, 2015). The rocks hosts pyrite and minor chalcopyrite associated with the early, regionally widespread but subeconomic sulfide stage I mineralization (Schlegel et al., 2017), and are likely tectonically jusxtaposed to the orebody suggesting that the latest movement along the hanging wall fault is post-sulfide stage II. The magnetite skarn is crosscut by magnetite + quartz + calcite + fluorite ± chalcopyrite ± pyrite ± barite ± K-feldspar veins and calcite + quartz ± hematite ± fluorite ± chalcopyrite veins.

2.4.   Economic stage II mineralization in the footwall

Two distinct hematite breccia types developed by multiple pulses of pervasive and zoned replacement of host rocks (Schlegel and Heinrich, 2015). The hematite-quartz breccia and the hematite-aluminosilicate breccia are the result of gradients in the intensity of hydrothermal alteration between hematite + quartz alteration and hematite + chlorite + sericite (muscovite-phengite) ± siderite alteration. Both alteration styles developed in previously brecciated and unbrecciated host rocks. The economic Cu-(Fe) sulfide mineralization is associated with hematite + chlorite + sericite ± siderite alteration (Belperio et al., 2007; Freeman and Tomkinson, 2010; Schlegel and Heinrich, 2015). Economic gold is commonly associated with the transition between the hematite + quartz alteration and the hematite + chlorite + sericite ± siderite alteration (Belperio et al., 2007). Hydrothermal muscovite and phengite from the ore body has been dated by $^{40}Ar/^{39}Ar$ geochronology. Althouth Bowden et al. (2017) recorded a rather large scatter in the documented $^{40}Ar/^{39}Ar$ ages ranging between ca. 1600 Ma and 1550 Ma, their prefered minimum age for sericitization of dikes and volcanic rock is between 1585 and 1570 Ma, consistent with mineralization during the Gawler Range Volcanic and Hiltaba Suite magmatic event.

Other hydrothermal minerals of stage II mineralization include hematite, magnetite (truly minor), siderite, ankerite, quartz, chlorite, (fluor)-apatite, fluorite, barite, REE-U minerals including monazite, uraninite and coffinite, and Cu-sulfides including chalcopyrite, chalcocite, bornite, digenite, idaite and minor covellite defining assemblages of low to very low sulfidation state (Belperio et al., 2007; Schlegel and Heinrich, 2015; Schlegel et al., 2017). Replacement of carbonates and aluminosilicates such as feldspars, muscovite and chlorite by hematite + quartz + fluorite + (fluor)-apatite + barite is characteristic for intense hematite-quartz alteration at Prominent Hill. The richest Cu mineralization is dominated by chalcocite and is associated with moderate hematite alteration (Schlegel and Heinrich, 2015).

The Cu-(Fe) sulfide mineralization is commonly strata-bound following the geochemically mappable lithostratigraphy, but within favorable strata, copper is concentrated along a discordant alteration front of intermediate alteration intensity with stable hematite + chlorite + sericite + siderite + fluorite + barite (Schlegel and Heinrich, 2015). Locally, intense hematite + fluorite + barite + chalcopyrite alteration replaces the carbonate-rich breccia matrix. Hematite, aluminosilicates, barite, fluorite, carbonate and minor quartz are intimately intergrown with Cu-(Fe) sulfides within the breccia matrix. High-grade mineralization with chalcocite + digenite + bornite + idaite + chalcopyrite ± covellite replaces stage I pyrite (Schlegel et al., 2017), fills vugs and cavities in the porous breccia matrix (Schlegel and Heinrich, 2015, Fig. 9D) or replaces altered breccia clasts. Quartz related to the copper ore-stage is not abundant in the hematite-aluminosilicate breccia matrix, whereas hematite is ubiquitous in all vein types crosscutting the footwall. Veins are commonly widely spaced and crosscutting relationships among them are rarely observed. Vein types cutting the mineralized hematite breccia matrix include siderite + quartz + fluorite + barite + chalcopyrite ± bornite ± calcite veins, barite + bornite + chalcocite ± hematite veins, and late specular hematite + Cu-(Fe) sulfide ± quartz veins as well as late calcite + barite + pyrite + fluorite ± chalcopyrite ± bornite ± chalcocite veins. In contrast, siderite-bearing veins are among the paragenetically earliest and also appear as clast-/vein-like structures, with siderite gradually coalescing into the porous and mineralized hematite-aluminosilicate breccia.

3. Samples and methods

The Prominent Hill deposit preserves abundant, petrographically consistent fluid inclusion assemblages (FIA) in the breccia matrix and in vein samples. Many FIA can clearly be related to breccia mineralization during the main sulfide stage II, some FIA may predate stage II as potentially late-stage I fluids, and some occur in veins that cut the breccia and may represent the

waning stage of economic mineralization. Representative samples (Figs. 2 and 3) contain fluid inclusions hosted in quartz, fluorite and barite that are typically intergrown with Cu-(Fe) sulfides and hematite.

Samples may be divided into six types (Table 1): (1) hematite-aluminosilicate breccia matrix with fluid inclusions in fluorite and/or barite intergrown with Cu-(Fe) sulfides (Fig. 3A-D); (2) hematite-aluminosilicate breccia clast-replacement by fluorite, sericite and/or calcite (Fig. 3E); (3) siderite + quartz + fluorite + barite + chalcopyrite ± bornite ± calcite veins (Schlegel and Heinrich, 2015, Fig. 9G); (4) calcite + barite + pyrite + fluorite ± chalcopyrite ± bornite ± chalcocite veins (Fig. 3F); (5) specular hematite + quartz veins crosscutting the hematite breccia body; and (6) transparent quartz in Cu-(Fe) sulfide-poor magnetite + quartz veins (Fig. 3G) crosscutting the magnetite altered metasedimentary rocks of the hanging wall. Hematite hosts intermediate- to low-density FIA as shown by reconnaissance infrared microcopy, but the interlocked crystals effectively reduce the transmittance of infrared light and thus make detailed fluid inclusion petrography impossible (Schlegel, 2010). Quartz-rich fragments of unknown origin enclosed in the breccia and their secondary FIA were excluded from quantitative study.

Detailed fluid inclusion petrography was carried out on 48 samples with quartz, fluorite, barite, calcite or dolomite (Table 1). Fluid inclusions assemblages were investigated by petrography using the established criteria for primary, pseudosecondary and secondary assemblages (Roedder, 1984; Goldstein and Reynolds, 1994). Fluid inclusions are classified according to phase proportions and the number and presence of daughter crystals at room temperature. The terminology (e.g. LV_5HoS) uses capital letters for liquid (L), vapor (V), halite (H), another isometric solid (S) and a needle-shaped daughter crystal (N). Subscripts indicate volume percent of vapor in the inclusion, and small letters in front of S and N further describe the nature and color of solid(s) present, i.e., black (b), opaque (o) and red (r).

Microthermometry was performed on 1018 fluid inclusions belonging to 135 FIA from 16 samples. We used temperature cycling (Haynes, 1985) to measure two last-melting temperatures, of ice and of hydrohalite ($NaCl·2H_2O$), or ice melting and halite dissolution in each fluid inclusion. NaCl and $CaCl_2$ salinities were quantified from these temperatures using the H_2O–$NaCl$–$CaCl_2$ phase relations as reviewed by Steele-MacInnis et al. (2011). NaCl and $CaCl_2$ concentrations defined the quantity of the total Cl-salinity (Cl_{tot}) as a measure of the conservative salinity component. To determine the Na concentration as an internal standard for quantification of LA-ICP-MS analysis, we used the microthermometric approach of Schlegel et al. (2012) based on the ternary $Na-Ca-H_2O$ model system. We did not use the more recent evaluation of low-temperature phase relations in multi-component fluids by Steele-MacInnis et al. (2016), because it introduces variations in calculated Na concentrations that are not real, but primarily reflect random uncertainties in elemental analysis by LA-ICP-MS.

In-situ LA-SF-ICP-MS data were successfully acquired for a total number of 85 assemblages from 14 samples, combining a total of 556 individual inclusion analyses. The Appendix and Table A1 contain further details on the methodology of microthermometry, LA-SF-ICP-MS conditions using a highly sensitive sector-field mass spectrometer and methods of microanalytical quantification.
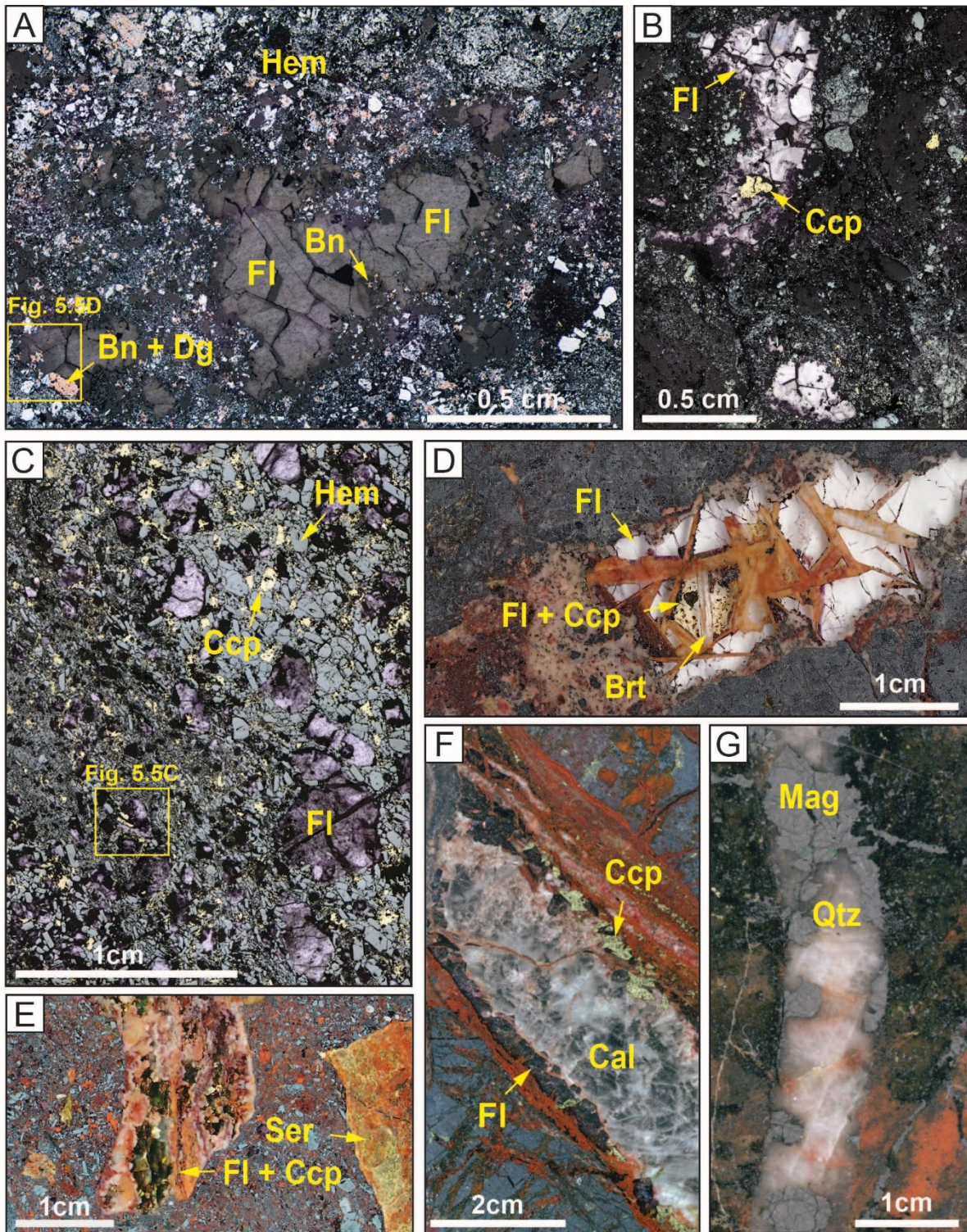
Fig. 3. Photomicrographs of representative samples from the hematite-aluminosilicate breccia matrix (A-E) and from veins crosscutting the hematite breccia and the magnetite altered metasedimentary rocks (F, G). (**A**) Coarse-grained fluorite (Fl) intergrown with bornite (Bn), digenite (Dg) and hematite (Hem); PH475, PH06D119, 214.4 m. (**B**) Coarse-grained fluorite intergrown with chalcopyrite (Ccp) and fine-gained hematite; PH238, PH05D169, 296.1 m. (**C**) Intergrown fluorite, chalcopyrite and hematite in hematite + calcite bearing matrix, modified from Schlegel et al. (2017); PH462, PH09D229, 179.9 m. (**D**) Breccia cavity containing carbonate-cemented Cu-sulfide poor wall rock debris (bottom left). The remaining cavity space is filled with barite (Brt), fluorite and chalcopyrite; PH251, PH05D169, 219.4 m. (**E**) Sericite (Ser) altered sedimentary rock clast is partly replaced by chalcopyrite and fluorite; PH505, PH04D057, 186.1 m, modified from Schlegel and Heinrich (2015). (**F**) Calcite (Cal) + fluorite + chalcopyrite vein crosscutting chalcopyrite-bearing breccia matrix, modified from Schlegel and Heinrich (2015); PH82, PH05D130, 438.3 m. (**G**) Quartz (Qtz) + magnetite (Mag) vein crosscutting magnetite altered metasedimentary rock in the hanging wall; PH50, DP017, 220.0 m.

10

Table 1. Location and description of fluid inclusion samples from the Prominent Hill, IOCG deposit

Sample	Hole	m	Description (sample-type as in text)	Host	P	M	LA	SI	Comments
Hematite-aluminosilicate breccia matrix									
PH63	PH05D130	670.0	Quartz + hematite-filled amygdale of altered mafic to intermediate volcanic rock	Qtz	x				(Schlegel, 2010, Fig. 4e)
PH81	PH05D130	445.5	Fluorite and interstitial barite within high-grade chalcopyrite-bearing breccia-aluminosilicate breccia matrix	Brt	x	x	x	x	Fig. 5A and Schlegel (2010), Fig. 4d
PH96	PH04D059	575.6	Hematite-aluminosilicate breccia matrix containing fluorite	Fl	x				
PH135	Pit stage 1	unkn	Siderite + quartz +fluorite vein exsolution filling porous, bornite-bearing hematite-aluminosilicate breccia matrix	Qtz	x		x		
PH138	PH05D147	570.2	Fine-grained fluorite and chalcopyrite in laminated hematite-aluminosilicate breccia matrix	Fl	x				
PH143	PH05D130	615.4	Geopetal marker in hematite + quartz-altered sandstone filled with calcite, bornite and barite	Brt, Cal	x				(Schlegel and Heinrich 2015, Fig. 11C)
PH148	PH05D130	575.1	Barite, fluorite, and chalcopyrite infill hematite-aluminosilicate breccia matrix	Brt, Cal	x		x		
PH214	PH05D169	438.4	Siderite + calcite + fluorite + chalcopyrite bearing hematite-quartz breccia cavity	Fl	x		x		
PH221	PH05D169	366.6	Sericite + fluorite + quartz + chalcopyrite-replaced breccia clasts in high-grade chalcopyrite-bearing hematite-aluminosilicate breccia	Fl	x		x		
PH222	PH05D169	367.8	Patchy intergrown hematite, fluorite and chalcopyrite replacing calcareous breccia matrix	Fl	x		x		
PH238	PH05D169	296.1	Coarse-grained fluorite intergrown with chalcopyrite in hematite-rich, mineralized breccia matrix	Fl	x	x	x		Fig. 3B
PH240	PH05D169	295.0	Fine-grained fluorite, barite and chalcopyrite in hematite-rich mineralized breccia matrix	Fl	x				
PH245	PH05D169	269.1	Coarse-grained fluorite and associated bornite replace early pyrite grains in hematite-rich breccia matrix	Fl	x	x	x	x	
PH251	PH05D169	219.4	Breccia cavity filled carbonate-cemented hematite altered wall rock debris. Cavity later filled with barite, fluorite and chalcopyrite	Brt, Fl	x	x	x		Fig. 3D
PH272	PH05D160	509.0	Coarse grained chalcocite and barite intergrown with hydrothermal sericite filling a cavity in the hematite-quartz breccia	Brt	x		x		
PH273	PH05D160	502.5	Coarse-grained barite needles in hematite-aluminosilicate breccia cavity	Brt	x		x		
PH320	PH05D114	283.9	Barite-filled cavity in hematite-quartz breccia	Brt	x		x		
PH346	PH04D100	595.1	Chalcopyrite and white fluorite intergrown in chalcopyrite-bearing, sericite altered hematite-aluminosilicate breccia	Fl	x				
PH430	PH04D059	361.2	Small fluorite crystals in fine-grained chalcopyrite-bearing hematite-aluminosilicate breccia	Fl	x				
PH462	PH09D259	179.9	Hematite-aluminosilicate breccia showing intensive intergrown patchy hematite, fluorite and chalcopyrite-earing matrix that is crosscut by siderite + fluorite + chalcopyrite vein	Fl	x	x	x	x	Fig. 3C, Fig. 5C
PH429	PH04D059	321.7	Barite, bornite and chalcopyrite-rich hematite-aluminosilicate breccia matrix	Brt	x				
PH475	PH06D119	214.4	Coarser-grained fluorite intergrown with bornite in hematite-rich breccia matrix. Bornite replaces early pyrite in the matrix	Fl	x	x	x		Fig. 3A
PH484	PH05D057	340.5	Intense hematite + quartz-altered rock showing cm-scaled bornite and chalcocite intergrown with barite	Brt	x				
PH503	PH04D056	343.7	Barite and chalcocite infill porous hematite-aluminosilicate breccia matrix	Brt	x	x			
Hematite-aluminosilicate (and hematite + quartz) clast replacement									
PH267	PH05D160	599.5	Barite-rich replacement of breccia clast	Brt	x				
PH378	PH04D100	489.2	Barite and chalcocite replacing hematite-aluminosilicate breccia clast	Brt	x				
PH444	PH05D057	186.3	Fluorite + chalcopyrite calcite replaced hematite-aluminosilicate breccia clast	Brt, Cal	x				
PH504	PH04D057	187.2	Fluorite, calcite, chalcopyrite and chalcocite-bearing, partly replaced sedimentary rock clast within hematite-aluminosilicate breccia	Fl	x				
PH505	PH04D057	186.1	Chalcopyrite and fluorite partly replace sericite altered sedimentary rock clast	Fl	x	x	x		(Schlegel and Heinrich, 2015, Fig. 10B)
PH507	PH06D224	359.5	Intergrown barite and chalcocite replace hematite-quartz breccia clast	Brt	x				
PH511	PH06D224	366.1	Intergrown barite and chalcocite replace hematite-quartz breccia clast	Brt	x				(Schlegel and Heinrich, 2015, Fig. 10D)

Table 1. *(Continued)*

Sample	Hole	m	Description	Host	P	M	LA	SI	Comments
Siderite + quartz + fluorite + barite + chalcopyrite veins									
PH15	Pit stage 1	unkn	Dm-scaled chalcopyrite + pyrite-bearing siderite + quartz + fluorite + calcite vein cutting hematite-aluminosilicate breccia	Qtz	x	x	x	x	(Schlegel, 2010, Fig. 4B)
PH17	Pit stage 1	unkn	Dm-scaled chalcopyrite-bearing siderite + fluorite + quartz vein	Fl	x	x	x	x	
PH103	PH04D059	452.9	Siderite + fluorite vein containing chalcopyrite with a rim of bornite	Fl	x				
PH106	PH04D059	412.0	Chalcopyrite-bearing siderite + calcite + fluorite vein cutting pervasively altered hematite-quartz breccia	Fl	x				
Calcite + barite + pyrite + fluorite veins									
PH27	PH07D313	757.0	Fluorite + barite vein cutting the hematite-quartz breccia, near the contact to footwall volcanic rocks	Fl	x	x	x	x	(Schlegel, 2010, Figs. 4C, 6B)
PH82	PH05D130	438.3	Possibly late calcite + fluorite + chalcopyrite-bearing vein cutting through fine grained hematite + fluorite + barite + chalcopyrite-bearing breccia matrix. The vein shows several repetitions of early (1) intergrown fluorite, chalcopyrite precipitation and late (2) calcite filling	Fl	x	x	x		Fig. 3F
PH83	PH05D130	424.5	Coarse-grained hematite + bornite cavity infill crosscut by fluorite veins	Fl	x	x	x		
PH98	PH04D059	559.1	Chalcopyrite-bearing fluorite + barite vein crosscutting hematite-aluminosilicate breccia matrix	Fl	x	x	x	x	
PH289	PH05D160	358.0	Cm-scaled barite + hematite + fluorite + calcite vein	Brt, Fl	x			x	
PH474	PH06D119	212.0	Vein showing hematite, euhedral fluorite, blocky calcite and chalcopyrite, Fluorite shows skeletal growth structures	Fl	x				
Specular hematite + quartz vein									
PH06	Pit stage 1	10016	Specular hematite + quartz vein cutting the hematite-aluminosilicate breccia	Qtz, Hem	x	x			
Magnetite + quartz vein									
PH50	DP017	220.0	Magnetite + quartz vein cutting the magnetite altered calc silicate rock	Qtz	x	x	x		Fig. 3G
Other									
PH02	Pit stage 1	10016	Hematite + carbonate + barite vein crosscutting hematite-quartz breccia	Brt	x		x		
PH11	Pit stage 1	10016	Fluorite + hematite + barite vein cutting the hematite-aluminosilicate breccia	Fl	x				
PH30	PH07D313	740.0	Barite + fluorite vein cutting the hematite-aluminosilicate breccia	Fl	x				
PH139	PH07D313	515.5	Up to 2.5 cm hematite needles within dolomite	Hem	x				(Schlegel, 2010, Fig. 4G)
PH445	PH05D057	188.7	Granular fluorite, barite and chalcocite-bearing vein cutting the hematite-aluminosilicate breccia	Fl	x				

Abbreviations: Host minerals: Brt, barite; Cal, calcite; Fl, fluorite; Hem, hematite Qtz, quartz.

Methods: P, fluid inclusion petrography; M, microthermometry; LA, LA-ICP-MS; SI, sulfur isotope data available (see: Schlegel et al., 2017).

4. Results of fluid inclusion studies

Fluid inclusion work is focused on analysis of FIA that texturally bracket the main sulfide stage II of economic Cu mineralization. The results from fluid inclusion petrography (Figs. 4 to 6), microthermometry (Figs. 7 to 9; Tables A2 and A3) and LA-ICP-MS analysis (Figs. 10 to 14, A1 to A2; Table A4) are presented in all diagrams using one symbol for the average concentration of typically 3 to 15 individual fluid inclusions within an assemblage.

4.1. Types of fluid inclusions

Four fluid inclusion types can be petrographically distinguished, including several subtypes (Fig. 4). LV-type inclusions (Fig. 4A to 4F, highlighted by red frames) are abundant in all samples.

The inclusions are mostly spherical to lens-shaped and their sizes vary between <5 μm and >100 μm. The LV-type can be subdivided into subtypes with distinct vapor fractions of approximately 1, 5, 10, 15, and 40 vol.%. In barite, primary and secondary LV_1 inclusions (Fig. 4A) commonly do not show any vapor bubble at room temperature (Fig. 4B), but the tiny bubble appears during cooling to low temperatures, sometimes prior to freezing. However, freezing of barite-hosted liquid-only inclusions prior to petrography was avoided, because it commonly led to decrepitation or leakage and inconsistent phase proportions. Reported homogenization temperatures in barite are mostly based on the first heating run of the few inclusions showing vapor bubbles at room temperature. The primary LV_{10} subtype (30–150 μm) is abundant in barite and characterized by a distinct negative relief against the host (Fig. 4D). The LV-subtype FIA with 5, 15 and 40 vol.% vapor (Fig. 4C, 4E and 4F) typically form secondary trails in fluorite of late calcite + barite + pyrite ± fluorite ± chalcopyrite ± bornite ± chalcocite veins.

LVS-type inclusions (Fig. 4G-O, highlighted by blue frames) occur in all host minerals in the breccia matrix and in veins samples. The inclusion size typically varies between 5 and 60 μm, but some reach 250 μm. Subtypes contain a red solid (Fig. 4G), an opaque needle- or irregular-shaped solid (Fig. 4H, 4I) or both of these solid phases (Fig. 4J, 4K). The LVrS and LVoN subtypes (Fig. 4G, 4H) contain a red hexagonal solid or an opaque blade- or needle-shaped solid, with consistent phase proportions indicating that a hematite daughter crystal precipitated internally from a homogenous fluid. The LVoS-subtype (Fig. 4I) contains a small irregular- or round-shaped opaque solid. The shape and relative size of the opaque solids in this subtype vary, thus we interpret them as heterogeneously trapped mineral grains. Barite in the hematite breccia matrix contains the round to spherical LV_1rSoN inclusions (Fig. 4J). At room temperature, these FIA do not show a vapor bubble. The LVrS, LVoS, and LV_1rSoN subtypes are observed in primary clusters and pseudosecondary trails restricted to the interior of barite grains, but they are not abundant. The LV_2S, $LV_{10}S$, $LV_{20}S$ and $LV_{30}S$ subtypes (Fig. 4L to 4O) occur occasionally as primary (LV_2S) or pseudosecondary ($LV_{10}S$), but mostly as secondary FIA patches and trails, showing consistent phase proportions within the FIA. Thus, the solids are interpreted as true daughter crystals. Transparent daughter crystals are round to elongate in shape and are interpreted as sylvite (Schlegel, 2010).

The LVH(SS)-type inclusions (Fig. 4P to 4R, highlighted by green frames) contain halite, and some FIA occasionally contain additional solids as daughter crystals. Three subtypes, LV_5H, LV_5HS, and LV_5HSS are identified and they show an irregular shape with sizes of 5–25 μm.

Some vapor-rich fluid inclusions (Fig. 4S, highlighted by gray frame) are hosted by quartz of specular hematite + quartz veins of sample PH6 and in quartz of one siderite + quartz + fluorite + chalcopyrite ± calcite vein of sample PH15. They are small (<5 μm), are present only in secondary assemblages and show mostly inconsistent phase relations within an individual assemblage. They cannot be related to the ore-forming event in the breccia matrix and were not studied further.

4.2. Petrographic relationships and timing among fluid inclusion assemblages

Variations in the V/(L+V) ratio between different assemblages are much larger than variations within each assemblage, demonstrating significant differences in the bulk density of paleo-fluids recorded even within a single mineral grain. The hematite breccia body does not show many ore formation-related time markers such as vein crosscutting relationships. Therefore, a combination of relative time markers and characteristics of associated FIA was used to establish a relative chronology of fluid events in individual samples (Figs. 5 and 6). This included progressive growth zones in crystals showing successions of primary and pseudosecondary FIA. Unfortunately, the time relation between magnetite + quartz veins in the hanging wall and ore samples from the footwall are unknown.
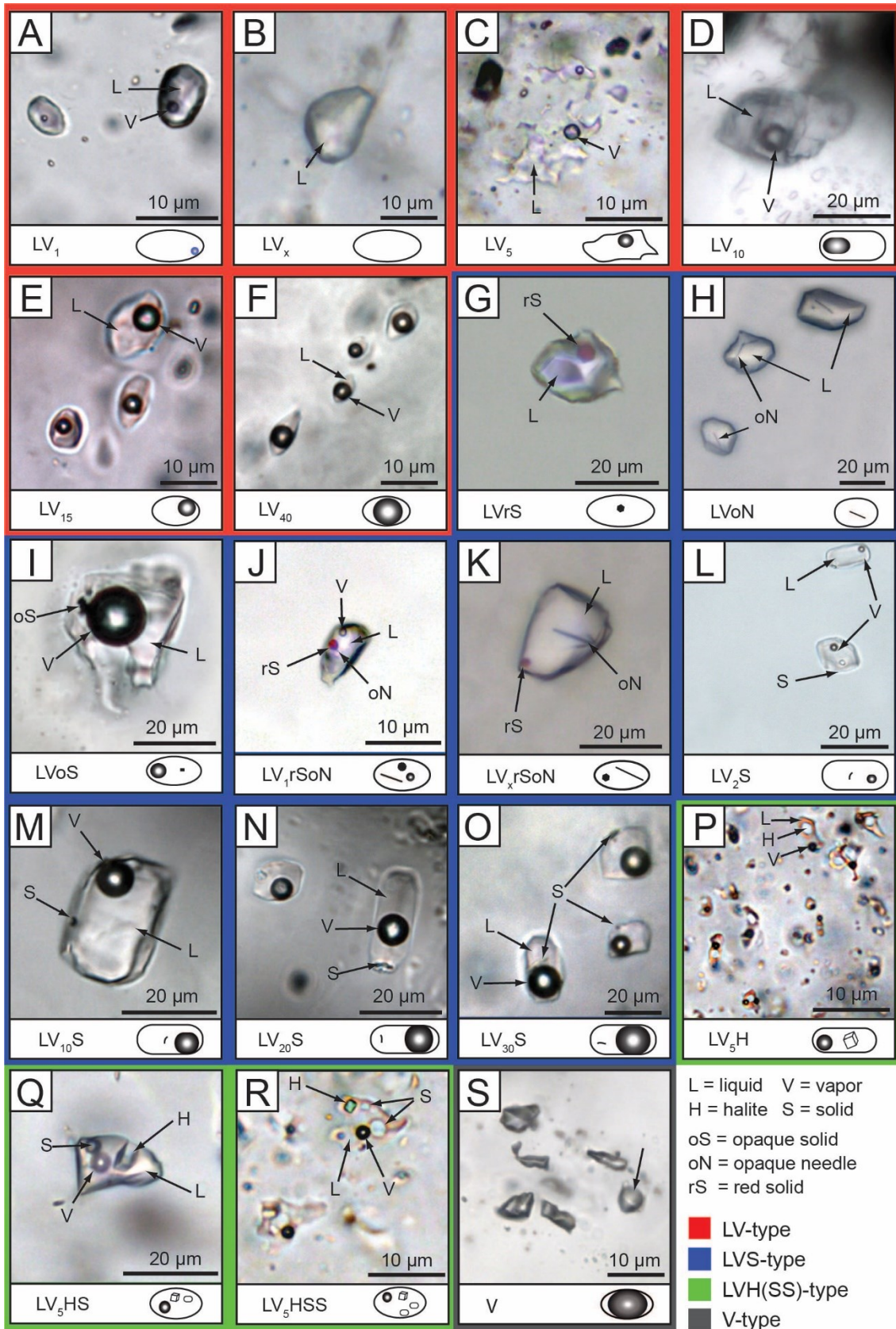
Fig. 4. Summary of the principal fluid inclusion types (grouped by frame color) and associated subtypes (A-S) present in transparent quartz, fluorite, and barite from the Prominent Hill iron oxide copper-gold deposit. Principal fluid inclusion are LV type (A-F, red frames), LVS type (G-O, blue frames), LVH(SS) type (P-R, green frames), and some V-type low-density inclusions (S, gray frames). Each inclusion subtype is described by a sequence of capital letters representing phases present in the inclusion. Phase abbreviations: H = halite, L = liquid, oN = opaque needle, oS = opaque solid, rS = red solid, S = solid daughter crystal, V = vapor (with subscript denoting the volume percent of vapor).

In general, fluorite and barite in matrix samples contain primary and pseudosecondary LV- and LVS-type FIA with 1, 2 and 10 vol.% vapor. In most matrix samples (e.g. PH81, PH462), primary LV-type FIA (i.e. the LV_1 and LV_{10} subtypes) were petrographically early (Fig. 5A to 5C). In other samples (e.g. PH238, PH475), primary LVS-type FIA (i.e. LV_2S subtype) are trapped early (Fig. 5D). Rare pseudosecondary and clearly secondary LV-type assemblages (i.e. LV_{15}, LV_{40} subtypes) postdate all other FIA in matrix and vein samples (Fig. 6). These relations indicate that LV and LVS fluid inclusions with low proportions of vapor overlapped in time, whereas some LV_{15} and LV_{40} fluid inclusions were trapped later during mineralization and locally postdate Cu-(Fe) sulfide formation. Abundant areas and clusters with primary and pseudosecondary FIA hosting LVH(SS)-type inclusions with 5 vol.% vapor occur in individual Cu-(Fe) sulfide- and hematite-rich matrix samples (e.g. PH475).

The hematite-aluminosilicate breccia contains primary LV- and LVS-type FIA with 2 and 10 vol.% vapor in barite and fluorite that are unambiguously associated with the Cu-(Fe) sulfide precipitation in the breccia matrix (Fig. 5A-D). In sample PH81 (Figs. 5A, 5B and 6A), two barite generations are separated by a dissolution front. Hematite, chalcopyrite and primary LV_{10} inclusions are intimately intergrown within barite of the earlier generation. The LV_{10} FIA are associated with chalcopyrite precipitation in this sample (Fig. 5A and 5B). The second barite generation contains primary LV_1 FIA. Both barite generations and the primary LV_{10} FIA are crosscut by secondary LV_1 FIA trails. In sample PH462 (Fig. 5C), hematite, chalcopyrite and fluorite containing primary LV_{10} inclusions are closely intergrown. In other samples (e.g. PH475), primary LV_2S FIA are related to bornite and chalcocite precipitation in vugs inside the hematite-aluminosilicate breccia matrix (Fig. 5D).

Petrographic relations of some vein samples are described in Schlegel et al. (2012), and we summarize essential information needed to establish the mineralogical and textural framework for the fluid inclusion petrography of matrix samples outlined above. Primary FIA of LV_5HS are abundant in siderite + quartz-bearing veins where they predate pseudosecondary LV_{40} FIA associated with chalcopyrite precipitation in one vein (Figs. 5E and 6B). Late calcite + barite + pyrite + fluorite ± chalcopyrite ± bornite ± chalcocite veins contain LVS-type FIA with 2, 10 and some with 20 and 30 vol.% vapor. These FIA occur as pseudosecondary trails, but later secondary trails are more common. Generally, LV_2S and $LV_{10}S$ FIA predate the $LV_{20}S$ and $LV_{30}S$ FIA in this vein type. LV- and LVS-type FIA with 15 vol.% and more vapor are abundant only in this sample type. A pseudosecondary $LV_{30}S$ FIA in fluorite appears co-genetic with chalcopyrite precipitation in the vein (PH82; Figs. 3F and 6C). In addition, sample PH82 shows secondary LV-type FIA with 15 and 40 vol.% vapor crosscutting single fluorite crystals, and possibly even later secondary trails with LV_5 FIA crosscutting several fluorite crystals (Fig. 6C). The LVS- and some LV-type inclusions in this sample occasionally contain irregularly shaped opaque crystals that were accidentally trapped. LA-ICP-MS analysis (see below) identified these crystals as Fe-, Cu-, S- and U-rich minerals, confirming that these FIA are probably synchronous with (or possibly postdate) chalcopyrite and U-mineral precipitation in the sample. The magnetite + quartz vein (Figs. 3G and 6D) contains two LVH(SS)-subtypes. An early FIA of primary LV_5HSS is succeeded by primary and pseudosecondary LV_5H FIA. In addition, pseudosecondary LV_1 FIA are followed by two generations of secondary LV_5 assemblages and intermediate density LV_{40} FIA which postdate the halite-bearing FIA.
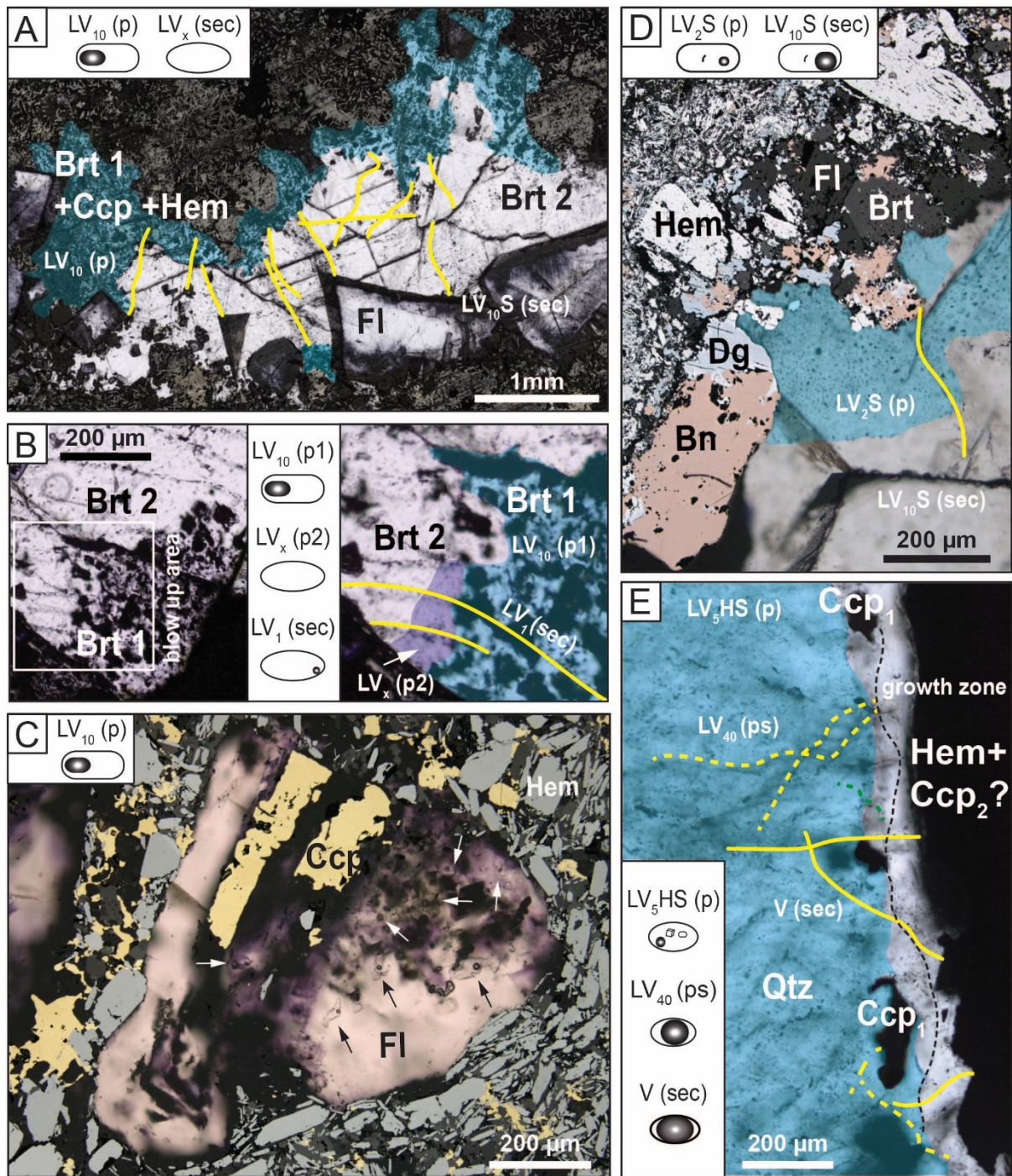
Fig. 5. Photomicrographs illustrating the distribution of fluid inclusion assemblages (FIA) in samples from the Cu-(Fe) sulfide-bearing hematite-aluminosilicate breccia matrix (A-D) and a siderite + calcite + quartz + chalcopyrite bearing vein (E). Blue shaded areas highlight zones that host primary (p) FIA. Yellow dashed and solid lines indicate healed microfractures with pseudosecondary (ps) and secondary (s) FIA, respectively. (**A**) Two barite generations in the breccia matrix, intergrown with fluorite (Fl) and fine-grained chalcopyrite in the hematite-aluminosilicate breccia matrix. (**B**) Barite generation 1 (Brt 1) hosts primary LV_{10} FIA intergrown with hematite and chalcopyrite (black spots). Barite generation 2 (Brt 2) contains primary LV_x inclusions that nucleate a small vapor bubble during low-temperature microthermometry. The latest FIA in this sample are secondary LV_1 fluid inclusion trails; PH81, PH05D130, 445.5 m. (**C**) Enlarged area of Figure 3C showing transparent fluorite intergrown with chalcopyrite (Ccp) and hematite (Hem). The fluorite contains primary LV_{10} fluid inclusions related to mineralization (arrow); PH462, PH09D259, 179.9 m. (**D**) The enlarged area of Fig. 3A shows coarse-grained fluorite intergrown with bornite (Bn) and digenite (Dg) in high Cu-grade breccia matrix. The fluorite contains primary LV_2S FIA; PH475, PH06D119, 214.4 m. (**E**) Part of a quartz crystal showing chalcopyrite present on growth zones. Primary LV_5HS fluid inclusions predate pseudosecondary (green) LV_{40} fluid inclusions and late secondary vapor inclusions. The LV_{40} and V-type fluid inclusions are associated with chalcopyrite (Ccp) mineralization; PH15, Malu Pit stage 10016 mRL.

16
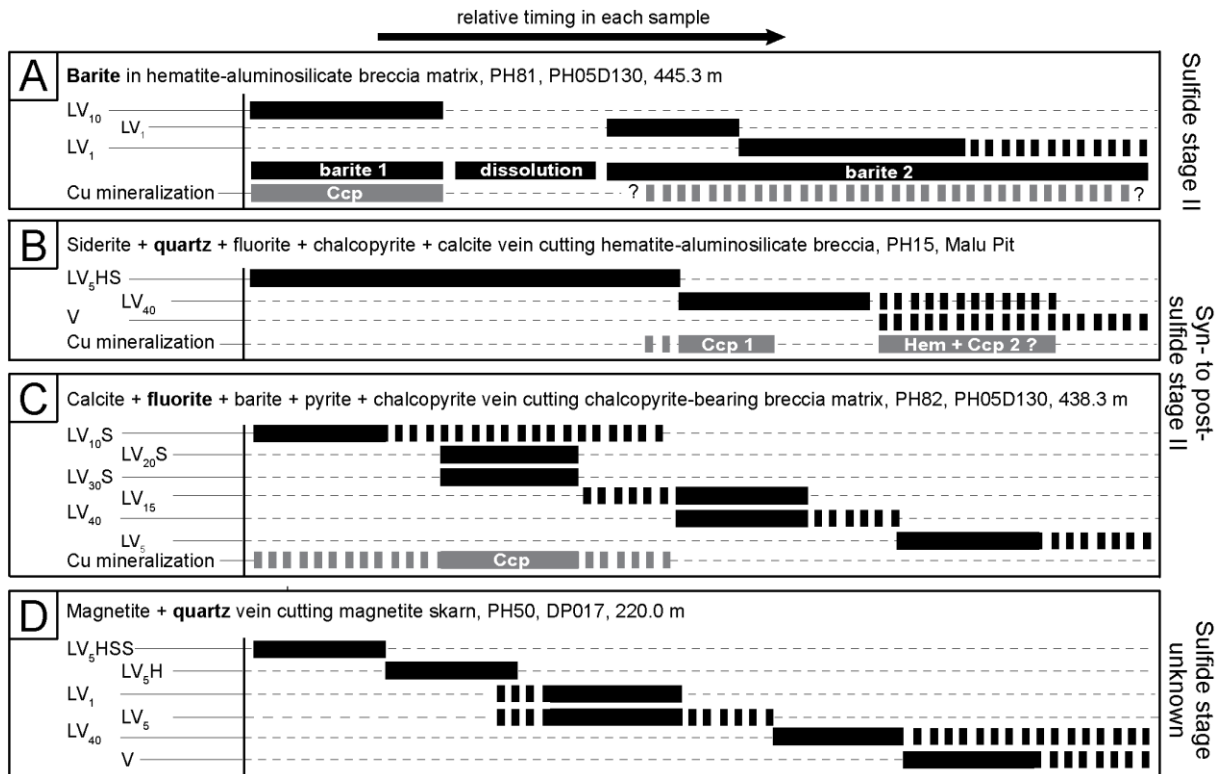
Fig. 6. Paragenesis diagram illustrating the relative time sequence of different FIA, based on four particularly diagnostic samples from the breccia matrix (**A**), from veins crosscutting the hematite breccia body (**B, C**) and from the magnetite skarn-like replacement body (**D**). Bold mineral names denote the fluid inclusion host mineral. Mineral and phase abbreviations: Ccp: chalcopyrite; L: liquid; V: Vapor with number as subscript denoting the vol.% of vapor; H: halite; S: solid daughter crystal.

4.3. Microthermometric results

In total, 841 of 1018 fluid inclusions showed reproducible melting behavior without metastability problems during low-temperature microthermometry. The majority of FIA show vapor-saturated initial melting temperatures around –50°C. Most FIA show a distinct freezing behavior and a consistent melting sequence of ice, hydrohalite and halite, indicating that their composition can be approximated by the ternary H_2O–$NaCl$–$CaCl_2$ system (Yanatieva, 1946; Vanko et al., 1988; Zwart and Touret, 1994; Steele-MacInnis et al., 2011).

We systematically measured two low-temperature phase transitions by microthermometry (cf. Appendix) and quantified variable $NaCl$ and $CaCl_2$ concentrations in fluid inclusions, with reference to experiments in the ternary fluid system (Fig. 7). In Figure 8A, compositions are reported as total ($NaCl$ + $CaCl_2$) salinity varying from 0.6 to 45.4 wt.% and the concentration ratio $NaCl$/($NaCl$ + $CaCl_2$) varying from about 0.3 to > 0.9. The $NaCl$ concentrations range between 0.6 and 35.2 wt.% and $CaCl_2$ concentrations reach 21.7 wt.%. Total homogenization temperatures vary between 107° and 475°C (Fig. 8B). Total homogenization occurred either by vapor disappearance T_h(LV→L) or by halite dissolution T_h(LH→L). All halite-bearing FIA show standard deviations between ± 7°C and ± 13°C for halite dissolution and vapor disappearance temperatures, and this small variation indicates that heterogeneous halite entrapment can effectively be excluded (cf. Lecumberri-Sanchez et al., 2015).

The LV- and LVS-type fluid inclusions in fluorite and barite within hematite-aluminosilicate breccia matrix samples homogenized by vapor disappearance into the liquid phase between 108°C and > 220°C. The upper value is a minimum temperature, because fluorite and barite host minerals may expand prior to homogenization at high temperatures, resulting in a sudden increase in bubble size due to mineral expansion (Fig. 8B).

17
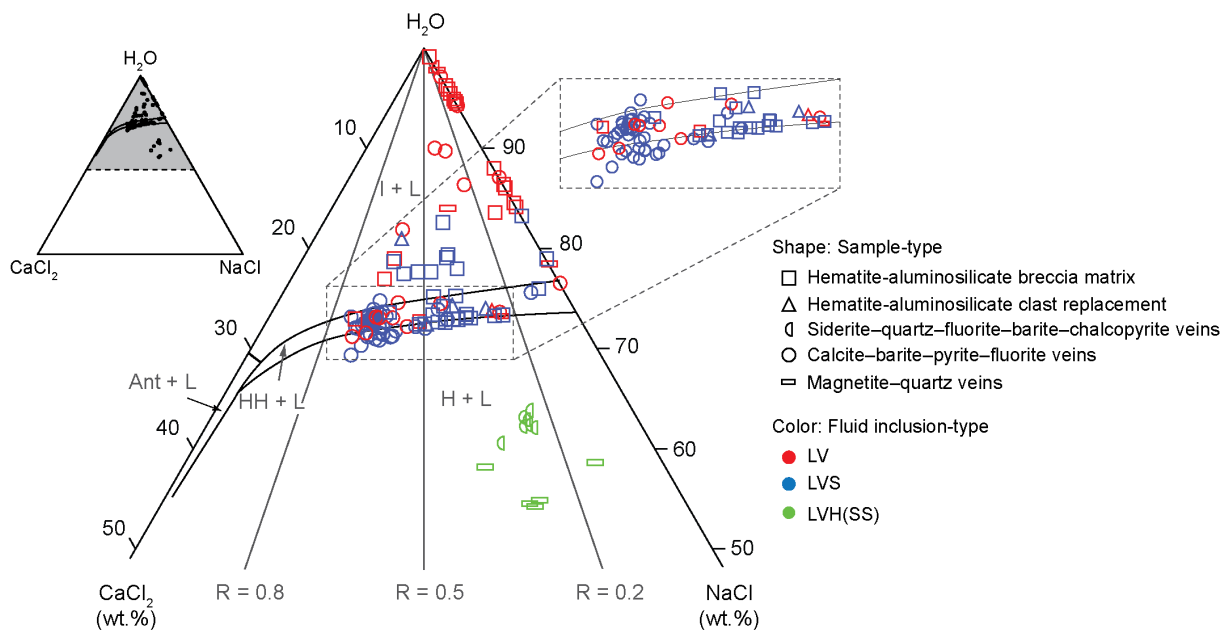
Fig. 7. Ternary H_2O–$NaCl$–$CaCl_2$ diagram (after Yanatieva, 1946; Vanko et al., 1988; Oakes et al. 1990) showing the stability fields of ice (I), hydrohalite (HH), halite (H) and antarcticite (Ant) coexisting with liquid (L). Plotted are average true salinities of fluid inclusion assemblages (FIA) determined by measuring two low-temperature phase transitions by microthermometry. The data is sorted by sample (symbol shape) and fluid inclusion type (symbol color; cf. Fig. 4). The NaCl and $CaCl_2$ salinity of each FIA was calculated from two phase melting temperatures using the equations from Steele-MacInnis et al. (2011). The salinities of FIA interpreted in terms of the NaCl–H_2O fluid system (in cases when only final ice melting was observed) were calculated using equations from Bodnar and Vityk (1994).
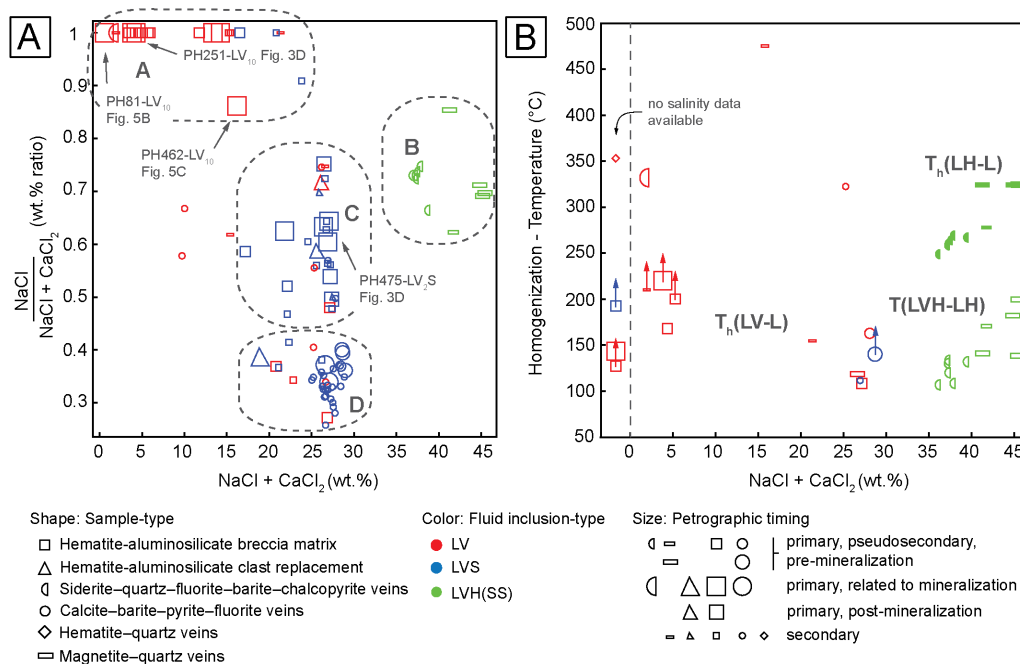
Fig. 8. Variation diagrams of (A) true NaCl-salinity and (B) temperature of homogenization as function of the total salinity (NaCl + $CaCl_2$) determined from two low-temperature microthermometric measurements. Letters A, B, C and D indicate the four FIA data groups present in samples from the Cu-mineralized hematite breccia body at Prominent Hill. Diagram (B) shows the temperature of final homogenization including data with $T_h(LH→L)$ representing total homogenization by halite dissolution, $T_h(LVH→LH)$ representing vapor disappearance in LVH(SS)-type assemblages and $T_h(LV→L)$ homogenization in LV- and LVS-type assemblages. Data marked with an arrow represent minimum temperatures, because these FI were not heated up to the temperature of homogenization, in order to prevent decrepitation or stretching. Data is sorted by sample type (symbol shape), fluid inclusion type (symbol color) and petrographic timing with respect to Cu-(Fe) sulfide formation in each sample type (indicated by symbol size; the largest symbols denote data most closely related to economic Cu mineralization). Individual FIA of particular significance are highlighted and discussed in the text.

18

Total homogenization of primary LVH(SS)-type inclusions in individual FIA hosted in siderite + quartz + fluorite + barite + chalcopyrite veins took place by halite dissolution between 249 ± 9°C and 269 ± 4°C, at notably higher temperatures than the vapor disappearance recorded between 107 ± 5°C and 133 ± 4°C. A pseudosecondary LV_{40} FIA associated with chalcopyrite mineralization in the vein homogenized at 332 ± 20°C (Fig. 5E). The $LV_{10}S$- and $LV_{20}S$-type FIA in calcite + barite + pyrite + fluorite veins homogenized between 111 ± 13°C and > 163°C, whereas petrographically later LV_{15} FIA homogenized at higher temperatures, one homogenized at 323 ± 19°C and the other decrepitated at 200°C. The LV_{40} FIA in the hematite + quartz vein homogenized at 354 ± 28°C. Halite in LVH(SS)-assemblages in the magnetite + quartz vein dissolved between 278 ± 13°C and 325 ± 6°C, while vapor disappearance occurred between 138 ± 9°C and 200 ± 5°C. A petrographically well defined succession of FIA ranging from early LV_1, through LV_5 to later LV_{30} FIA homogenized at 119 ± 6°C, 155 ± 11°C and 475 ± 14°C, respectively. Despite the limited number of recorded homogenization temperatures, the common petrographic observation of inclusions with small vapor bubble sizes (LV_{2-10}) predating those with larger vapor bubble sizes (LV_{15-40}) is robust and significant (Figs. 6 and 9). This observation indicates that conditions of rather low temperature and pressure during mineralization in the breccia matrix were commonly overprinted by influx of hotter fluids. Petrographic relations and systematic variations in inclusion density, NaCl and $CaCl_2$ concentration among distinct FIA in single samples leave no doubt that temperatures and fluid compositions varied significantly during IOCG mineralization at the Prominent Hill deposit (Figs. 8 and 9).
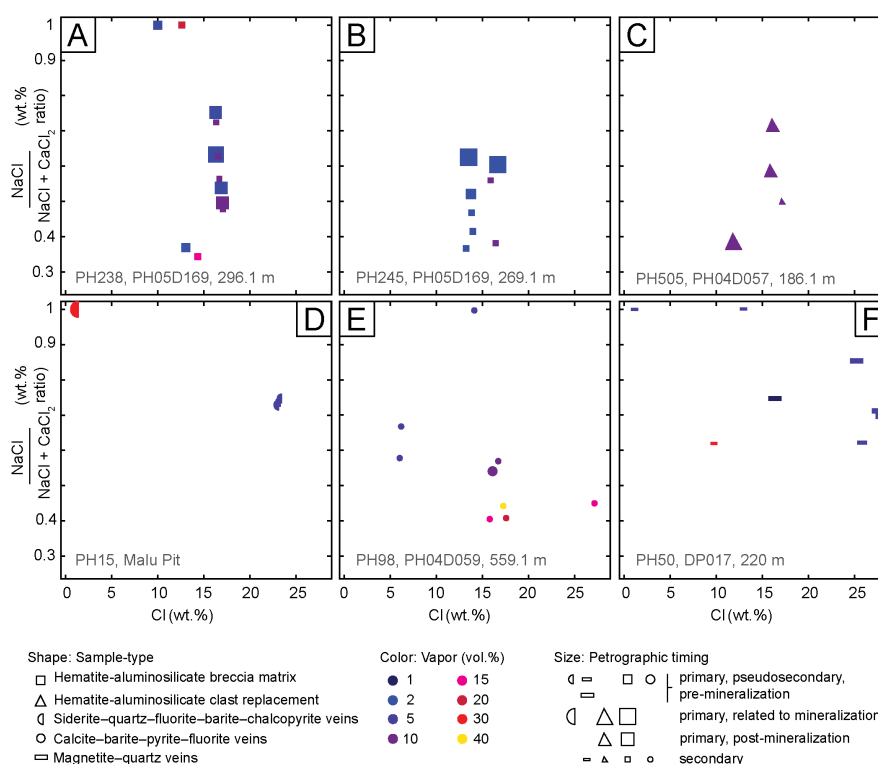
Fig. 9. Variation diagrams showing the total Cl salinity (wt %), derived from the (NaCl + $CaCl_2$) concentrations obtained from microthermometry, as a function of the NaCl mass fraction. Each diagram contains data for an individual sample, highlighting the petrographically established time sequence of different fluid inclusion assemblages in each sample. Each symbol represents one fluid inclusion assemblage, and the variation within one fluid inclusion assemblage is much smaller than the total variation. Successive fluid inclusion assemblages in individual breccia matrix samples (A-C) record lower salinity variations compared to fluid inclusion assemblages in vein samples (D-E). Samples plotted in (A), (B), and (D) record a general decrease in fluid density with time, which is equivalent to a path that reflects increasing temperature for near-constant pressure. The data shown in (E) and (F) record distinct fluctuations in salinity and fluid density.

Fig. 10. Variation diagrams illustrating the concentrations of selected elements (K, Fe, Cu, U, Mn, Mg, Al and Ba, analyzed by LA-SF-ICP-MS) as function of the total chlorinity (wt.% Cl calculated from $NaCl + CaCl_2$) for FIA from Prominent Hill. The data comprise pre-, syn- and post-mineralization associated FIA and are sorted by sample type (symbol shape), fluid inclusion type (symbol color) and relative timing with respect to Cu-(Fe) sulfide formation (symbol size). End-member compositions of model fluid types A, B and C are labelled by gray points with capital letters, and calculated mixing lines between them are shown as gray solid lines.

3.4. LA-ICP-MS microanalysis of fluid inclusion assemblages

The combined results of microthermometry and LA-SF-ICP-MS indicate variations in major and trace element concentration and their ratios among petrographically well-constrained FIA that significantly exceed the variation within each FIA (Figs. 10-14; Table A3).

Primary FIA associated with Cu-(Fe) sulfide precipitation in the breccia matrix show a total Cl-salinity between 0.3 and 16.3 wt.% with partly very high K (220–14000 ppm), Fe (310–6000 ppm), Cu (20–5900 ppm), Al (13–830 ppm), Mn, Mg, and Pb. The U concentrations fall into two groups that cannot be discerned petrographically, one with low values of 0.5–2 ppm, while the other has higher concentrations of 38–69 ppm U (Figs. 10-11). In addition, most of their molar Br/Cl ratios in FIA of the LV-type are around 0.003, although values of about 0.006 are found in

20

LVS-type FIA (Fig. 12). Primary LVH(SS)-type FIA in siderite + quartz + fluorite + barite + chalcopyrite veins are Na-dominated and contain some of the highest minor element concentrations including K, Fe (14000–47000 ppm), S, Mn, Cs and Pb, but only moderate Cu (70 ppm) and low U concentrations (typically < 1 ppm). Pseudosecondary and late secondary LVS-type FIA in late calcite + barite + pyrite + fluorite vein samples usually contain intermediate concentrations of K, Fe (200–13000 ppm), Cu (0.9–1300 ppm), S, and typically much lower concentrations of Mn, Cs and Pb.

Total Cl-salinity is the most conservative major fluid component, and Cs and Pb are highly soluble trace elements that are not significantly present as minerals in the deposit. Plotting the Cs and Pb concentration as a function of Cl_{tot} is therefore suitable for discriminating potential fluid types involved in ore formation (Table 2). Figure 13 shows groups of FIA that can be separated into four fluid types A to D, which correlate with the petrographically determined fluid inclusion types and their occurrence as indicated by symbol colors and shapes.

Data of group A mainly comprise primary LV-type FIA hosted in fluorite and barite intergrown with the chalcopyrite- and chalcocite-bearing hematite-aluminosilicate breccia matrix, as well as pseudosecondary LV-type FIA within siderite + quartz + fluorite + chalcopyrite veins. These FIA are weakly saline with ≤ 10 wt.% eqv. NaCl, and are Na-dominated with Ca concentrations typically below the quantification limit of microthermometry and LA-ICP-MS microanalysis (Fig. 8A). Many FIA in group A contain relatively high Cs/Cl_{tot} and Pb/Cl_{tot} ratios compared to their low salinity (Fig. 13), even though the absolute concentrations of most minor and trace elements including Na, K, Fe, Mn, Cs and Pb are low. Despite their low salinity, many FIA contain high concentrations of Cu and U (Figs. 10 and 11). They homogenize by vapor disappearance between 146 ± 12°C and 332 ± 20°C, and most of the petrographically late FIA in this group have higher homogenization temperatures above 210°C.

The data of group B represents primary LVH(SS)-type FIA in siderite + quartz + fluorite + barite + chalcopyrite veins and magnetite + quartz veins. The FIA are NaCl-dominated hypersaline brines with a Ca/Na mass ratio of 0.3. The Cs/Cl_{tot} and Pb/Cl_{tot} ratios of FIA in group B of the siderite-bearing veins are high and well-defined, ranging between 2 and 5, and between 30 and 69, respectively (Fig. 13). The FIA have rather high concentrations of K, Fe, Mn, Cs, Pb and S, variable but mostly low Cu, and invariably low U concentrations generally below the LOD of about 1 ppm (Figs. 10 and 11). Their total homogenization temperatures (by halite dissolution) are between 249 and 269°C in siderite-bearing veins and between 278 and 326°C in magnetite-bearing veins, respectively.

Group C are typically primary LVS-type and some secondary LV-type FIA hosted in fluorite and barite of the bornite + chalcocite-bearing hematite-aluminosilicate breccia matrix. They show intermediate total (NaCl + CaCl$_2$) salinity and are NaCl-dominated but are relatively calcic FIA with Ca/Na mass ratio near 0.6. The Cs/Cl_{tot} and Pb/Cl_{tot} ratios are low compared to their salinity, ranging from 0.1 to 0.4, and from 0.5 to 7, respectively (Fig. 13). These FIA have low K, Fe, Cs and Pb concentrations for their intermediate salinity and lie mostly well below possible mixing trends between the lower-salinity group A and the higher-salinity group B. Their Cu and U concentrations are highly variable (Figs. 10 and 11).

Group D comprises typically pseudosecondary and secondary LV- and LVS-type FIA hosted in fluorite of late calcite + barite + pyrite + fluorite veins, and few clearly post-mineralization LVS-type FIA in breccia matrix samples. They are Ca-dominated brines with higher Ca/Na mass ratios of > 1.2 but similar chlorinity compared with the group C inclusions assemblages. The Cs/Cl_{tot} and Pb/Cl_{tot} ratios are nearly identical among groups C and D (Figs. 13), with overlapping ranges also visible for K, Fe, Mn, Cu and U (Figs. 10 and 11). Group C and D inclusions homogenize between 108 ± 3°C and 323 ± 19°C.
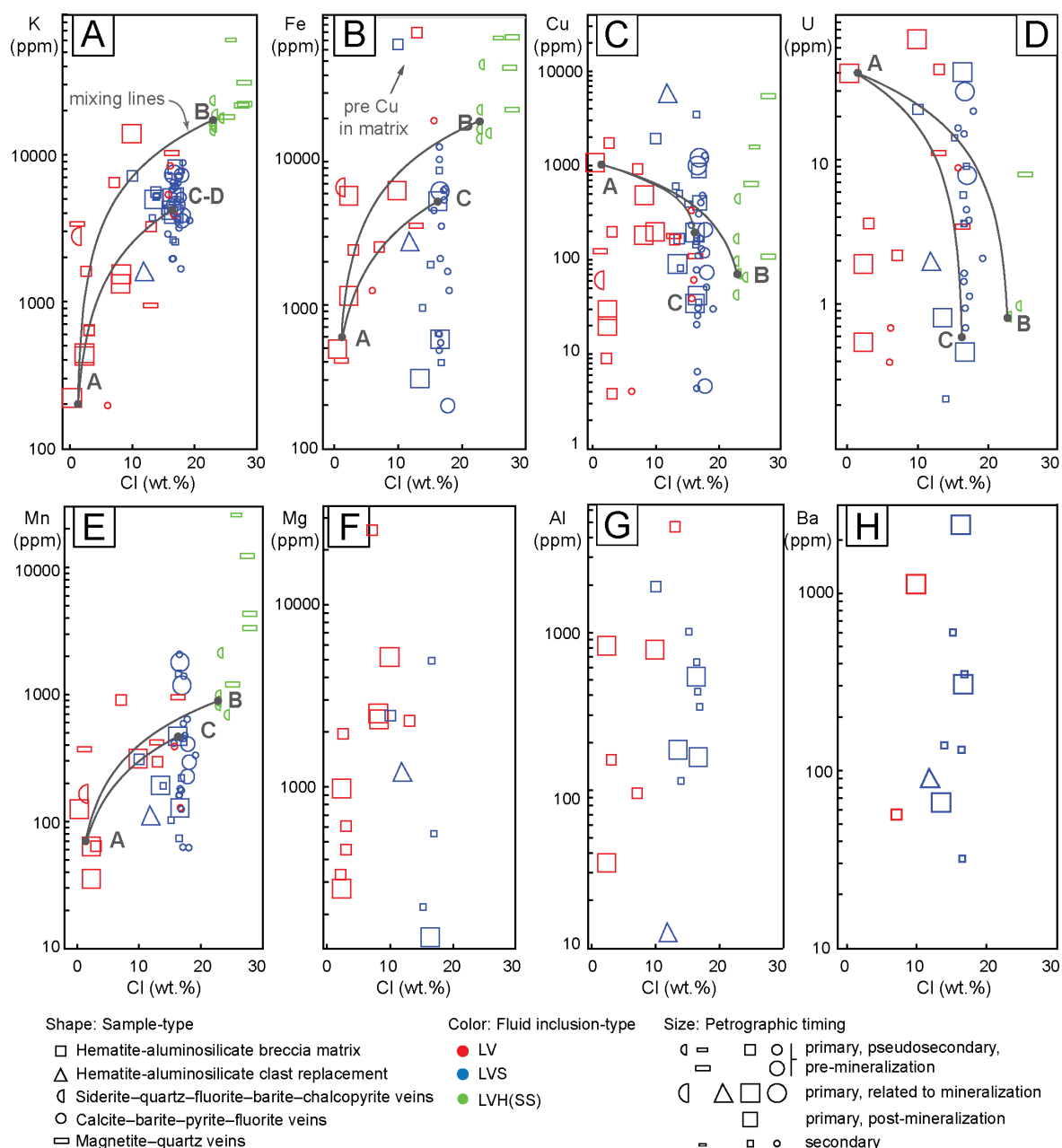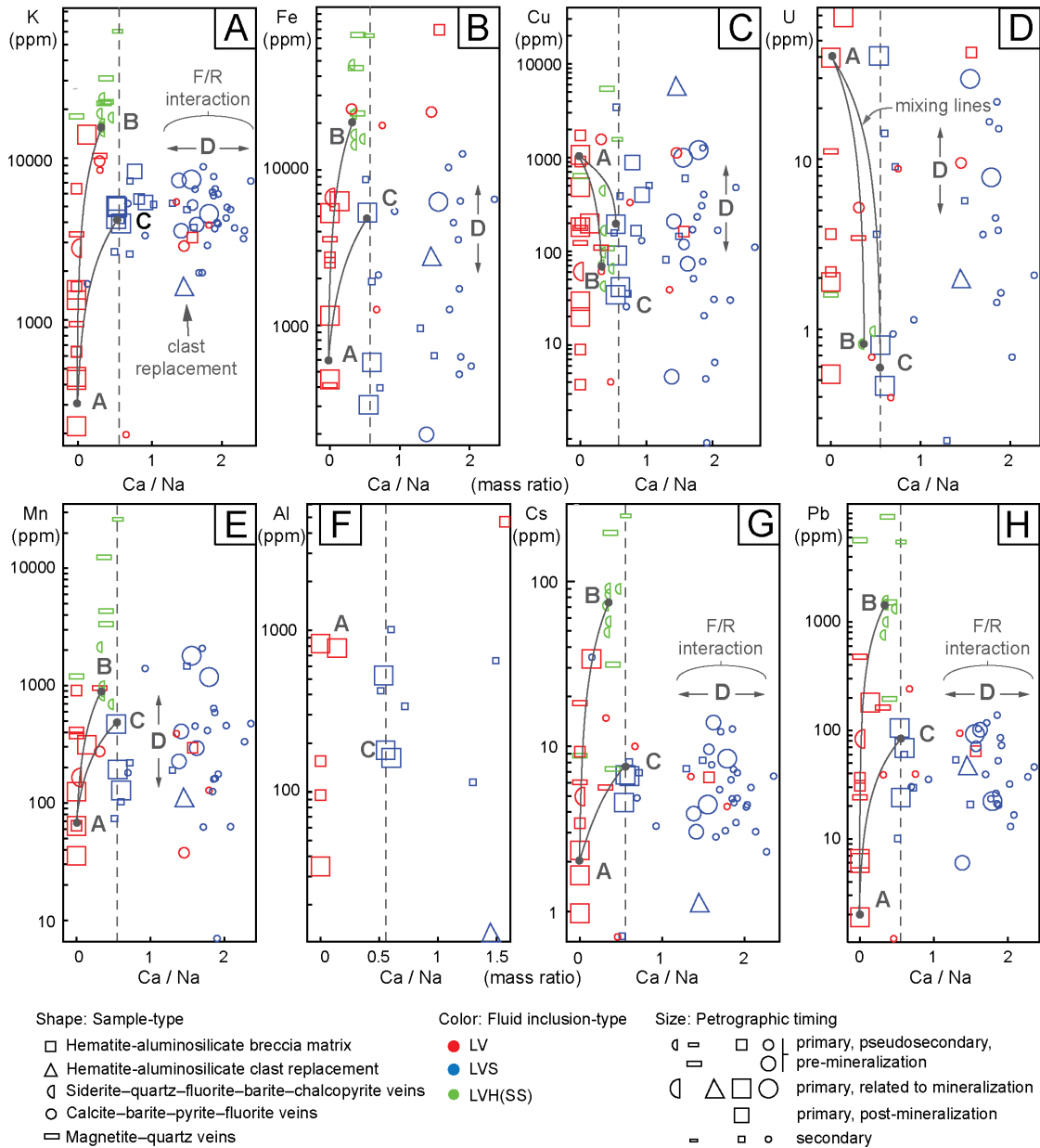
Fig. 11. Variation diagrams illustrating the concentrations of selected elements (K, Fe, Cu, U, Mn, Mg, Al, Cs and Ba analyzed by LA-SF-ICP-MS) as function of the accurate Ca/Na mass ratio (determined from two microthermometric measurements) for FIA from Prominent Hill. The data comprise pre-, syn- and post-mineralization associated FIA and are sorted by sample type (symbol shape), fluid inclusion type (symbol color) and relative timing with respect to Cu-(Fe) sulfide formation (symbol size). End-member compositions of fluid types A, B and C are labelled by gray points and capital letters, consistent with those in Fig. 10. Fluid types A, B and C have Ca/Na mass ratios of about 0.6 or lower. Fluid D has typically Ca/Na mass ratios > 1.4 and rather variable compositions for elements that are modified by fluid-rock interaction. Solid gray lines are fluid mixing lines between model end-member fluids.
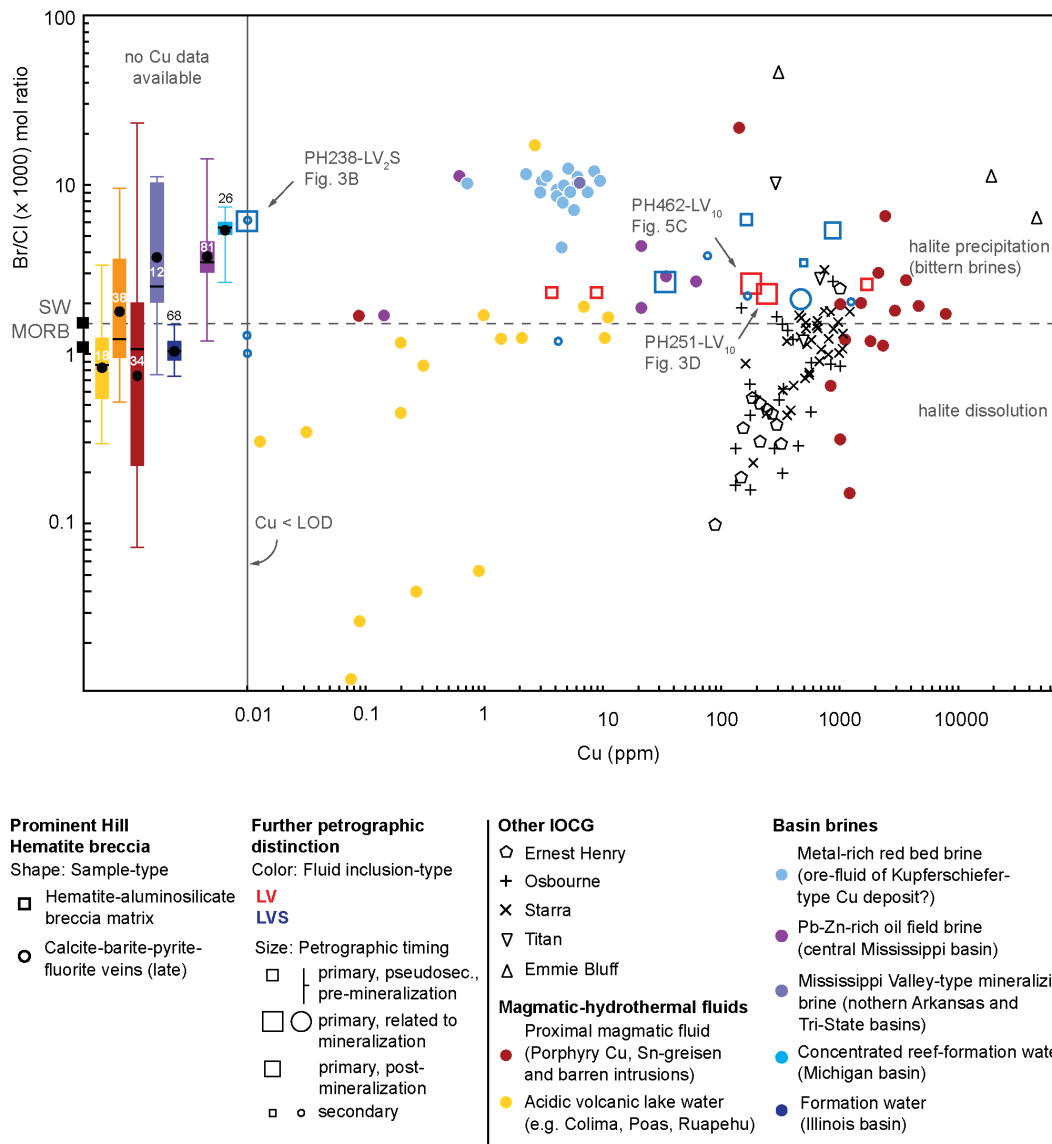
Fig. 12. Variation diagrams of the molar Br/Cl ratio as function of the Cu concentrations, comparing data of the Prominent Hill deposit with data from other Australian IOCG deposits, magmatic-hydrothermal fluids and basin brines. Some FIA from Prominent Hill contain Cu concentrations below the limit of detection (< LOD) of LA-SF-ICP-MS microanalysis and are shown on the line labelled Cu < LOD near the left edge of the diagram and next to box plots showing halogen ratios of fluid types for which no Cu concentration data is available in the literature. Data from Prominent Hill are sorted by sample type (symbol shape), fluid inclusion type (symbol color) and relative timing with respect to Cu-(Fe) sulfide formation (symbol size). Data for the IOCG deposits in the Cloncurry district are from Williams et al. (2001) and Baker et al. (2008); data for the Olympic Dam district are from Bastrakov et al. (2007) and are micro-PIXE analyses of single inclusions; data for fumaroles, acidic volcanic lake water and proximal magmatic fluids are from Symonds et al. (1990); Böhlke and Irwin (1992); Cline and Vanko (1995); Taran et al. (1995); Williams-Jones and Heinrich (2005); Nahnybida et al. (2009); Seo et al., (2011) and Henley (2015); data for basin brines are form Carpenter et al. (1974); Kharaka et al. (1987); Steuber and Walter (1993); Wilson and Long (1993); Stoffell et al. (2008) and Fusswinkel et al. (2014). The reference value for seawater (SW) is from McCaffrey et al. (1987) and the value for MORB is from Jambon et al. (1995). Box plots show mean values (black circle), median (black line), 50% quartile (central box) and extreme values (whiskers) of data. Abbreviations: LV: liquid–vapor; LVS: liquid–vapor–solid. Individual FIA of particular significance are highlighted and discussed in the text.

Table 2. Description of fluid inclusion assemblage data accumulating in clusters A-D and shown in Figures 8 and 12 including ranges of average concentration of selected elements in different FIA, as determined by microthermometry and LA-ICP-MS microanalysis.

Cluster	A	B	C	D
General description	• Na-dominated fluid, weakly saline fluid • Primary LV-type FIA in barite and fluorite intergrown with Cu sulfide bearing hematite-alumino-silicate breccia matrix • Secondary LV-type FIA in siderite + quartz + fluorite + chalcopyrite veins	• Na-dominated and Ca-bearing hypersaline brine • Primary LVH(SS)-type FIA in siderite + quartz + fluorite + chalcopyrite veins • Barite + chalcopyrite veins • Magnetite + quartz veins	• $CaCl_2$-bearing and NaCl-dominated brine • Primary LVS-type FIA in fluorite and barite of bornite + chalcocite-bearing hematite-aluminosilicate breccia matrix • Late secondary LV-type FIA	• Ca-dominated and Na-bearing brine • Pseudosecondary and secondary LV- and LVS-type assemblages in fluorite of calcite + barite + pyrite + fluorite veins
wt.%				
$NaCl+CaCl_2$	0.6–24	36. 0–45.4	15.7–27.8	18.8–29.5
NaCl	0.6–24	26.0–35.2	9.8–19.9	6.9–11.4
$CaCl_2$	< LOD to 3	6.0–15.7	6.0–15.4	11.5–21.7
Na	0.21–9.1	10.2–13.9	4.0–7.8	0.5–4.5
Ca	< LOD to 1	3.6–5.7	2.4–5.6	4.1–7.8
Cl	0.34– 14.8	22.1–28.0	9.8–17.2	11.8–19.2
Ca/Na	< ~0.1	~ 0.3	~ 0.6	> 1.2
ppm				
K	220–14000	15000–61000	2500–10300	1600–8800
Fe	410–6600 usually < 2400	14000–73000	310–8600 some > 10000	200–13000 some > 21000
S	< 300	4200–8100	230–6000	180–13000 some > 20000
Mn	36–900	690–26000	74-1400	7–2100
Pb	1.9–470	190–9300	10-160	6.0–140
Cs	1.0–34	7.2–250	0.7-15	1.1–35
Cu	4–1900 typically ~400 in pre ore assemblages, some > 800	40–5400 typically ~80 in siderite veins	25–3400 typically ~200	0.9–1200 typically ~130
U	0.5–70	0.8–0.9	0.5–40	0.2–42
ppm/wt.%				
Cs/Cl	0.5–5.2	0.3–9.7	0.1–0.9	0.1–0.82
Pb/Cl	0.8–84	7.0–340	0.6–9.9	0.3–7.3

5. Discussion

Deposit geology, mineralogy, lithogeochemistry, sulfur isotope and fluid inclusion data and some first-order thermodynamic estimates can be integrated into a coherent process model for formation of the Prominent Hill IOCG deposit, which has applications to other hematite-rich deposits in the Olympic IOCG province. It focuses on the key role of magmatism and advocates a dominantly magmatic source of the ore components. The essential difference to porphyry Cu-Au deposits is a stage of wholesale oxidation of magmatic ore fluid components by the oxygenated atmosphere, and subsequent redox reactions involving fluid mixing and fluid–rock interaction, with sulfate as an essential oxidant to explain the iron-rich but sulfide-poor nature of the economic Cu-Au orebodies.

5.1. Constraints from mine-scale geology, alteration mapping and sulfur isotope geochemistry

Zones of hydrothermal alteration and mineralization crosscut primary lithochemical contacts (Schlegel and Heinrich, 2015). This deposit-scale observation suggests steep chemical gradients during reaction between mineralizing fluids focused up within zones of massive hematite-quartz alteration (Fig. 2) and the volcano-sedimentary host rock package with its

ambient fluids. Redox gradients are indicated by highly variable and heterogeneous sulfur isotope compositions of Cu-(Fe) sulfides, from the scale of the deposit to the scale of individual sulfide grains (Schlegel et al., 2017). The range in ∂34S of sulfates and sulfides can be fully explained by partitioning and redox reaction between oxidized and reduced sulfur species of magmatic origin, without requiring input of sulfur from marine or evaporitic sources (Schlegel et al., 2017). The economically important stage II precipitation of chalcocite and bornite derived parts of its sulfur from replacement of pre-existing stage I pyrite and chalcopyrite. Another, likely dominant fraction of sulfur for chalcocite and bornite rich ores originated from magmatic gases that had been released by Gawler Range Volcanics eruptions into the oxygenated hydrosphere. The sulfur isotope data can be explained by complete oxidation of magmatic SO_2 to sulfate and sulfuric acid prior to infiltration into the host rocks (Schlegel et al., 2017). This might have occurred in the vadose zone or as volcanic aerosols, but this would disperse the reactive components by ground water or winds, before they could infiltrate back into the subsurface in significant amounts. We therefore favor a scenario where the magmatic volatiles have interacted with atmospheric oxygen in a volcanic lake environment to produce the acid, metal- and sulfate-rich ore-fluid inferred from fluid inclusions, alteration geochemistry and sulfur isotope data.
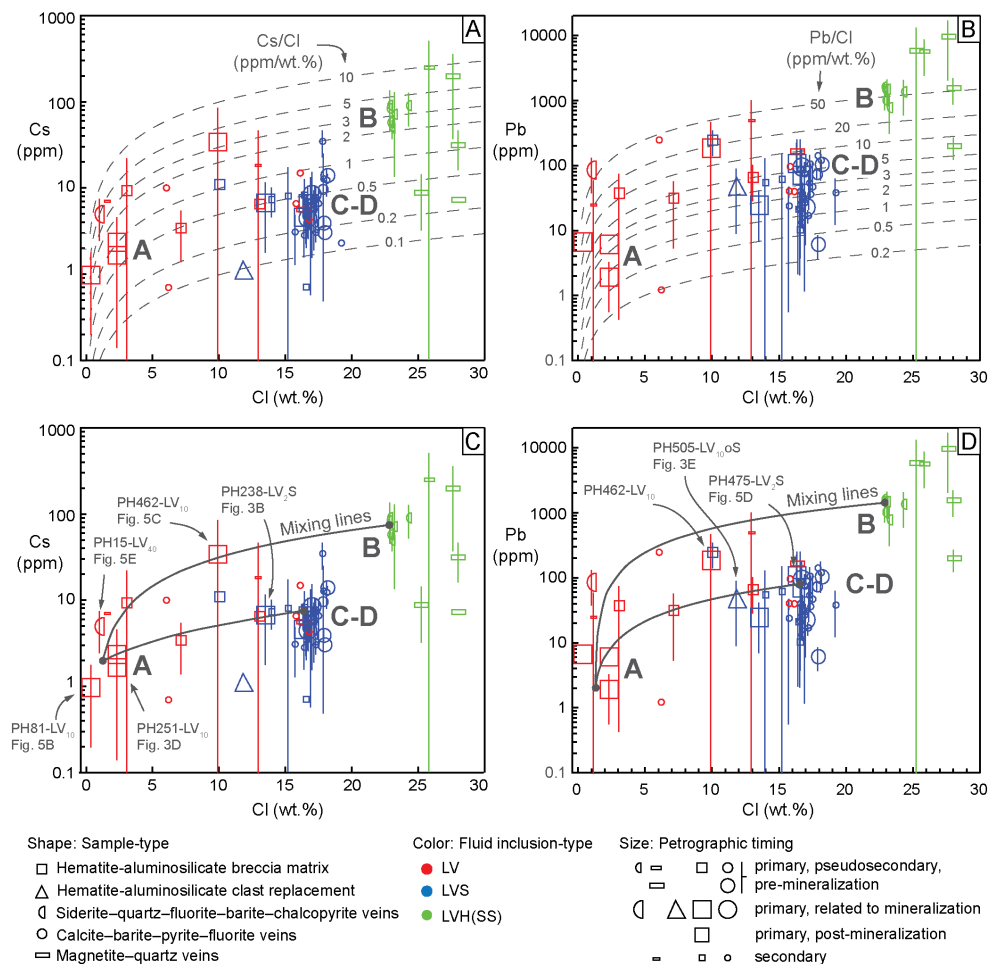
Fig. 13. Variation diagrams of the concentration of Cs (A and C) and Pb (B and D) as function of the total Cl salinity (calculated from NaCl + CaCl₂) for FIA from Prominent Hill. The standard deviations (1 σ) within each FIA are shown by vertical bars. Dashed gray lines in diagrams (**A**) and (**B**) represent trend lines of constant Cs/Cl$_{tot}$ and Pb/Cl$_{tot}$ ratios calculated for fluid dilution with pure water, showing that FIA in group A have lower relative Cs and Pb concentrations than FIA in group B. Fluids in groups C and D have approximately the same Cs and Pb contents. Solid gray lines in (**C**) and (**D**) represent calculated mixing lines between end-member fluid compositions (gray dots), i.e. fluid mixing lines between A and B or between A and C. The data are sorted by sample type (symbol shape), fluid inclusion type (symbol color) and relative timing with respect to Cu-(Fe) sulfide formation (symbol size). Individual samples and FIA of particular significance are highlighted and discussed in the text.

5.2. Four end-member fluids involved in the hydrothermal evolution of Prominent Hill

Fluid inclusion assemblages associated with ore formation at Prominent Hill record large and analytically significant variations in total salinity, Ca/Na ratios, and Fe, Cu, U and most trace-element concentrations (Figs. 8, 10 and 11). By contrast, the concentrations of Cs and Pb vary much less and appear to be unaffected by mineral precipitation (no galena has ever been reported) or fluid–rock reactions (no systematic Pb or Cs enrichment or depletion is observed in altered rocks; Belperio, 2002; Carter et al., 2003; Belperio and Freeman, 2004; Belperio et al., 2007; Freeman and Tomkinson, 2010; Schlegel and Heinrich, 2015). Considering Cs and Pb as largely conservative fluid components, we can identify four fluid types A through D (Fig. 13). Using their ranges of K, Fe, Mn, Cu, and U concentrations, we have reconstructed the likely composition of four end-members fluids labelled A to D in Figures 10 to 12. The Cu concentration of fluid end-members A and B are estimates based on weighted Cu concentrations of primary, pre-mineralization FIA. Similarly, the Cu concentrations in fluid end-members C and D are averages in primary, pre-mineralization FIA. The variability in elemental composition in FIA of the three fluid inclusion types and four main compositional groups makes the definition of end-member fluids somewhat subjective, but they allow testing possible fluid processes.

The sources of the end-member fluids may be inferred from global comparison with fluid compositions from different hydrothermal environments. The Br-Cl systematics of sedimentary brines has been widely used as a tracer for the origin of the salinity (e.g. Carpenter et al., 1974; Hanor, 1994; Kharaka and Hanor, 2003). Comparison with fluid inclusion data from magmatic-hydrothermal fluids show that molar Br/Cl signatures are not unique to a specific reservoir (Fig. 12). Nevertheless, texturally-controlled LV-type FIA from Prominent Hill ores range between magmatic values and bittern brines and also resemble values characteristic for acidic volcanic lake water. Most of the LVS-type data overlap with the few micro-PIXE analyses of individual inclusions from other prospects in the Olympic IOCG province (Emmie Bluff and Titan) that have higher Br/Cl, between those of modern seawater and residual bittern brines (Bastrakov et al., 2007). By contrast, high-temperature IOCG deposits of the Cloncurry district contain fluids with low Br/Cl ratios, indicating a contribution from halite dissolution (Williams et al. 2001; Baker et al., 2008) that is consistent with geological evidence of regional metamorphism of evaporites (Oliver et al., 2004). Insufficient data are published to compare trace-element concentrations like Cs and Pb, but ratios among major and minor solute components including Na, K, Ca and Mn allow a first-order comparison with magmatic fluids, fumaroles, acidic volcanic lake water, basin brines and skarn-forming fluids (Fig. 14) leading to the following interpretation.

End-member fluid A is a low salinity fluid with nominated 1.3 wt.% eqv. NaCl and no detectable $CaCl_2$. The molar Br/Cl ratios in FIA dominated by fluid A (e.g., PH81-LV_{10}, PH251-LV_{10} and PH462-LV_{10}, in Figs. 12-14) are typical for magmatic fluids, acidic volcanic lake water and evaporated bittern brines (Fig. 12). Fluid inclusion assemblages approximating the composition of end-member fluid A have Cs/Cl_{tot} or Pb/Cl_{tot} ratios that are close to those of fluids B or C and D (Figs. 13), but they contain significantly higher Cu and U concentrations at much lower salinity (Fig. 10). Thus, fluid A cannot be produced by dilution of one of the more saline fluids B, C or D. End-member fluid A is the main ore fluid and is approximated by 1000 ppm Cu and 40 ppm U, which can be readily achieved if the fluid was highly acidic and highly oxidized (Bastrakov et al., 2010). Clearly detected Al in FIA dominated by end-member fluid A (Fig. 11F) is also consistent with a highly acidic fluid (Hemley et al., 1980; Reed, 1997; Tagirov and Schott, 2001) and can explain the large-scale Al leaching in the core of the alteration system at Prominent Hill (Schlegel and Heinrich, 2015) and Olympic Dam (Ehrig et al., 2012). The high U concentration implies that the oxidation state was well above the hematite/magnetite buffer and precludes significant co-transport of reduced sulfur along with the Cu and U. Limited microanalytical data for total S in FIA approximating end-member fluid A (up to 300 ppm) leave the possibility that the ore fluid A was transporting substantial amounts of sulfate or sulfuric acid.
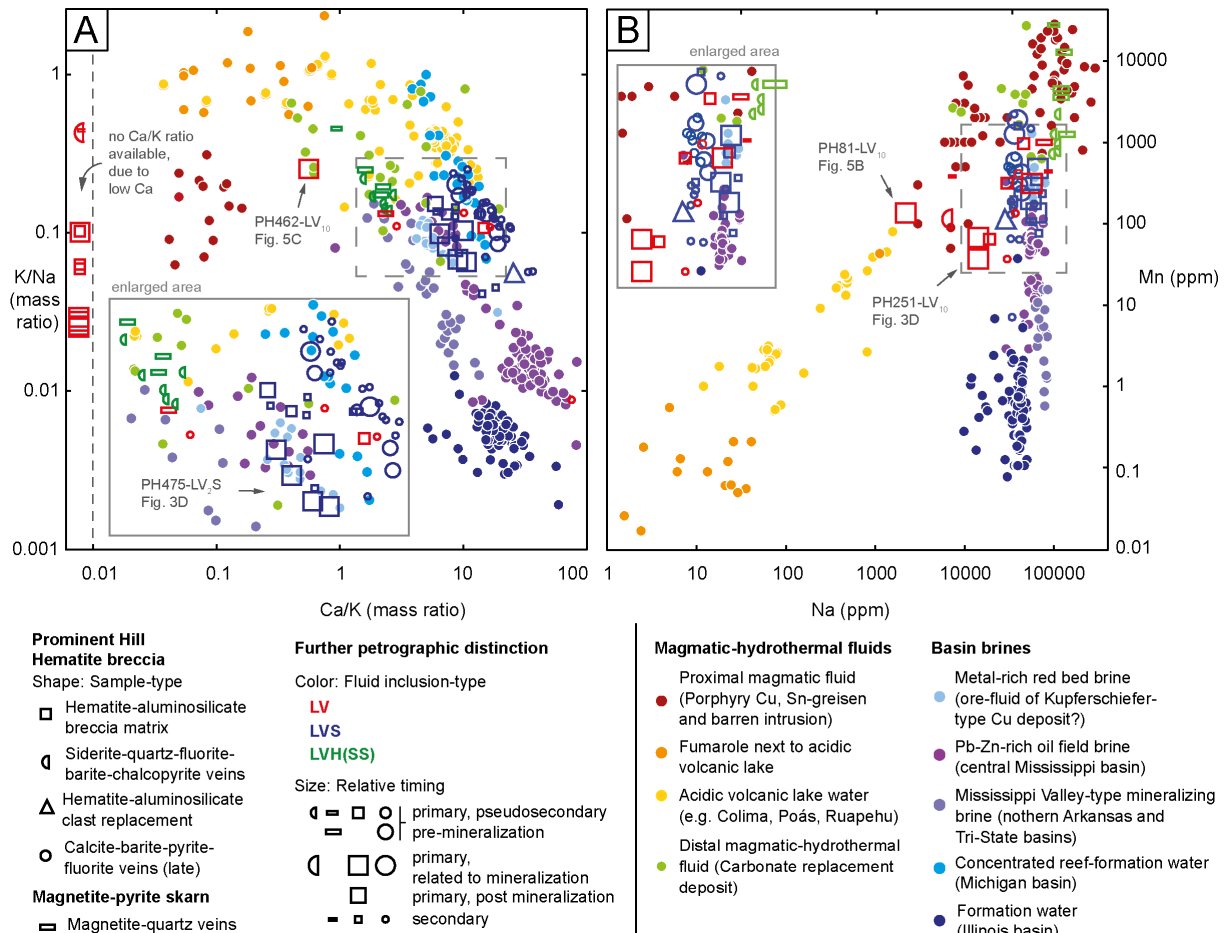
Fig. 14. Variation diagrams comparing the chemical characteristics of FIA of the Prominent Hill deposit with magmatic fluids released from granites, fumaroles, modified magmatic-hydrothermal fluids from acidic volcanic lake water, distal base-metal skarn deposit, and basin brines (modified from Samson et al., 2008). Data from Prominent Hill are sorted by sample type (symbol shape), fluid inclusion type (symbol color) and relative timing with respect to Cu-(Fe) sulfide formation (symbol size). Data for the El Mochito skarn and Mexican carbonate-replacement deposits are from Samson et al., (2008); Williams-Jones et al., (2010), and Haynes and Kesler (1988); data for proximal magmatic fluids are from Cline and Vanko (1995), and Williams-Jones and Heinrich (2005); data for fumaroles and volcanic lake water are from Symonds et al. (1990); Rowe et al. (1992); Christenson and Wood (1993); Sriwana et al. (2000); Taran et al. (2001); Bernard et al. (2004); Henley (2015); and Varekamp et al. (2015); data for oil field and other basin brines are from Carpenter et al. (1974); Kharaka et al. (1987); Lundegard and Trevena (1990); Connolly et al. (1993); Steuber and Walter (1993); and Wilson and Long (1993); Stoffell et al. (2008), and Fusswinkel et al. (2014). Abbreviations: LV, liquid–vapor; LVS, liquid–vapor–solid; LVH(SS), liquid–vapor–halite + solids.

The FIA representing fluid A have low Ca contents, which, together with the comparatively high K contents, suggests a magmatic-derived salt component. Their low Ca/K and K/Na mass ratios are similar to the ratios of FIA from proximal magmatic fluids, whereas the Ca/K ratio of FIA PH462-LV$_{10}$ (Figs. 5A-C, and 12-14), being also part of group A (Fig. 8), plots close to the transition to more distal magmatic fluids in fumaroles, acidic volcanic lake water and carbonate replacement deposits (Fig. 14A). Moreover, the absolute Na and Mn concentrations are comparable to the ones in FIA from barren intrusions, Cu-Au bearing porphyry deposits and acidic volcanic lake water (e.g. PH81-LV$_{10}$, Fig. 14B). Thus, fluid A is interpreted as meteoric water that became enriched in magmatic components by shallow volcanic degassing of late Gawler Range Volcanics, followed by complete oxidation of magmatic sulfur via atmospheric oxygen in a volcanic lake environment. We therefore propose that fluid A has contributed fully oxidized magmatic sulfate to the system, as indicated by sulfur isotope data (Schlegel et al., 2017), because cooling and oxidation of magmatic SO$_2$ produced sulfuric acid according to:

$$4\ SO_2 + 4\ H_2O + 2\ O_2 = 4\ HSO_4^- + 4\ H^+ \tag{1}$$

Surface water rich in sulfuric acid will aggressively leach Cu and U from eruption rubble in the vent, subaerial lavas, and with the wall-rocks of lakes and rivers (Christenson and Wood, 1993). Reaction-path models that simulate interaction of volcanic condensate with andesite, lake water, and reacted condensate show that Cu can become enriched in lake water by three orders of magnitude, reaching ppm levels given enough magmatic heat (Christenson and Wood, 1993). Low-density, oxidized volcanic gas condensates from high temperature fumaroles of basaltic fissure eruptions typically contain 1–6 ppm and locally up to 50 ppm Cu (Menyailov and Nikitina, 1980; Symonds et al., 1990; Henley, 2015; van Hinsberg et al., 2015), but magmatic vapor is able to transport much higher Cu concentrations (e.g., Migdisov et al. 2014). Magmatic vapor expansion in the shallow sub-surface leads to the accumulation of water-soluble, copper-rich condensates in some volcanic environments (Taran et al., 2001; Yudovskaya et al., 2006). Dissolution of such condensates by reacted, but still acidic volcanic lake water is envisaged to yield the Cu-rich ore fluid A containing several hundred ppm of copper as well as significant levels of U.

Given the fluorine-rich nature of the Gawler Range Volcanics magmas (Agangi et al., 2012), the effusive volcanism probably also released HF in gaseous or readily leachable form. The low Ca concentration of fluid A permitted efficient fluorine transport, which is limited by the solubility of fluorite that eventually becomes enriched in the deposit by interaction with more Ca-rich brines (Fig. 5A, C).

Oxidized, Cu-, U- and F-rich and highly acidic fluids reaching the focal area of hematite + quartz alteration in the Prominent Hill deposit requires that surface-derived water charged with magmatic solutes infiltrated during short-lived periods of active volcanic degassing. Acidic weathering and leaching of volcanic rocks on the surface without acidity recharge would have led to fluid neutralization and metal precipitation. The source region of the ore fluid A cannot have been a playa lake as originally proposed for Olympic Dam by Haynes et al. (1995) because such a surface brine would not have been acidic enough to produce the intense hydrothermal alteration, Al-leaching and mineral zonation at Prominent Hill (cf. Schlegel and Heinrich, 2015).

End-member fluid B is the most saline fluid, dominated by NaCl as the main salt component (37 wt.% NaCl+CaCl$_2$) and a moderately low Ca/Na mass ratio of 0.35. Fluid inclusions dominated by end-member fluid B have the highest concentrations of Fe, K, Na, Mn, Cs, and Pb out of all FIA recorded in the deposit, approaching those of magmatic-hydrothermal brines in granite-related systems and skarn (Fig. 14B; Audétat et al., 1998; Ulrich et al., 2001; Audétat et al., 2008; Samson et al., 2008; Kouzmanov and Pokrovski, 2012). They occur in siderite + quartz + chalcopyrite bearing veins cutting the Prominent Hill breccia, recording moderately reduced and less acidic fluids (Fig. 5E). Fluid inclusion assemblages of similar character occur in barren magnetite + quartz veins that cut the weakly mineralized magnetite skarn-like alteration assemblage. These FIA cannot be linked in time across the hanging wall fault, but neither produced economic ore. Fluid B is interpreted as a magmatic-hydrothermal brine partially modified by high-temperature fluid–rock reaction with quartz + feldspar ± carbonate bearing rocks, which increased the Ca/Na ratios in the fluid to a moderate degree (Dolejs and Wagner 2008; Hennings et al., 2017) compared with pristine magmatic fluids (Fig. 14A). Replacement of feldspar- and carbonate-rich rocks by albite, magnetite and hematite at Joe's Dam (Freeman and Tomkinson, 2010) in the vicinity of the fluid-saturating White Hill gabbros at 1562 ± 14 Ma, supports a magmatic source of fluid B, modified by exchange of Na for Ca. The magmatic origin of fluid B is also confirmed by the sulfur isotope signature of pyrrhotite and chalcopyrite hosted in magnetite-bearing miarolitic cavities in the gabbroic intrusion (Schlegel et al., 2017). These observations and the high temperature of FIA of group B, including some potential high-temperature mixtures between fluids A and B in late-stage ore veins (Figs. 9D and 10), imply that magmatism was active during the formation of the deposit.

We considered the alternative possibility that fluids A and B represent an immiscible pair of magmatic brine and vapor that had originally coexisted and separated during accent into a low-density vapor and high-salinity brine. Indeed, a few vapor-rich inclusion are present in a siderite-bearing vein sample (PH15), but no low-density FIA are observed in mineralization-

relevant matrix samples or as boiling trails associated with LVH(SS)-type fluid inclusions. Phase separation of magmatic fluids typically results in vertically extensive quartz vein networks and dominantly quartz-cemented breccias, as seen in most porphyry Cu deposits in obvious contrast to the replacive hematite-cemented breccias observed at Prominent Hill. Although recurrent hydrothermal brecciation was described by Belperio et al. (2007), the early interpretation is inconsistent with more recent observations (cf. Freeman and Tomkinson, 2010; Bull et al., 2015; Schlegel and Heinrich, 2015; Allen et al., 2016; Schlegel et al., 2017; Williams et al 2017 a, b). Nevertheless, the solute components in fluids A and B are ultimately sourced from magmas with similar composition, but the two distinct fluids have evolved along different fluid-flow pathways in the system.

End-member fluid C is a sodic-calcic brine with an intermediate salinity of 27 wt.% (NaCl + $CaCl_2$) and a Ca/Na mass ratio of 0.6. It contains less Fe than fluid B, but primary mineralization-associated LVS-type FIA similar to fluid C (Fig. 10) contain about 200 ppm Cu. Based on the elevated molar Br/Cl ratios (for example LV_{10} assemblages in sample PH238 approximate end-member fluid C; marked in Figures 12 and 13), halite dissolution can be excluded as the source of salinity of fluid C, but a component of magmatic salinity is possible besides contributions from sedimentary rocks or bittern brines. The Pb/Cl ratios of fluid C are similar to ratios in metal-rich basin brines (Stoffell et al., 2008; Wilkinson, 2013; Fusswinkel et al., 2013; Wagner et al., 2016). The ranges in Ca/K and K/Na mass ratios support this interpretation, because FIA similar to fluid C closely overlap with data from red bed brines, interpreted as modified ore fluids of Kupferschiefer type Cu mineralization (Fusswinkel et al., 2014). Moreover, our data overlap with metalliferous oil field brines from the central Mississippi basin and some basin brines in northern Arkansas (Fig. 14). Fluid C contains elevated Cu concentrations (but less than Fluid A despite its higher salinity) that may have been liberated from reactive glass-rich volcaniclastic material in the sedimentary host sequence. FIA approximating end-member fluid C contain about 500 ppm sulfur which is typical for the sulfate content for basin brines with 30 wt.% total salinity (Hanor, 1994). The variability in Cu and S concentrations of FIA similar to fluid C can be explained by variable degrees of fluid-rock interaction and release of pore fluid during replacement of the sedimentary host sequence. Sulfur isotope data show no evidence for major sulfate contributions from a sedimentary-evaporitic source but are readily explained with partial inheritance of S from pre-existing pyrite in the host rock sequence (Schlegel et al., 2017).

End-member fluid D is a calcic-sodic brine with total salinity (25 to 29 wt.% NaCl+$CaCl_2$) similar to fluid C, but with a very high Ca/Na mass ratio of about 2. The FIA of group D (Fig. 8) occur in late calcite + barite + fluorite bearing veins that host minerals of the ore stage with calcite as a characteristic mineral. Fluid inclusions dominated by fluids C or D show a continuum in their Ca/Na ratio (Fig. 11), but have rather constant and distinct Cs/Cl and Pb/Cl ratios (Fig. 12). The Ca/Na ratio of fluid D is much higher than in typical basin brines, only matched by low-temperature brines in (a) crystalline shields (basement brines; Frape et al., 1984; Frape and Fritz, 1987; Lodemann et al., 1998; Bottomley et al., 2005), (b) post-ore fluids in gold-bearing quartz vein deposits (Boullier et al., 1998; Wilkinson et al., 1999; Turner et al., 2001) and (c) in retrograde metamorphic settings (e.g., Heinrich et al., 1989). Published results of thermodynamic modeling indicate that the high Ca/Na ratio probably developed by reaction with plagioclase-rich rocks at low temperature and very low fluid/rock ratio (Heinrich et al., 1995; Dolejs and Wagner, 2008; Hennings et al., 2017). Such rock reaction must therefore have occurred on a large scale, extending well beyond the area of the Prominent Hill deposit and the region of local ore-fluid-related heating. Despite its involvement in clast replacement (e.g. Fig. 3E; PH505-LV_{10}oS marked in Fig. 11A), fluid D plays no major role in economic Cu-Au mineralization, as petrographic observations show that it typically postdates sulfide precipitation in the breccia matrix (Fig. 11). More locally, it may have been significant for remobilization of Cu, because FIA approximating the end-member fluid composition are abundant in fluorite of late calcite + barite + pyrite ± fluorite ± chalcopyrite veins.

5.3.   Fluid mixing drives IOCG mineralization

Economic Cu-Au mineralization at Prominent Hill is interpreted to be the consequence of concurrent fluid mixing and fluid–rock reaction. Calculated mixing lines between end-member fluid compositions indicate that the entire spectrum of primary pre-, syn- and post-mineralization FIA in the breccia matrix can be explained by mixing between fluids A and B and between fluids A and C (Figs. 10, 11 and 13). Most FIA related to the main stage of copper mineralization are of variably low to intermediate salinity (1–15 wt.% Cl_{tot}) with a signature of conservative trace elements dominated by fluids A and C (straddling the lower mixing lines in Fig. 13C, D). Thus, mixing of fluid A with fluid B and with fluid C is interpreted to have dominated the deposition of hematite, low-sulfidation Cu-(Fe) sulfides and the main gangue minerals including fluorite and barite in the Prominent Hill high-grade orebody.

We interpret fluid A to be the main ore fluid contributing most of the Cu, the relatively small amount of U at Prominent Hill (compared to the U-rich Olympic Dam deposit) and oxidized sulfur as sulfuric acid. Sulfate is a critical component for our mineralization model, because it represents the main oxidant for ferrous iron even though only a few S concentrations with large analytical uncertainty have been measured above the limit of detection. Fluid B is inferred to have contributed a limited amount of sulfur as reduced aqueous sulfide, as well as a high fraction of the total Fe that caused iron oxide deposition. Fluid C contributed some Cu at Prominent Hill, particularly in peripheral zones with lower ore grades. This fluid mixing scenario involves three main reservoirs of dominant ore-forming components, by precipitation reactions of ore minerals that additionally depend on fluid–rock reactions for acid neutralization, as discussed in the following section.

5.4.   Alteration and redox reactions driving hematite and

Cu-(Fe) sulfide deposition

Neutralization of acidic fluid is evident from replacement textures of host rock components, and appears to have exerted a critical control on the localization of the highest grade chalcocite + bornite + hematite + sericite ores (Fig. 2). The main source of acidity is the disproportionation of magmatic sulfur and wholesale oxidation of SO_2 and H_2S in fluid A via Eq. (1). An additional source of H^+ is the reduction of sulfate (e.g., transported by fluid A) matched by oxidation of Fe^{2+} (contributed by saline fluids B or C) to precipitate hematite (Haynes et al. 1995, their eq. 1):

$$HSO_4^- + 8\ Fe^{2+} + 8\ H_2O = 4\ Fe_2O_3 + H_2S + 15\ H^+ \qquad (2)$$

In the absence of sulfate or any other abundant oxidant, some hematite may precipitate from reaction with water alone (Barton et al., 2014), according to:

$$3\ H_2O + 2\ Fe^{2+} = Fe_2O_3 + H_2 \quad + 4\ H^+ \qquad (3)$$

However, even with ample supply of Fe^{2+} from reduced brines and a sink for H^+ in acid-consuming alteration reactions discussed below, the progress of reaction (3) is limited by the production of H_2. An upper limit of H_2 in the mixed fluid is defined by the stability of hematite itself, where magnetite would precipitate instead of the ubiquitous hematite at Prominent Hill:

$$3\ Fe_2O_3 + H_2 = 2\ Fe_3O_4 + H_2O \qquad (4)$$

The equilibrium constant of this reaction (expressed with H_2 as aqueous species) according to SUPCRT92 (Johnson et al., 1992) is log K_4 = 5.9 at 200°C and 4.8 at 300°C. Considering that log K_4 = – log $aH_{2,aq}$, the field of possible hematite precipitation is constrained to a maximum molality of H_2 in solution of about 10^{-5} m or 0.02 ppm H_2 by weight. Comparing this limiting H_2 molality with the roughly 10000 times higher molalities of Fe in the analyzed brines (0.1 $m \sim 0.5$ wt.% in fluid end-member C, even higher in brine B), we conclude that reaction (3) can at best precipitate a tiny fraction (0.2 ‰) of the available Fe. It is therefore an inefficient and unlikely process for generating highly hematite-enriched rocks. Hematite precipitation is far more efficient if Fe^{2+} reacts with a more abundant oxidant. The obvious candidate is sulfate, present at hundreds of ppm (300 ppm S ~ 0.01 m sulfate) or more. From these approximate calculations based on our fluid analyses at Prominent Hill, sulfate-driven hematite precipitation by reaction (2) is at least 4000 times more effective than by reaction (3).

Reactions precipitating copper sulfides in the stability field of hematite are also likely to be balanced by the dominant redox species in the fluids, S and Fe. Copper is originally present as Cu(II) under atmospheric O_2 conditions, but is still very soluble as Cu(I) complexes throughout the stability field of hematite + sulfate (Brown, 2014). Expressed by reactions starting with Cu^{2+} and sulfate (both fluid A), chalcocite and bornite may co-precipitate directly with hematite by mixing with an Fe^{2+}-rich brine (fluid B or C), effectively using the sulfide produced by reduction of sulfate with Fe^{2+}:

$$2\ Cu^{2+} + HSO_4^- + 10\ Fe^{2+} + 11\ H_2O = Cu_2S + 5\ Fe_2O_3 + 23\ H^+ \tag{5}$$

$$5\ Cu^{2+} + 4\ HSO_4^- + 37\ Fe^{2+} + 38\ H_2O = Cu_5FeS_4 + 18\ Fe_2O_3 + 80\ H^+ \tag{6}$$
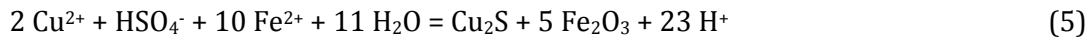
Isovolumetric replacement of pre-ore pyrite (stage I) by chalcocite and bornite (Schlegel et al., 2017) involving Cu^{2+} transported in fluid A will further contribute to redox-balanced copper deposition according to:

$$14\ Cu^{2+} + 5\ FeS_2 + 12\ H_2O = 7\ Cu_2S + 5\ Fe^{2+} + 3\ HSO_4^- + 21\ H^+ \tag{7}$$

$$70\ Cu^{2+} + 36\ FeS_2 + 64\ H_2O = 14\ Cu_5FeS_4 + 22\ Fe^{2+} + 16\ HSO_4^- + 112\ H^+ \tag{8}$$
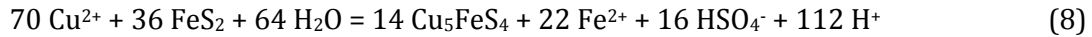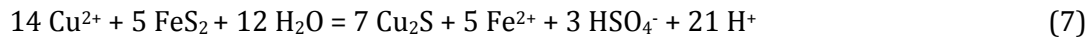
The replacement reactions liberate sulfate and aqueous iron that may in turn promote reactions (2), (5) and (6) to precipitate additional hematite and copper sulfides. Considering the sulfur balance in these two reactions, 71% (chalcocite reaction 7) or 64% (bornite reaction 8) of the copper is precipitated by recycling pyrite sulfur, while 29% or 36% of the copper is precipitated by sulfate reduction. We cannot quantify the relative contributions of pyrite replacement and sulfate reduction to copper enrichment at the scale of the orebody but the distribution of sulfide textures along representative cross sections of the orebody (Fig. 2) show that replacement of pyrite dominates, except in the most highly mineralized hematite-aluminosilicate breccia.

Major production of H^+ is common to all Fe and Cu precipitation reactions (2) and (5) to (8), which means that acid-consuming alteration will promote the deposition of hematite and Cu-sulfides by any of these reactions. Acid consumption is effected at Prominent Hill by replacement of abundant carbonates and feldspars in the host rock package and subsequently by replacement of other aluminosilicates if the preceding rock buffer capacity are exhausted.

The replacement of carbonates according to:

$$2\ H^+ + CaCO_3 = Ca^{2+} + CO_2 + H_2O \tag{9}$$
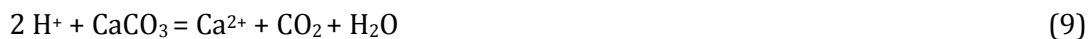
can be combined with essential solute components of the three fluids involved in ore formation. Specifically, mixing of the sulfate (and fluorine) bearing fluid A with the iron-rich fluid B (or C) and concurrent replacement of carbonates results in precipitation of hematite, while H_2S is used for sulfide precipitation and Ca^{2+} is released to the fluid (or used for fluorite precipitation). Combining the redox-balanced precipitation of Fe^{2+} to hematite by sulfate (reaction 2) with calcite dissolution (reaction 9) yields:

$$HSO_4^- + H^+ + 8\,Fe^{2+} + 8\,CaCO_3 = 4\,Fe_2O_3 + 8\,Ca^{2+} + 8\,CO_2 + H_2S \qquad (10)$$

for which the equilibrium constant:

$$\log\,[H_2S]/[HSO_4^-] = \log K - pH + 8\log\,[Fe^{2+}]/[Ca^{2+}] - 8\log\,[CO_2].$$

was calculated using thermodynamic data from SUPCRT92 (Johnson et al., 1992) over a range of temperatures (100 to 300°C) at a pressure of 500 bar. Approximating aqueous activities by molalities (denoted by square brackets) the mass action expression of Eq. (10) can be rearranged to yield the H_2S/HSO_4^- ratio as a function of the Fe/Ca ratio in the fluids or their mixture. Assuming, for a rough order-of-magnitude approximation, that complexation and non-ideality of the two metal ions are similar and cancel, we can insert the analyzed concentrations of 2 wt.% Fe (and 7 wt.% for the most Fe-rich FIA) and 10 wt.% $CaCl_2$ in fluid inclusions approximating fluid B. Figure 15 shows that reaction 10 is thermodynamically very favorable at acidic to neutral pH for any reasonable CO_2 concentration in the fluid, converting essentially all Fe^{2+} and HSO_4^- to hematite and H_2S. Balancing redox as well as the consumption of H^+ by fluid mixing and concurrent replacement of calcite in the host rock, we can combine Eqs. (5) and (6) with Eq. (10) to yield chalcocite, bornite and hematite at the expense of carbonate according to:

$$4\,Cu^{2+}\,(\text{fluid A}) + 2\,HSO_4^-\,(\text{fluid A}) + 20\,Fe^{2+}\,(\text{fluid B}) + 23\,CaCO_3\,(\text{host rock})$$
$$= 2\,Cu_2S\,(\text{chalcocite}) + 10\,Fe_2O_3\,(\text{hematite}) + 23\,Ca^{2+} + 23\,CO_2 + H_2O \qquad (11)$$

$$5\,Cu^{2+}\,(\text{fluid A}) + 4\,HSO_4^-\,(\text{fluid A}) + 37\,Fe^{2+}\,(\text{fluid B}) + 40\,CaCO_3\,(\text{host rock})$$
$$= 2\,Cu_5FeS_4\,(\text{bornite}) + 18\,Fe_2O_3\,(\text{hematite}) + 40\,Ca^{2+} + 40\,CO_2 + 2\,H_2O \qquad (12)$$
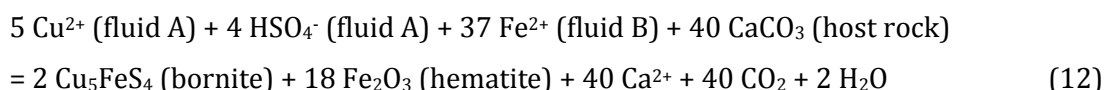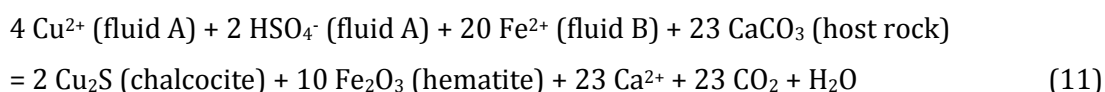
or, considering pyrite replacement (7) and (8) combined with calcite dissolution:

$$28\,Cu^{2+}\,(\text{fluid A}) + 10\,FeS_2\,(\text{host rock}) + 21\,CaCO_3\,(\text{host rock}) + 3\,H_2O$$
$$= 14\,Cu_2S\,(\text{chalcocite}) + 10\,Fe^{2+} + 6\,HSO_4^- + 21\,Ca^{2+} + 21\,CO_2 \qquad (13)$$

$$70\,Cu^{2+}\,(\text{fluid A}) + 36\,FeS_2\,(\text{host rock}) + 56\,CaCO_3\,(\text{host rock}) + 8\,H_2O$$
$$= 14\,Cu_5FeS_4\,(\text{bornite}) + 22\,Fe^{2+} + 16\,HSO_4^- + 56\,Ca^{2+} + 56\,CO_2 \qquad (14)$$
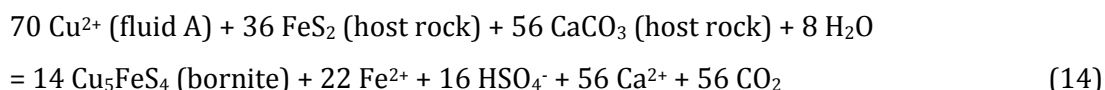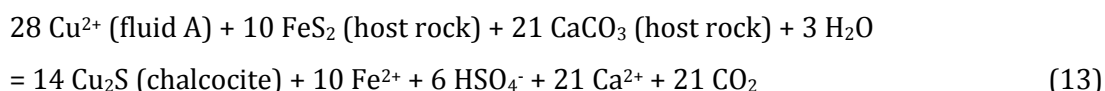
Given an excess of dissolved Fe^{2+} in the iron-rich fluids B or C and considering that HSO_4^- occurs on different sides of Eqs (11) and (12), and Eqs (13) and (14), we recognize that comparatively little HSO_4^- is required to replace large amounts of carbonate by hematite according to reaction (10).

The molar volumes of $CaCO_3$ and Fe_2O_3 are quite similar, thus, breccia porosity (and likely permeability) and fluid focusing would further increase in response to the alteration reactions. Incipient carbonate replacement following Eq. (10) can thus effectively prepare the ground for the pargenetically late copper mineralization (Schlegel and Heinrich, 2015). When the carbonate buffer becomes exhausted or volcanic rocks dominate the local lithology, consumption of H^+ progresses by alteration of alkali feldspars to phyllosilicates by reactions like:

$$3 \text{ KAlSi}_3\text{O}_8 \text{ (K-feldspar)} + 2 \text{ H}^+ = \text{KAl}_3\text{Si}_3\text{O}_{10}(\text{OH})_2 \text{ (muscovite)} + 6 \text{ SiO}_2 + 2 \text{ K}^+ \quad (15)$$
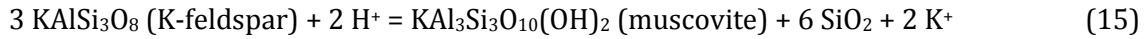
Feldspar replacement textures are observed in the breccia matrix and in clasts at the Prominent Hill deposit. Further aluminosilicate-destructive replacement occurs at the innermost alteration front adjacent to the hematite + quartz core (Schlegel and Heinrich, 2015), possibly according to:

$$2 \text{ KAl}_3\text{Si}_3\text{O}_{10}(\text{OH})_2 \text{ (muscovite)} + 2 \text{ H}^+ + 3 \text{ H}_2\text{O} = 3 \text{ Al}_2\text{Si}_2\text{O}_5(\text{OH})_4 \text{ (kaolinite)} + 2 \text{ K}^+ \quad (16)$$

$$\text{Al}_2\text{Si}_2\text{O}_5(\text{OH})_4 \text{ (kaolinite)} + 6 \text{ H}^+ = 2 \text{ SiO}_2 + 2 \text{ Al}^{3+} + 5 \text{ H}_2\text{O} \quad (17)$$
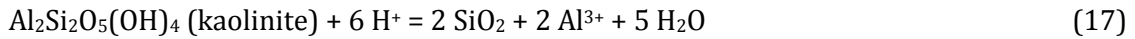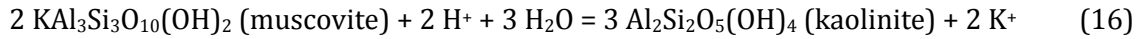
The highest-grade copper ores at the Prominent Hill deposit occur at the transition between the most intense hematite + quartz alteration front (Al-removal) and hematite + chlorite + sericite altered zones. In these high-grade ore zones the main ore-fluid A was neutralized and reduced by reaction with carbonates, aluminosilicates and the Fe^{2+}-bearing fluids B and C (and possibly also Fe^{2+}-bearing minerals like e.g. chlorite). This caused the development of the upward-convex geometry of the high-grade mineralization front (Schlegel and Heinrich 2015). Note that it is not particularly important which host rock acts as an acid neutralizing sink for the large amounts of excess H^+ generated. This sets IOCG mineralization apart from skarn and carbonate replacement deposits, where carbonate host rocks are critical for neutralization of acid fluids.
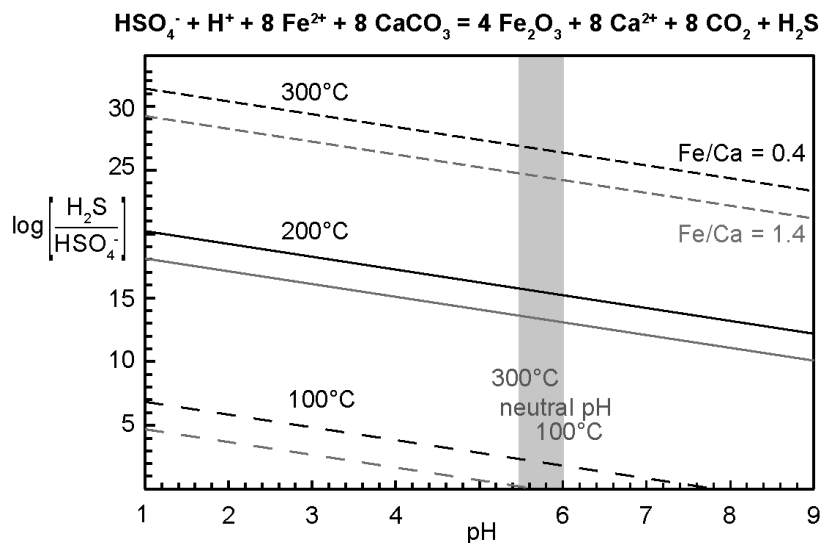
Fig. 15. Diagram showing the calculated H_2S/HSO_4^- molality ratios for the reaction of Eq. (10) as function of pH at temperatures of 100°C, 200°C, and 300°C and 500 bar. Equilibrium constants were calculated using thermodynamic data from SUPCRT92 (Johnson et al., 1992). Activity ratios of Fe/Ca were approximated from concentrations obtained by LA-ICP-MS from fluid inclusions. Two composition of the iron-bearing fluid B were approximated as 30 wt.% NaCl, 10 wt.% $CaCl_2$ with 2 wt.% Fe (black) and 7 wt.% Fe (gray). The diagram shows that the reaction will produce high H_2S/HSO_4^- ratios at all temperatures, which will drive precipitation of Cu sulfides. Variations in pressure between 0.5 and 2 kbar has a negligible effect on the calculated (H_2S/HSO_4^-) ratios. Variations of Fe concentrations as well as of ($NaCl + CaCl_2$) shift the equilibrium somewhat, but do not affect the general result of high (H_2S/HSO_4^-) ratios.

Calcite replacement by hematite from a Fe-rich brine increases the Ca concentration in the fluid, and we therefore need to consider the possibility that the more calcic fluid C (or even fluid D) is the product of a less calcic brine having been modified by ore-related alteration reactions. The calcite replacement reaction, according to Eq. (10), can increase the $CaCl_2$ concentration of fluid B from an initial value of 10 wt.% $CaCl_2$, up to 14 wt.% $CaCl_2$ in the fully rock-reacted fluid. This increase by 4 wt.% $CaCl_2$ is obtained when 2 wt.% Fe dissolved in the fluid are lost as hematite that forms at the expense of calcite. This value is not even close to the much higher $CaCl_2$ concentration of fluid D. Furthermore, we have noted before that fluid B has much higher

ratios of Cs/Cl_{tot} and Pb/Cl_{tot} compared to fluid C (or any mixtures with fluid A). Therefore, fluid D cannot be the product of fluid–rock reaction involving fluid C and the host rocks, because precipitation of all Fe (up to 0.5 wt.%) in fluid C as hematite (which initially contains 10 wt.% $CaCl_2$), would increase the $CaCl_2$ concentration only up to 11 wt.% $CaCl_2$, which is much lower than observed in fluid D. These mass-balance considerations confirm that the more calcic fluid D must originate from outside the orebody and is most likely a brine buffered at variably low fluid/rock ratios by the surrounding rock package.

5.5.   The physical hydrology of the Prominent Hill hydrothermal system

Figure 16 links the proposed chemical fluid process and the observed mineral zonation with the combined geological information in a set of cartoons depicting the possible evolution of the Prominent Hill ore system. Our fluid-chemical arguments require that fluid A flowed from a volcanically active land surface of the younger Gawler Range Volcanics towards the zone of extreme leaching inside the hematite + quartz alteration front at Prominent Hill. Conditions in highly permeable breccias were probably near-hydrostatic at rather shallow depth of a few kilometers, and fluid flow was therefore driven by topographic gradients and/or by thermal convection driven by magmatic heat. Fluid focusing was directed by tectonic breccias, primary flow-top breccias between lava flows, and structures such as unconformities and faults. Secondary permeability produced by the replacement reactions probably contributed significantly to the ore-hosting breccias.

Original deposition of host sediments may have occurred in a fault-bounded basin (Fig 16A, Belperio et al., 2007) and was interrupted by regression and the deposition of red beds above the unconformity separating the main host rock units (Bull et al., 2015). Tectonic brecciation and progressive tilting of the host rock package was probably related to crustal shortening (Fig. 16B, Schlegel and Heinrich, 2015). Part of the early stage I pyrite is of sedimentary origin (diagenetic, partly reworked by early near-surface brecciation; Allen et al., 2016), another part formed in response to magmatic fluids released from crystallizing plutons as pyrite halos extending beyond the limits of magnetite + pyrite alteration (Fig. 16B, Schlegel et al. 2017).

The dominant fluid flow during economic mineralization (Fig. 16C, D) can be explained by a combination of topographic flow and thermal convection, with some injection of magmatic fluid from below. For fluid mixing, the flow indicated in the NS-oriented cartoons in Figure 16C was probably combined with a component of E-W directed flow perpendicular to the plane of these drawings. In the region of the Gawler Range Volcanics, water was flowing downward in recharge areas for fluid A (e.g., from topographically perched volcanic lakes) eventually discharging towards a depression that might have been an E-W-extending valley in the foreland (Fig. 16C). Topography-driven up-flow of fluid A in the discharge area may be assisted by magmatic heat released from crystalizing plutons underneath, granites or gabbros similar to the White Hill intrusion. Furthermore, release of magmatic heat from cooling plutons results in formation of convection cells extending over several kilometers distance (Hayba and Ingebritsen, 1997) supporting downward percolation of fluid A and fluid mixing by reduction of the density of the otherwise denser brines B and C, allowing upward-directed flow of the mixed fluids at Prominent Hill (Fig. 16C and D). Mixing among fluid A and B, advected to Prominent Hill, and their mixing with the brine C resulted in the inverse bell-shaped alteration zones of the high Cu grade ore mined in the Malu pit.
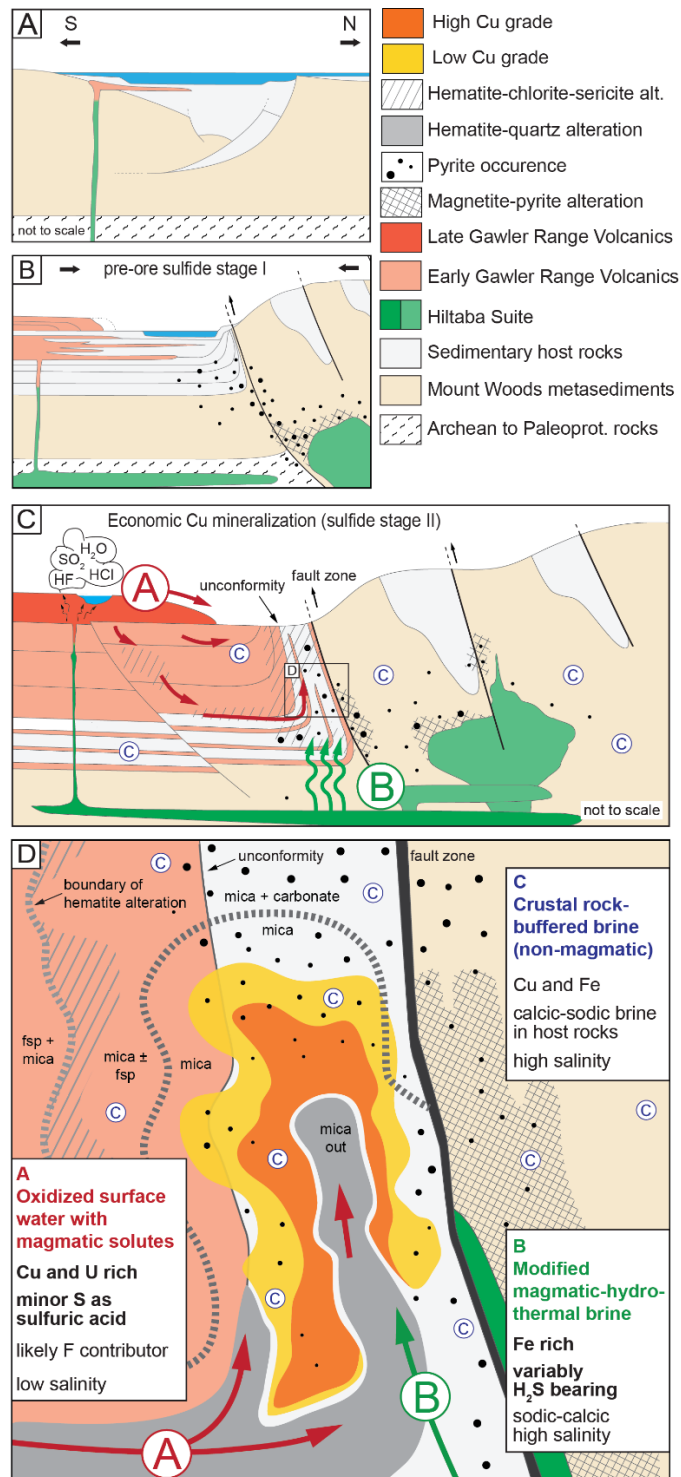
Fig. 16. Conceptual model illustrating the key processes that were driving sulfide stage I and stage II IOCG mineralization in the southern Mount Woods domain. (**A**) Sedimentation of the host-rock package and extrusion of early Gawler Range Volcanics. (**B**) Continued extrusion of Gawler Range Volcanic, intrusion of the Hiltaba Suite granites and sediment input derived from the orogenic front. Deposition of stage I sulfides by circulation of magmatic-hydrothermal fluids sourced from a peripheral intrusive center. (**C**) Regional perspective of fluid processes leading to the economic Cu-Au mineralization. Late volcanism produces the highly oxidized Cu and U rich ore fluid A, possibly in an acidic volcanic lake environment, which then mixes with fluids B and C and deposits the high-grade Cu sulfides at Prominent Hill. Arrows indicate the flow paths of the principal fluids the ore fluid A (red) migrating along oxidized aquifers including the unconformity (Bull et al., 2015), the magmatic-hydrothermal brine B (green) and the basin brine C (blue). Fluid flow was driven by topography and high heat flow related to ongoing igneous activity. (**D**) Illustration summarizing the key observations and interpretations, based on a type section in the Malu pit at Prominent Hill. The section shows the upward convex-shaped shell of high-grade Cu-(Fe) sulfide mineralization located at the transition between hematite + quartz and hematite + chlorite + sericite ± siderite alteration and highlights fluids involved in economic sulfide stage II (modified from Schlegel and Heinrich, 2015).

35

5.6. Comparison with porphyry copper and sediment-hosted copper ore formation

Hematite breccia-hosted IOCG deposits in the Gawler craton have formed by a distinct hydrothermal process that shares aspects with porphyry–epithermal ore systems on one hand (cf. Seedorff et al., 2005; Sillitoe, 2010), and with sediment-hosted Cu deposits on the other hand (cf. Hitzman et al., 2010, Brown, 2014). Apart from their different geodynamic setting in extensional or transtensional large igneous provinces (Richards and Mumin, 2013), IOCG deposits have a number of unique features which set them apart from the subduction-related Cu ore deposits (Table 3). Of these, an explanation for their iron oxide-rich nature is essential, which we propose to be a source of sulfate acting as the essential oxidant for ferrous iron, by oxidizing either precursor magnetite (Gow et al., 1994) or aqueous Fe^{2+} supplied by hot brines (Haynes et al., 1995).

The main mass transfer of ore components including Cu, Fe and S (probably also Au and U) in IOCG deposits in the Gawler Craton can be driven by fluids containing solutes of magmatic origin. Elsewhere, sulfate in particular may also have alternative sources, including seawater or sulfate evaporites (e.g. Oliver et al., 2004; Benavides et al., 2007; Kendrick et al., 2007). Instead of a single magmatic fluid derived from a hydrous intrusion as in porphyry Cu deposit formation (Redmond et al., 2004), hematite-rich IOCG mineralization (disseminated Cu sulfides in hematitic breccia) involves two or more fluids of different origins. Essential components of the high-grade ore at Prominent Hill, i.e., Cu and Fe, are introduced by separate fluids (e.g. Cu in fluid A together with sulfate, and Fe in fluid B). Another important difference between IOCG processes as proposed here for the Gawler craton, compared to porphyry Cu deposits, is that the principal ore fluid in IOCG mineralization forms from comparatively water-poor but hot magmas that release metal-, SO_2- and F-rich volcanic gases into the oxidizing environment close to the Earth's surface, rather than delivering magmatic fluids by hydraulic fracturing into a stockwork of quartz veins. Surface-expelled magmatic components dissolve in dominantly meteoric water, resulting in a low salinity, highly oxidized and acidic aqueous fluid charged with copper and uranium, probably as Cu^{2+} and UO_2^{2+} in the case of Prominent Hill. Based on the results of our fluid inclusion study, hematite-style IOCG mineralization forms in response to fluid mixing and by interaction with reactive host rocks which have a permeability structure facilitating efficient fluid infiltration. A distinct similarity with sediment-hosted Cu deposits is that mineralization also occurs by Cu^{2+} and sulfate reduction, and replacement of pre-ore pyrite which provides a preexisting source of sulfur (Brown, 2014).

The recognition of first-order hydrothermal alteration patterns is essential for locating the ores with the highest Cu grades. By contrast, porphyry Cu deposits contain economic sulfides in quartz-rich stockwork veins (and as disseminations) associated with potassic alteration, which in turn are typically overprinted by lower temperature, more acidic sericite + pyrite ± clay alteration. At Prominent Hill, and probably also at Olympic Dam, the highest Cu grades conform to the boundary between intense hematite + quartz ± barite alteration and the hematite + chlorite + sericite ± siderite alteration, which can be monitored by the hematite-quartz alteration index (Schlegel and Heinrich, 2015). Notably, this mineralogical transition marks a zone where the oxidized and extremely acidic ore fluid was leaving the hematite-quartz breccia, flowing into the hematite-aluminosilicate breccia where it became reduced and neutralized by ferrous iron from magmatic-hydrothermal or ambient basement fluids, and by reaction with chlorite- and carbonate-rich host rocks and formation waters contained in them (Fig. 15D). Even if hydrothermal alteration is considered incidental to the formation of sedimentary Cu deposits in most places (Brown, 2014), their highest Cu ore grades (and associated Au and PGE mineralization) also occur at the interface between oxidized red beds and more reduced lithologies such as carbonaceous and calcareous host rocks (Hitzman et al., 2010; Brown, 2014). The Cu-rich fluids flowed from oxidized into more reduced rocks, where they became reduced, notably at a distinct redox transition. This is a feature which resembles the ore grade and alteration structure of IOCG deposits. Host rock chemical composition appears to be of greater importance in IOCG and sediment-hosted Cu formation than in porphyry Cu mineralization. This is partly because reactive calcareous sedimentary and volcaniclastic host rocks including their

connate waters are not only chemical traps where Cu sulfides (and Au) precipitate, but they also contribute metals (i.e. Cu and Fe) via fluid–rock reactions that facilitate the development of redox and pH gradients.

6. Conclusions

Our data are consistent with a magmatic-hydrothermal origin for the hematite breccia-hosted Prominent Hill IOCG deposits and probably for other hematitic deposits in the Gawler Craton. The proposed process of ore formation differs from that of porphyry–epithermal metalliferous systems by release of magmatic fluids to a surface reservoir in a continental volcanic environment. This leads to complete atmospheric oxidation of magmatic copper and sulfur, preparing a sulfur-bearing but sulfide-depleted and acidic ore fluid. Subsequent copper sulfide deposition is partly linked to hematite deposition by reaction of this oxidized copper and sulfate-bearing ore fluid with iron-rich brines of magmatic and non-magmatic origins. Their dissolved ferrous iron together with ferrous iron in chlorite and in pre-ore pyrite in the host rocks act as the essential reductant for magmatic sulfate to precipitate Cu sulfides, whereas oxidation of iron causes large-scale precipitation of hematite. Magmatic heat was essential to enable convective mixing of fluids with variable salinity, but the contribution of magmatic brine was not a main driver for brecciation at Prominent Hill. Most relevant for exploration, high-grade Cu-Au mineralization at this deposit was formed by redox reactions and mixing among fluids along with replacement of pre-ore pyrite by Cu sulfides plus acid neutralization during host rock alteration. Precipitation of high-grade Cu ores therefore occurred at the transition between hematite + quartz altered to hematite + aluminosilicate ± siderite altered rocks, i.e. the location with the strongest chemical gradient where the ore fluid became reduced and neutralized. These processes resulted in development of the distinct shell of high-grade Cu sulfide mineralization wrapping around the upward-convex shaped hematite + quartz core which is rich in gold. A distinct similarity between IOCG and sediment-hosted Cu deposits is that the highest grade Cu ores occur where the ore fluid migrated from oxidized into more reduced rocks, thereby defining a distinct first-order redox boundary.

References

Agangi, A., Kamenetsky, V.S., and McPhie, J., 2012, Evolution and emplacement of high fluorine rhyolites in the Mesoproterozoic Gawler silicic large igneous province, South Australia: Precambrian Research, v. 208, p. 124–144.

Allan, M.M., Yardley, B.W.D., Forbes, L.J., Shmulovich, K.I., Banks, D.A., and Shepherd, T.J., 2005, Validation of LA-ICP-MS fluid inclusion analysis with synthetic fluid inclusions: American Mineralogist, v. 90, p. 1767–1775.

Allen, M., Anderson, I., Benavides, J., Betts, P.G., Bull, S., Creaser, R.A., Davidson, G.D., Freeman, H., Holcombe, R., Meffre, S., Murphy, F., Schlegel, T.U., Tomkinson, M., Williams, P.J., and the OZ Minerals Prominent Hill Geology Team, 2016, New geological and geochronological constrains on the origin of the Prominent Hill hematitic IOCG deposit, Gawler craton, South Australia: Abstract for the Australian Earth science convention: Uncover Earths past to discover our future, June 26–30 2016, Adelaide, p. 1.

Ambrose, G.J., and Flint, R.B., 1981, Billa Kalina, South Australia, Explanatory Notes 250 000: Geological Survey of South Australia, Geological Series, Sheet SH/53–7.

Armit, R.J., Betts, P.G., Schaefer, B.F., Pankhurst, M.J., and Giles, D., 2014, Provenance of the early Mesoproterozoic Radium Creek Group in the northern Mount Painter inlier: Correlating isotopic signatures to inform tectonic reconstructions: Precambrian Research, v. 243, p. 63–87.

Audétat, A., Günther, D., and Heinrich, C.A., 1998, Formation of a magmatic-hydrothermal ore deposit; insights with LA-ICP-MS analysis of fluid inclusions: Science, v. 279, p. 2091–2094.

Audétat, A., Pettke, T., Heinrich, C.A., and Bodnar, R.J., 2008, The composition of magmatic-hydrothermal fluids in barren and mineralized intrusions: Economic Geology, v. 103, p. 877–908.

Baker, T., Bertelli, M., Fisher, L., Fu, B., Hodgson, W., Kendrick, M., Mark, G., Mustard, R., Ryan, C., and Williams, P.J., 2006, Salt and copper in iron oxide-copper-gold systems, Cloncurry district, Australia: Geochimica et Cosmochimica Acta, v. 70, p. A30.

Baker, T., Mustard, R., Fu, B., Williams, P.J., Dong, G.Y., Fisher, L., Mark, G., and Ryan, C. G., 2008, Mixed messages in iron oxide-copper-gold systems of the Cloncurry district, Australia: insights from PIXE analysis of halogens and copper in fluid inclusions: Mineralium Deposita, v. 43, p. 599–608.

Barton, M.D., 2014, 13.20 - Iron Oxide(–Cu–Au–REE–P–Ag–U–Co) Systems, in Holland, H.D., and Turekian, K.K., (eds.), Treatise on Geochemistry (Second Edition): Oxford, Elsevier, p. 515–541.

Barton, M.D., and Johnson, D.A., 1996, Evaporitic-source model for igneous-related Fe oxide-(REE-Cu-Au-U) mineralization: Geology, v. 24, p. 259–262.

Bastrakov, E.N., Skirrow, R.G., and Davidson, G.J., 2007, Fluid evolution and origins of iron oxide-Cu-Au prospects in the Olympic Dam district, Gawler craton, South Australia: Economic Geology, v. 102, p. 1415–1440.

Bastrakov, E.N., Jaireth, S., and Mernagh, T.P., 2010, Solubility of uranium in hydrothermal fluids at 25°–300°C: Implications for the formation of uranium deposits: Record 2010/029. Geoscience Australia, Canberra.

Belperio, A.P., 2002, The Prominent Hill copper-gold discovery; exploration strategies for world-class iron-oxide Cu-Au deposits: Abstracts Geological Society of Australia, v. 67, p. 257.

Belperio, A.P., and Freeman, H., 2004, Common geological characteristics of Prominent Hill and Olympic Dam; implications for iron oxide copper-gold exploration models: The AusIMM Bulletin, v. 1990, p. 67-70, 72–75.

Belperio, A., Flint, R., and Freeman, H., 2007, Prominent Hill: A hematite-dominated, iron oxide copper-gold system: Economic Geology, v. 102, p. 1499–1510.

Benavides, J., Kyser, T.K., Clark, A.H., Oates, C.J., Zamora, R., Tarnovschi, R., and Castillo, B., 2007, The Mantoverde iron oxide-copper-gold district, III region, Chile; the role of regionally derived, non-magmatic fluids in chalcopyrite mineralization: Economic Geology, v. 102, p. 415–440.

Bernard, A., Escobar, C.D., Mazot, A., Gutiérrez, R. E., 2004, The acid volcanic lake of Santa Ana volcano, El Salvador, in Rose, W.I., Bommer, J.J., López, D.L., Carr, M.J., and Major, J.J., (eds.), Natural hazards in El Salvador: Boulder, Colorado, Geological Society of America Special Paper 375, p. 121–133.

Betts, P.G., Valenta, R.K., and Finlay, J., 2003, Evolution of the Mount Woods inlier, northern Gawler craton, Southern Australia: an integrated structural and aeromagnetic analysis: Tectonophysics, v. 366, p. 83–111.

Betts, P.G., Giles, D., Mark, G., Lister, G.S., Goleby, B.R., and Aillères, L., 2006, Synthesis of the Proterozoic evolution of the Mt Isa inlier: Australian Journal of Earth Sciences, v. 53, p. 187–211.

Bodnar, R.J., and Bethke, P.M., 1984, Systematics of stretching of fluid inclusions. 1. Fluorite and sphalerite at 1 atmosphere confining pressure: Economic Geology, v. 79, p. 141–161.

Bodnar, R.J., and Vityk, M.O., 1994, Interpretation of microthermometric data for H_2O-NaCl fluid inclusions, in De Vivo, B., and Frezzotti, M.L., (eds.), Fluid Inclusions in Minerals, Methods and Applications, Blacksburg, VA, Virginia Tech, p. 117–130.

Böhlke, J.K., and Irwin, J.J., 1992, Laser microprobe analyses of Cl, Br, I and K in fluid inclusions - Implications for sources of salinity in some ancient hydrothermal fluids: Geochimica et Cosmochimica Acta, v. 56, p. 203–225.

Bottomley, D.J., Clark, I.D., Battye, N., and Kotzer, T., 2005, Geochemical and isotopic evidence for a genetic link between Canadian Shield brines, dolomitization in the Western Canada Sedimentary Basin, and Devonian calcium-chloridic seawater: Canadian Journal of Earth Sciences, v. 42, p. 2059–2071.

Boullier, A.M., Firdaous, K., and Robert, F., 1998, On the significance of aqueous fluid inclusions in gold-bearing quartz vein deposits from the southeastern Abitibi subprovince (Quebec, Canada): Economic Geology, v. 93, p. 216–223.

Bowden, B., Fraser, G., Davidson G.J., Meffre, S., Skirrow, R., Bull, S., Thompson, J., 2017, Age constraints on the hydrothermal history of the Prominent Hill iron oxide copper-gold deposit, South Australia: Mineralium Deposita, v. 52, p. 863-881.

Brown, A.C., 2014, 13.10 - Low-temperature sediment-hosted copper deposits, in Holland, H.D., and Turekian, K.K., (eds.): Treatise on Geochemistry (Second Edition): Oxford, Elsevier, p. 251–271.

Bull, S., Meffre, S., Allen, M., Freeman, H., Tomkinson, M., and Williams, P.J., 2015, Volcanosedimentary and chronostratigraphic architecture of the host rock succession at Prominent Hill, South Australia: Abstracts to the SEG 2015 conference: World Class Ore Deposits: Discovery to Recovery, Hobart, TAS, Australia, Society of Economic Geologists, p. 1.

Carpenter, A.B., Trout, M., and Pickett E.E., 1974, Preliminary report on the origin and chemical evolution of lead- and zinc-rich oil field brines in the central Mississippi: Economic Geology, v. 69, p. 1196-1206.

Carter, D., Belperio, T., and Freeman, H., 2003, The discovery of the Prominent Hill copper-gold deposit, South Australia: NewGenGold - Case histories of discovery: Perth, Lothean Media.

Chen, H.Y., 2010, Mesoproterozoic IOCG mineralisation in the Central Andes: An updated review, in Porter, T. M., (ed.), Hydrothermal iron oxide copper-gold & related deposits: A global perspective - Advantages in understanding of IOCG deposits, v. 3: Adelaide, PGC Publishing, p. 259–272.

Chen, H.Y., 2013, External sulphur in IOCG mineralization: Implications on definition and classification of the IOCG clan: Ore Geology Reviews, v. 51, p. 74–78.

Chiaradia, M., Banks, D., Cliff, R., Marschik, R., and de Haller, A., 2006, Origin of fluids in iron oxide-copper-gold deposits: constraints from delta Cl-37, Sr-87/Sr-86 and Cl/Br: Mineralium Deposita, v. 41, p. 565–573.

Christenson, B.W., and Wood, C.P., 1993, Evolution of a vent-hosted hydrothermal system beneath Ruapehu crater lake, New Zealand: Bulletin of Volcanology, v. 53, p. 547–565.

Cline, J.S., and Vanko, D.A., 1995, Magmatically generated saline brines related to molybdenum at Questa, New Mexico, USA, in Thompson, J. H. F., (ed.), Magmas, fluids, and ore deposits, 23, Mineralogical Association of Canada Short Course Notes, p. 153–174.

Creaser, R.A., 1995, Neodymium isotopic constraints for the origin of Mesoproteroroic felsic magmatism, Gawler craton, South Australia: Canadian Journal of Earth Sciences, v. 32, p. 460–471.

Creaser, R.A., 1996, Petrogenesis of a Mesoproterozoic quartz latite-granitoid suite from the Roxby Downs area, South Australia: Precambrian Research, v. 79, p. 371–394.

Creaser, R.A., and White, A.J.R., 1991, Yardea Dacite–large-volume, high temperature felsic volcanism from the Middle Proterozoic of South Australia: Geology, v. 19, p. 48–51.

Davidson, G.J., Paterson, H., Meffre, S., and Berry, R.F., 2007, Characteristics and origin of the Oak Dam East breccia-hosted, iron oxide Cu-U-(Au) deposit: Olympic Dam region, Gawler craton, South Australia: Economic Geology, v. 102, p. 1471–1498.

de Haller, A., and Fontboté, L., 2009, The Raul-Condestable iron oxide-copper-gold deposit, central coast of Peru: Ore and related hydrothermal alteration, sulfur isotopes, and thermodynamic constraints: Economic Geology, v. 104, p. 365–384.

Dilles, J.H., Einaudi, M.T., Proffett, J.M., and Barton, M.D., 2000, Overview of the Yerington porphyry copper district. Magmatic to nonmagmatic sources of hydrothermal fluids their flow paths and alteration effects on rocks and Cu-Mo-Fe-Au ores: Society of Economic Geologists Guidebook Series, v. 32, p. 55–66.

Dolejs, D., and Wagner, T., 2008, Thermodynamic modeling of non-ideal mineral-fluid equilibria in the system Si-Al-Fe-Mg-Ca-Na-K-H-O-Cl at elevated temperatures and pressures: Implications for hydrothermal mass transfer in granitic rocks: Geochimica et Cosmochimica Acta, v. 72, p. 526–553.

Dreher, A.M., Xavier, R.P., Taylor, B.E., and Martini, S. L., 2008, New geologic, fluid inclusion and stable isotope studies on the controversial Igarape Bahia Cu-Au deposit, Carajás Province, Brazil: Mineralium Deposita, v. 43, p. 161–184.

Ehrig, K., McPhie, J., and Kamenetsky, V., 2012, Geology and mineralogical zonation of the Olympic Dam iron oxide Cu-U-Au-Ag deposit, South Australia, in Hedenquist, J. W., Harris, M., and Camus, F., (eds.), Geology and genesis of major copper deposits and districts of the world: A tribute to Richard H. Sillitoe: Economic Geology, Special Publication 16, p. 237–267.

Fanning, C.M., Flint, R.B., Parker, A.J., Ludwig, K.R., and Blissett, A.H., 1988, Refined Proterozoic evolution of the Gawler craton, South Australia, through U-Pb zircon geochronology: Precambrian Research v. 40/41, p. 363-386.

Fanning, C.M., 1997, Geochronological synthesis of southern Australia. Part 2. The Gawler craton: South Australia Primary Industries and Resources Open File Envelope 8918.

Fanning, C.M., Reid, A.J., and Teale, G.S., 2007, A geochronological framework for the Gawler craton, South Australia: South Australia Geologial Survey Bulletin 55, 258 p.

Fisher, L.A., and Kendrick, M.A., 2008, Metamorphic fluid origins in the Osborne Fe oxide-Cu-Au deposit, Australia: evidence from noble gases and halogens: Mineralium Deposita, v. 43, p. 483–497.

Flint, R.B., and Benbow, M.C., 1977, Geology of the Mount Woods inlier, South Australia Department of Mines, Report Book 77/134, 50 p.

Flint, R.B., Blissett, A.H., Conor, C.H.H., Cowley, W.M., Cross, K.C., Creaser, R.A., Daly, S.J., Krieg, G.W., Major, R.B., Teale, G.S., and Parker, A.J., 1993, Mesoproterozoic: Adelaide, Geological Survey of South Australia Bulletin 54, p. 107–169.

Forbes, C.J., Giles, D., Hand, M., Betts, P.G., Suzuki, K., Chalmers, N., and Dutch, R., 2011, Using P-T paths to interpret the tectonothermal setting of prograde metamorphism: An example from the northeastern Gawler craton, South Australia: Precambrian Research, v. 185, p. 65–85.

Forbes, C.J., Giles, D., Jourdan, F., Sato, K., Omori, S., and Bunch, M., 2012, Cooling and exhumation history of the northeastern Gawler craton, South Australia: Precambrian Research, v. 200, p. 209–238.

Frape, S.K., and Fritz, P., 1987, Geochemical trends for groundwaters from the Canadian Shield: Geological Association of Canada - Special Paper, v. 33, p. 19–38.

Frape, S.K., Fritz, P., and McNutt, R.H., 1984, Water rock interaction and chemistry of groundwaters from the Canadian Shield: Geochimica et Cosmochimica Acta, v. 48, p. 1617–1627.

Freeman, H., and Tomkinson, M., 2010, Geological setting of iron oxide related mineralisation in the southern Mount Woods domain, South Australia, in Porter, T.M., (ed.), Hydrothermal iron oxide copper-gold & related deposits: A global perspective - Advantages in understanding of IOCG deposits, v. 3: Adelaide, PGC Publishing, p. 171–190.

Fusswinkel, T., Wagner, T., Wälle, M., Wenzel, T., Heinrich, C.A., and Markl, G., 2013, Fluid mixing forms basement-hosted Pb-Zn deposits: Insight from metal and halogen geochemistry of individual fluid inclusions: Geology, v. 41, p. 679–682.

Fusswinkel, T., Wagner, T., Wenzel, T., Wälle, M. Lorenz, J., 2014, Red bed and basement sourced fluids recorded in hydrothermal Mn-Fe-As veins, Seilauf (Germany): A LA-ICPMS fluid inclusion study: Chemical Geology, v. 363, p. 22–39.

Giles, C.W., 1988, Petrogenesis of the Proterozoic Gawler Range Volcanics, South Australia: Precambrian Research, v. 40, p. 407–427.

Giles, D., Betts, P. G., Aillères, L., Hulscher, B., Hough, M., and Lister, G.S., 2006, Evolution of the Isan orogeny at the southeastern margin of the Mt Isa inlier: Australian Journal of Earth Sciences, v. 53, p. 91–108.

Goldstein, R.H., and Reynolds, T.J., 1994, Systematics of fluid inclusions in diagenetic minerals: SEPM Short Course Notes, v. 31, 213 p.

Gow, P.A., Wall, V.J., Oliver, N.H.S., and Valenta, R.K., 1994, Proterozoic iron oxide (Cu-U-Au-REE) deposits: Further evidence of hydrothermal origins: Geology, v. 22, p. 633–636.

Günther, D., Audetat, A., Frischknecht, R., and Heinrich, C.A., 1998, Quantitative analysis of major, minor and trace elements in fluid inclusions using laser ablation–inductively coupled plasma mass spectrometry: Journal of Analytical Atomic Spectrometry, v. 13, p. 263–270.

Guillong, M., Meier, D.L., Allan, M.M., Heinrich, C.A., and Yardley, B.W.D., 2008, Appendix A6; SILLS; a MATLAB-based program for the reduction of laser ablation ICP-MS data of homogeneous materials and inclusions: Mineralogical Association of Canada Short Course Series, v. 40, p. 328–333.

Hanor, J.S., 1994, Origin of saline fluids in sedimentary basins, Geological Society Special Publication, v. 78, p. 151–174.

Harris, T.M., Murphy, F.C., Funk, C.W., and Betts, P.G., 2013, Mt Woods 2D seismic reflection survey, Gawler craton, South Australia: An intergrated minerals exploration case study, 23rd international geophysical conference and exhibition, ASEG-PESA 2013, The eureka moment: Melbourne, Australia, CSIRO Publishing, p. 1–4.

Hayba D.O., and Ingebritsen S.E., 1997, Multiphase groundwater flow near cooling plutons; Journal of Geophysical Research, v. 102, p. 12235–12252.

Haynes, D.W., Cross, K.C., Bills, R.T., and Reed, M.H., 1995, Olympic Dam ore genesis: A fluid-mixing model: Economic Geology, v. 90, p. 281–307.

Haynes, F.M., 1985, Determination of fluid inclusion compositions by sequential freezing: Economic Geology, v. 80, p. 1436–1439.

Haynes, F.M., and Kesler, S.E., 1988, Composition and sources of mineralizing fluids from Chimney and Manto limestone-replacement ores in Mexico: Economic geology, v., 83, p. 1985–1992.

Hayward, N., and Skirrow, R.G., 2010, Geodynamic setting and controls on iron oxide Cu-Au (U) ore in the Gawler craton, South Australia, in Porter, T.M., (ed.), Hydrothermal iron oxide copper-gold & related deposits: A global perspective, v. 3: Adelaide, PGC Publishing, p. 119–146.

Heinrich, C.A., and Candela, P.A., 2014, 13.1 - Fluids and Ore Formation in the Earth's Crust, in Turekian, K. H., and Holland, H. D., (eds.), Treatise on Geochemistry (Second Edition): Oxford, Elsevier, p. 1–28.

Heinrich, C.A., Andrew, A.S., Wilkins, R.W.T., and Patterson, D.J., 1989, A fluid inclusion and stable isotope study of synmetamorphic copper ore formation at Mount Isa, Australia: Economic Geology, v. 84, p. 529–550.

Heinrich, C.A., Bain, J.H.C., Mernagh, T.P., Wyborn, L.A.I., Andrew, A.S., and Waring, C. L., 1995, Fluid and mass transfer during metabasalt alteration and copper mineralization at Mount Isa, Australia: Economic Geology, v. 90, p. 705–730.

Heinrich, C.A., Pettke, T., Halter, W.E., Aigner-Torres, M., Audétat, A., Güther, D., Hattendorf, B., Bleiner, D., Guillong, M., and Horn, I., 2003, Quantitative multi-element analysis of minerals, fluid and melt inclusions by laser-ablation inductively-coupled-plasma mass-spectrometry: Geochimica et Cosmochimica Acta, v. 67, p. 3473–3497.

Henley, R.W., 2015, Hyperacidic volcanic lakes, metal sinks and magmatic gas expansion in arc volcanoes, in Rouwet, D., Christenson B., Tassi, F., and Vandemeulebrouck, J., (eds.), Volcanic lakes, Advances in Volcanology: Springer, p. 155–178.

Hennings, S.K., Wagner, T., Heinrich C.A., and Ulmer P., 2017, Fluid evolution of the Monte Mattoni mafic complex, Adamello batholith, northern Italy: constraints from LA-ICPMS analysis

of fluid inclusions and thermodynamic modelling: Journal of Petrology, doi: 10.1093/petrology/egx068

Hemley, J.J., Montoya, J.W., Marinenko, J.W., and Luce, R.W., 1980, Equilibria in the system Al_2O_3-SiO_2-H_2O and some general implications for alteration-mineralization processes: Economic Geology, v. 75, p. 210–228.

Hitzman, M.W., Oreskes, N., and Einaudi, M.T., 1992, Geological characteristics and tectonic setting of Proterozoic iron oxide (Cu-U-Au-REE) deposits: Precambrian Research, v. 58, p. 241–287.

Hitzman, M.W., Selley, D., Bull, S., 2010. Formation of sedimentary rock-hosted stratiform copper deposits trough Earth history: Economic Geology, v. 105, p- 627–639.

Jambon, A., Deruelle, B., Dreibus, G., and Pineau, F., 1995, Chlorine and bromine abundance in MORB: The contrasting behaviour of the Mid-Atlantic Ridge and East Pacific Rise and implications for chlorine geodynamic cycle: Chemical Geology, v. 126, p. 101–117.

Kharaka, Y.K., Maest, A.S., Carothers, W.W., Law, L.M., Lamothe, P.J., and Fries, T.L., 1987, Geochemistry of metal-rich brines from central Mississippi Salt Dome basin, USA: Applied Geochemistry, v. 2, p. 543–651.

Kharaka, Y.K., and Hanor, J.S., 2003, 5.16 – Deep fluids in the continents: I. Sedimentary basins, Holland, H.D., and Turekian, K.K., (eds.), Treatise on Geochemistry, Oxford, Elsevier v. 5-9, p. 1–48.

Kendrick, M.A., Mark, G., and Phillips, D., 2007, Mid-crustal fluid mixing in a Proterozoic Fe oxide-Cu-Au deposit, Ernest Henry, Australia: Evidence from Ar, Kr, Xe, Cl, Br, and I: Earth and Planetary Science Letters, v. 256, p. 328–343.

Kouzmanov, K., and Pokrovski, G.S., 2012, Hydrothermal controls on metal distribution in porphyry Cu (-Mo-Au) systems: Society of Economic Geologists Special Publication 16, p. 573–618.

Lecumberri-Sanchez, P., Steele-MacInnis, M., Weis, P., Driesner, T., and Bodnar, R.J., 2015, Salt precipitation in magmatic-hydrothermal systems associated with upper crustal plutons: Geology, v. 43, p. 1063–1066.

Lodemann, M., Fritz, P., Wolf, M., Ivanovich, M., Hansen, B.T., and Nolte, E., 1998, On the origin of saline fluids in the KTP (Continental Deep Drilling Project of Germany): Applied Geochemistry, v. 13, p. 653–671.

Longerich, H.P., Jackson, S.E., and Gunther, D., 1996, Laser ablation inductively coupled plasma mass spectrometric transient signal data acquisition and analyte concentration calculation: Journal of Analytical Atomic Spectrometry, v. 11, p. 899–904.

Mark, G., Oliver, N.H.S., and Williams, P.J., 2006, Mineralogical and chemical evolution of the Ernest Henry Fe oxide-Cu-Au ore system, Cloncurry district, northwest Queensland, Australia: Mineralium Deposita, v. 40, p. 769–801.

Marschik, R., and Fontboté, L., 2001, The Candelaria-Punta del Cobre iron oxide Cu-Au(-Zn-Ag) deposits, Chile: Economic Geology, v. 96, p. 1799–1826.

McCaffrey, M.A., Lazar, B., and Holland, H.D., 1987, The evaporation path of seawater and the coprecipitation of Br^- and K^+ with halite: Journal of Sedimentary Petrology, v. 57, p. 928–937.

McPhie, J., Kamenetsky, V., Allen, S., Ehrig, K., Agangi, A., and Bath, A., 2011a, The fluorine link between a supergiant ore deposit and a silicic large igneous province: Geology, v. 39, p. 1003–1006.

McPhie, J., Kamenetsky, V.S., Chambefort, I., Ehrig, K., and Green, N., 2011b, Origin of the supergiant Olympic Dam Cu-U-Au-Ag deposit, South Australia: Was a sedimentary basin involved?: Geology, v. 39, p. 795–798.

Menyailov, I.A., and Nikitina, L.P., 1980, Chemistry and metal contents of magmatic gases: the Tolbachik volcanoes case (Kamchatka): Bulletin of Volcanology, v. 43, p. 197–205.

Migdisov, A.A., Bychkov, A., Williams-Jones, A.E., and van Hinsberg, V.J., 2014, A predictive model for the transport of copper by HCl-bearing water vapour in ore-forming magmatic-hydrothermal systems: Implications for copper porphyry ore formation: Geochimica et Cosmochimica Acta, v. 129, p. 33–53.

Nahnybida, R., Gleeson, S.A., Rusk, B.G., Wassenaar, L.I., 2009, Cr/Br ratios and stable chlorine isotope analysis of magmatic-hydrothermal fluid inclusions from Butte, Montana and Bingham Canyon, Utah: Mineralium Deposita, v. 44, p. 837–848.

Oakes, C.S., Bodnar, R.J., and Simonson, J.M., 1990, The system $NaCl-CaCl_2-H_2O$. 1. The ice liquidus at 1 atm pressure: Geochimica et Cosmochimica Acta, v. 54, p. 603–610.

Oliver, N.H.S., 1995, Hydrothermal history of the Mary-Kathleen Fold Belt, Mount Isa block, Queensland: Australian Journal of Earth Sciences, v. 42, p. 267–279.

Oliver, N.H.S., Cleverley, J.S., Mark, G., Pollard, P.J., Fu, B., Marshall, L.J., Rubenach, M.J., Williams, P.J., and Baker, T., 2004, Modeling the role of sodic alteration in the genesis of iron oxide-copper-gold deposits, Eastern Mount Isa block, Australia: Economic Geology, v. 99, p. 1145–1176.

Oreskes, N., and Einaudi, M.T., 1990, Origin of rare-earth element-enriched hematite breccias at the Olympic-Dam Cu-U-Au-Ag deposit, Roxby Downs, South Australia: Economic Geology, v. 85, p. 1–28.

Oreskes, N., and Einaudi, M.T., 1992, Origin of hydrothermal fluids at Olympic Dam; preliminary results from fluid inclusions and stable isotopes: Economic Geology v. 87, p. 64–90.

Page, R.W., Conor, C.H.H., Stevens, B.P.J., Gibson, G.M., Preiss, W.V., and Southgate, P.N., 2005, Correlation of Olary and Broken Hill domains, Curnamona Province: Possible relationship to Mount Isa and other north Australian Pb-Zn-Ag-bearing successions: Economic Geology, v. 100, p. 663–676.

Pettke, T., Oberli, F., Audétat, A., Guillong, M., Simon, A.C., Hanley, J.J., and Klemm, L.M., 2012, Recent developments in element concentration and isotope ratio analysis of individual fluid inclusions by laser ablation single and multiple collector ICP-MS: Ore Geology Reviews, v. 44, p. 10–38.

Pollard, P.J., 2000, Evidence of a magmatic fluid and metal source for Fe-oxide Cu-Au mineralization, in Porter, T.M., (ed.), Hydrothermal iron oxide copper-gold & related deposits - a global perspective, v. 1: Adelaide, PGC Publishing, p. 27–41.

Pollard, P.J., 2006, An intrusion-related origin for Cu-Au mineralization in iron oxide-copper-gold (IOGG) provinces: Mineralium Deposita, v. 41, p. 179–187.

Redmond, P.B., Einaudi, M.T., Inan, E.E., Landtwing, M.R., and Heinrich, C.A., 2004, Copper deposition by fluid cooling in intrusion-centered systems: New insights from the Bingham porphyry ore deposit, Utah: Geology, v.32, p. 217–220.

Reed, M.H., 1997, Hydrothermal alteration and its relationship to ore fluid composition, in Barnes, H. L., (ed.), Geochemistry of hydrothermal ore deposits, third Edition, John Wiley & Sons, p. 303–365.

Roedder, E., 1984, Fluid inclusions: Reviews in Mineralogy, v. 12.

Rowe, G.L., Ohsawa, S., Takano, B., Brantley, S., Fernandez, J. F., and Barguero, J., 1992, Using crater lake chemistry to predict volcanic activity at Poás volcano, Costa Rica: Bulletin of Volcanology, v. 54, p. 494–503.

Samson, I.M., Williams-Jones, A.E., Ault, K. M., Gagnon, J. E., and Fryer, B. J., 2008, Source of fluids forming distal Zn-Pb-Ag skarns: Evidence from laser ablation-inductively coupled plasma-mass spectrometry analysis of fluid inclusions from El Mochito, Honduras: Geology, v. 36, p. 947–950.

Schlegel, T.U., 2010, Ore-fluid history of the Prominent Hill iron oxide-copper-gold deposit, South Australia: A reconnaissance fluid inclusion study: Unpublished MSc thesis, Swiss Federal Institute of Technology, ETH Zurich, 66 p.

Schlegel, T.U., and Heinrich, C.A., 2015, Alteration and lithology control Cu mineralization at Prominent Hill iron oxide-copper-gold deposit, Gawler craton, South Australia: Economic Geology, v. 110, p. 1953–1994.

Schlegel, T.U., Wälle, M., Steele-MacInnis, M., and Heinrich, C.A., 2012, Accurate and precise quantification of major and trace element compositions of calcic-sodic fluid inclusions by combined microthermometry and LA-ICP-MS analysis: Chemical Geology, v. 334, p. 144–153.

Schlegel, T.U., Wagner, T., Heinrich C.A., and Boyce, A.J., 2017, Magmatic-hydrothermal sulfur source for Prominent Hill and other iron oxide-copper-gold mineralisations in the Olympic IOCG province, South Australia: Ore Geology Reviews, v. 89, p. 1058–1090.

Seedorff, E., Dilles, J., Proffett, J., Einaudi, M., Zurcher, L., Stavast, W., Johnson, D., and Barton, M.D., 2005, Porphyry deposits: characteristics and origin of hypogene features: Economic Geology 100th Anniversary Volume, p. 251–298.

Seo, J.H., Guillong, M., Aerts, M., Zajacz, Z., and Heinrich, C.A., 2011, Microanalysis of S, Cl, and Br in fluid inclusions by LA-ICP-MS: Chemical Geology, v. 284, p. 35–44.

Sillitoe, R.H., 2003, Iron oxide-copper-gold deposits: an Andean view: Mineralium Deposita, v. 38, p. 787–812.

Sillitoe, R.H., 2010, Porphyry copper systems: Economic Geology, v. 105, p. 3–41.

Singer, D.A., Berger, V.I., Moring, B.C., 2008, Porphyry copper deposits of the world: database and tonnage models, 2008: Open-file report 2008-1155, U.S. Geological Survey, Reston Virgina.

Skirrow, R.G., and Walshe, J.L., 2002, Reduced and oxidized Au-Cu-Bi iron oxide deposits of the Tennant Creek inlier, Australia: An integrated geologic and chemical model: Economic Geology, v. 97, p. 1167–1202.

Skirrow, R.G., Bastrakov, E., Davidson, G.J., Raymond, O.L., and Heithersay, P., 2002, The geological framework, distribution and controls of Fe-oxide Cu-Au mineralisation in the Gawler craton, South Australia; Part II, Alteration and mineralisation, in Porter, T. M., (ed.), Hydrothermal iron oxide copper-gold & related deposits - A global perspective, v. 2: Adelaide, PGC Publishing, p. 33–47.

Souza, L.H., and Vieira, E.A.P., 2000, Salobo 3 Alpha Deposit; geology and mineralization: Part I, in Porter, T.M., (ed.), Hydrothermal iron oxide copper-gold & related deposits - A global perspective, v. 1: Adelaide, PGC Publishing, p. 213–224.

Steele-MacInnis, M., Bodnar, R.J., and Naden, J., 2011, Numerical model to determine the composition of H_2O-NaCl-$CaCl_2$ fluid inclusions based on microthermometric and microanalytical data: Geochimica et Cosmochimica Acta, v. 75, p. 21–40.

Steele-MacInnis, M., Ridley, J., Lecumberri-Sanchez, P., Schlegel, T.U., and Heinrich, C.A., 2016, Application of low-temperature microthermometric data for interpreting multicomponent fluid inclusion compositions: Earth-Science Reviews, v. 159, p. 14–35.

Steuber, A.M., Walter, L.M., Huston, T.E., and Pushkar, R., 1993, Formation waters from the Mississippi-Pennsylvanian reservoirs, Illinois basin, USA: Chemical and isotopical constraints on evolution and migration: Geochemica and Cosmochemica Acta, v. 57, p. 763–784.

Stoffell, B., Appold, M.S., Wilkinson, J.J., McClean, N.A., and Jeffries, T.E., 2008, Geochemistry and evolution of Mississippi Valley-type mineralizing brines from the Tri-State and Northern Arkansas districts determined by LA-ICP-MS microanalysis of fluid inclusions: Economic Geology, v. 103, p. 1411–1435.

Sriwana, T., van Bergen, M.J., Varekamp, J.C., Sumarti, S., Takano, B., van Os, G.J.H., and Leng, M.J., 2000, Geochemistry of the acid Kawah Putih lake, Patuha volcano, West Java, Indonesia: Journal of Volcanology and Geothermal Research, v. 97, p. 77–104.

Symonds, R.B., Rose, W.I., Gerlach, T.M., Briggs, P.H., and Harmon, R.S., 1990, Evaluation of gases, condensates, and SO_2 emissions from Augustine volcano, Alaska: the degasing of a Cl-rich volcanic system: Bulletin of Volcanology, v. 52, p. 355–374.

Tagirov, B.R., and Schott, J., 2001, Aluminum speciation in crustal fluids revisited: Geochimica et Cosmochimica Acta, v. 65, p. 3965–3992.

Taran, Y.A., Hedenquist, J.W., Korzhinsky, M.A., Tkachenko, S.I., and Shmulovich, K.I., 1995, Geochemistry of magmatic gases form Kudrayavy volcano, Iturup, Kuril Islands: Geochimica et Cosmochimica Acta, v. 59, p. 1749–1761.

Taran, Y.A., Bernard, A., Gavilanes, J.-C., Lunezheva, E., Cortés, A., and Armienta, M.A., 2001, Chemistry and mineralogy of high-temperature gas discharges from Colima volcano, Mexico. Implications for magmatic gas-athmosphere interaction; Journal of Volcanology and Geothermal Research, v. 108, p. 245–264.

Turner, W., Richards, J., Nesbitt, B., Muehlenbachs, K., and Biczok, J., 2001, Proterozoic low-sulfidation epithermal Au-Ag mineralization in the Mallery Lake area, Nunavut, Canada: Mineralium Deposita, v. 36, p. 442–457.

Ulrich, M.R., and Bodnar, R.J., 1988, Systematics of stretching of fluid inclusions. 2. Barite at 1-atm confining pressure: Economic Geology, v. 83, p. 1037–1046.

Ulrich, T., Günther, D., and Heinrich, C.A., 2001, The evolution of a porphyry Cu-Au deposit, based on LA-ICP-MS analysis of fluid inclusions: Bajo de la Alumbrera, Argentina: Economic Geology, v. 96, p. 1743–1774.

van Hinsberg, V.V., Vigouroux, N., Palmer, S., Berlo, K., Mauri, G., Williams-Jones, A.E., Mckenzie, J., Williams-Jones, G., and Fischer, T., 2017, Element flux in the environment of passively degassing crater lake-hosting Kawah Ijen volcano, Indonesia, and implications for estimates of the global volcanic flux, in Ohba, T., Capaccioni, B. and Caudron, C. (eds.): Geochemistry and Geophysics of Active Volcanic Lakes. Geological Society, London, Special Publications, v. 437, p. 9–34.

Vanko, D.A., Bodnar, R.J., and Sterner, S.M., 1988, Synthetic fluid inclusions. 8. Vapor-saturated halite solubility in part of the system $NaCl-CaCl_2-H_2O$, with application to fluid inclusions from oceanic hydrothermal systems: Geochimica et Cosmochimica Acta, v. 52, p. 2451–2456.

Varekamp, J. C., 2015, The chemical composition and evolution of volcanic lakes, in Rouwet, D., Christenson B., Tassi, F., and Vandemeulebrouck, J., (eds.): Volcanic lakes, Advances in Volcanology: Springer, p. 93–123.

Wagner, T., Fusswinkel, T., Wälle, M., and Heinrich, C.A., 2016, Microanalysis of fluid inclusions in crustal hydrothermal systems using laser ablation methods: Elements, v. 12, p. 323–328.

Wälle, M., and Heinrich, C.A., 2014, Fluid inclusion measurements by laser ablation sector-field ICP-MS: Journal of Analytical Atomic Spectrometry, v. 29, p. 1052–1057.

Wilkinson, J.J., 2013, Sediment-hosted zinc-lead mineralization: Processes and perspectives, Treatise on Geochemistry (Second Edition): Oxford, Elsevier, p. 219–249.

Wilkinson, J.J., Boyce, A.J., Earls, G., and Fallick, A.E., 1999, Gold remobilization by low-temperature brines: Evidence from the Curraghinalt gold deposit, Northern Ireland: Economic Geology, v. 94, p. 289–296.

Williams-Jones, A.E., and Heinrich, C.A., 2005, 100th Anniversary Special Paper: Vapor transport of metals and the formation of magmatic-hydrothermal ore deposits: Economic Geology, v. 100, p. 1287–1312.

Williams-Jones, A.E., Samson, I.M., Ault, K.M., Gagnon, J.E., Fryer, B.J., 2010, The genesis of distal zinc skarns: Evidence from the Mochito deposit, Honduras: Economic Geology, v. 105, p. 1411–1440.

Williams, P.J., and Skirrow, R.G., 2000, Overview of iron oxide-copper-gold deposits in the Curnamona province and Cloncurry district (eastern Mount Isa Block), Australia, in Porter, T.M., (ed.), Hydrothermal iron oxide copper-gold & related deposits - a global perspective, v. 1: Adelaide, PGC Publishing, p. 105–122.

Williams, P.J., Dong, G. Y., Ryan, C.G., Pollard, P.J., Rotherham, J.F., Mernagh, T.P., and Chapman, L.H., 2001, Geochemistry of hypersaline fluid inclusions from the Starra (Fe oxide)-Au-Cu deposit, Cloncurry district, Queensland: Economic Geology v. 96, p. 875–883.

Williams, P.J., Barton, M.D., Johnson, D.A., Fontboté, L., de Haller, A., Mark, G., Oliver, N.H.S., and Marschik, R., 2005, Iron oxide copper-gold deposits: geology, space-time distribution, and possible modes of origin: Economic Geology 100th Anniversary Volume, p. 371–405.

Williams, P.J., Kendrick, M.A., and Xavier, R.P., 2010, Sources of ore fluid components in IOCG deposits, in Porter, T.M., (ed.), Hydrothermal iron oxide copper-gold & related deposits: A global perspective - Advantages in understanding of IOCG deposits, v. 3: Adelaide, PGC Publishing, p. 107–116.

Williams, P.J. Freeman H., Anderson, I., and Holcombe, R., 2017a, Prominent Hill copper-gold deposit, in Philips, N. (ed.): Australian ore deposits: Carlton Victoria, Monograph 32, The Australian Institute of Mining and Metallurgy, p. 611–614.

Williams, P.J., Benavides J., Sadikin P., OZ Minerals Prominent Hill Geology Team, 2017b; Metallogenic significance of altered volcanic rocks near the Prominent Hill IOCG deposit, South Australia: Proceedings of the 14th SGA Biennial Meeting, Quebéc, v. 3, p. 895–898.

Wilson, T.P., and Long, D.T., 1993, Geochemistry and isotope chemistry of Ca-Na-Cl brines in Silurian strata, Michigan basin, USA: Applied Geochemistry, v. 8, p. 507–524.

Xavier, R.P., Wiedenbeck, M., Trumbull, R.B., Dreher, A.M., Monteiro, L.V.S., Rhede, D., de Araujo, C.E.G., and Torresi, I., 2008, Tourmaline B-isotopes fingerprint marine evaporites as the source of high-salinity ore fluids in iron oxide copper-gold deposits, Carajas mineral province (Brazil): Geology, v. 36, p. 743–746.

Yanatieva, O.K., 1946, Solubility polytherms in the systems $CaCl_2$-$MgCl_2$-H_2O and $CaCl_2$-NaCl-H_2O: Russian Journal of General Chemistry, v. 19, p. 709–722.

Yudovskaya, M.A., Dister, V.V., Chaplygin, I.V., Mokhov, A.V., Trubkin, N.V., and Gorbacheva S.A., 2006, Gaseous transport and deposition of gold in magmatic fluid: evidence from the active Kudryavy volcano, Kurile Islands: Mineralium Deposita, v. 40, p. 828–848.

Zwart, E.W., and Touret, J.L.R., 1994, Melting behavior and composition of aqueous fluid inclusions in fluorite and calcite - Applications within the System H_2O-$CaCl_2$-NaCl: European Journal of Mineralogy, v. 6, p. 773–786.

Appendix

Fluid inclusion petrography and microthermometry

Ninety-six doubly-polished wafers of 200–350 μm thickness were prepared and examined in order to document consistent FIA. Detailed fluid inclusion petrography was carried out on quartz, fluorite, barite, calcite and dolomite bearing samples (Table 1). Inclusion petrography was performed using an Olympus BX-60 microscope equipped with transmitted and reflected light. Petrographic relationships were documented on high-resolution A3 printouts of photomicrographic mosaics, acquired using a combination of transmitted and reflected light.

Microthermometry was performed on 16 representative samples (Table 1) using a Linkham THMSG-600 heating-freezing stage, equipped with Linkham LNP and Cl94 controlling units attached to a Nikon E600 transmitted light microscope (Table A1). The microthermometry stage was calibrated with synthetic fluid inclusion standards containing CO_2 (triple point: –56.6°C), H_2O–NaCl (eutectic melting of ice and hydrohalite: –21.2°C), H_2O (ice melting: 0.0°C, homogenization: 374.1°C). Fluorite and barite are not considered as highly reliably host minerals in terms of volume preservation (Bodnar and Bethke, 1984; Ulrich and Bodnar, 1988), thus microthermometry was done with the greatest care to avoid any overstepping of the homogenization temperature. Low-temperature microthermometry of vapor-saturated fluid inclusions was performed as described in Schlegel et al. (2012), recording two individual final melting temperatures of ice, hydrohalite and the dissolution temperature of halite by careful cyclic heating and cooling (Table A2).

Table A1. Instrumental parameters of the LA-ICP-MS and microthermometry analytical systems.

LA-ICP-MS systems	
Laser type	ArF excimer laser (193nm) (Coherent, Germany) and homogenized beam path
Laser energy for mineral ablation	>30 J/cm^2
Laser pulse frequency	10Hz
Ablation diameter	variable from 5 to 100μm by adjusting a variable aperture
ICPMS systems	Elan 6100 DRC ICP quadrupole mass spectrometer (Perkin Elmer) Element XR, sector field mass spectrometer (ThermoFisher)
Carrier gas	He, 1.1 l/min
Auxiliary gas	H_2 5 ml/min for Elan 6100 DRC
Dwell time	10 ms, except for Ca, Br and Cu 20ms
External standards	NIST610, in-house scapolite for Cl and Br
Microthermometry System	
Heating-freezing stage	Linkham THMSG 600 heating–freezing stage
Controlling units	Linkham LNP and Cl 94
Optical microscope	Nikon Eclipse E600 Pol
Objective	50x
Calibration standard	Syn Flinc® fluid inclusion H_2O (0 °C and 374.1 °C), H_2O–CO_2 (–56.6 °C) H_2O–NaCl (–21.2 °C)

The absolute NaCl and $CaCl_2$ salinities were quantified from the temperatures of ice and hydrohalite melting, or ice melting and halite dissolution (Table A2), using the H_2O–NaCl–$CaCl_2$ phase relations of Steele-MacInnis et al. (2011). The salinities of inclusions interpreted with the H_2O–NaCl fluid model system were calculated using equations from Bodnar and Vityk (1994). Despite great care, it was not always possible to observe ice and hydrohalite melting in all inclusions of an assemblage. Average melting temperatures from fluid inclusions within the same FIA were used to calculate the salinity in this case. In order to avoid systematic errors in

the calculation of salinity caused by metastable hydrohalite melting, average salinities have been calculated from inclusions showing non-metastable melting behavior. Rarely, every fluid inclusion within an assemblage showed metastable hydrohalite melting, thus the average hydrohalite melting temperatures of all other FIA of the same fluid inclusion subtype in the same sample was used to calculate the salinity. This procedure minimized any systematic errors. Deviations from true salinities are likely to be small, because the hydrohalite and halite stability fields show a sharp increase near the cotectic line, implying that the salinity increase is relatively insensitive to temperature (Schlegel, 2010).

LA-ICP-MS analysis of fluid inclusion assemblages and element quantification transient signals

A beam homogenized 193 nm ArF Eximer laser ablation system (Günther et al., 1998; Heinrich et al., 2003) was coupled either to a ThermoFisher Element XR sector field mass spectrometer (LA-SF-ICP-MS; Wälle and Heinrich, 2014) or to an Elan 6100 DRC ICP quadrupole mass spectrometer (LA-Q-ICP-MS), both located at ETH Zürich. The laser pulse frequency was 10 Hz. All ablation pits were selected based on the size of the fluid inclusions by adjusting an aperture in the laser beam path (Günther et al., 1998). Helium with 0.5 vol.% of H_2 additive was used as carrier gas in the LA-Q-ICP-MS system and pure helium in the LA-SF-ICP-MS. Each ablation run was observed as a real-time signal in order to relate the signal to the ablated inclusion. Standard reference material SRM NIST 610 and the in-house scapolite standard SCA-17 (for Cl and Br) were used as external standards (Seo et al., 2011). All analytical parameters are summarized in Table A1. To account for instrumental drift, the standards were measured two times prior and after ablation in each chip or after a maximum of 26 ablated inclusions. The analyses were done with different multi-element menus for matrix and vein-hosted samples, depending on the FI host mineral.

We measured the isotopes ^{7}Li, ^{11}B, ^{23}Na, ^{24}Mg, ^{27}Al, ^{29}Si, ^{39}K, ^{44}Ca, ^{55}Mn, ^{57}Fe, ^{65}Cu, ^{133}Cs, ^{137}Ba, ^{208}Pb and ^{238}U in fluid inclusions with sizes between 15 and 50 μm (occasionally up to 80 μm) from hematite-aluminosilicates breccia matrix and in clast-replacement samples using the more sensitive LA-SF-ICP-MS system. Both ^{32}S and ^{75}As were initially included, but later dropped from the element menu, in order to improve the counting statistics (i.e. increasing dwell times) for elements that could be detected and quantified but had low concentrations. Analysis of the typically larger (> 25 μm) vein-hosted FIA was performed on the LA-Q-ICP-MS system. The fluid inclusions were analyzed for the isotopes ^{23}Na, ^{29}Si, ^{32}S, ^{39}K, ^{44}Ca, ^{55}Mn, ^{57}Fe, ^{65}Cu, ^{133}Cs, ^{208}Pb and ^{238}U. In both matrix and vein samples, some FIA analyses were done with a reduced element menu optimized for analysis of Br/Cl ratio that included only the isotopes ^{23}Na, ^{24}Mg, ^{35}Cl, ^{39}K, ^{65}Cu and ^{79}Br along with ^{29}Si, ^{44}Ca, or ^{137}Ba depending on the ablated host mineral.

In general, the FIA contain Na and commonly Ca (both measured by microthermometry), but lesser amounts (less than one-tenth of the Na) of K, Fe, Mg, Si, Li, B, S, Mn, Cu, Cs, Pb and U. This confirms the validity of the microthermometry interpretation in terms of the ternary H_2O–$NaCl$–$CaCl_2$ model system (Schlegel, 2010). The SILLS software was used for data reduction including spike elimination, time-integration of background-subtracted and host mineral corrected signals (Allan et al., 2005; Guillong et al., 2008). Only element signals showing a peak that would clearly follow the large Na peak of the FI were considered significant and quantified.

The concentrations of major and trace elements in Ca-bearing fluid inclusions were quantified using the microthermometrically calculated absolute Na concentrations as internal standard, which was then applied to individual LA-ICP-MS analyses. The use of absolute Na concentrations increases the accuracy of the element concentration data compared to quantification methods that use NaCl equivalent salinity (Schlegel et al., 2012). In some FIA, individual inclusions analyzed by LA-ICP-MS did not allow determination of their Na–Ca salinity, in which case the average Na content obtained from other fluid inclusions in the same FIA was used as internal standard. For assemblages in which none of the inclusions showed a quantifiable Ca content, the ice melting or halite dissolution was interpreted to determine the NaCl equivalent salinity. Sodium was then used as internal standard for quantification of elemental concentrations, with an empirical salt correction based on the LA-ICP-MS signals for

potassium (Heinrich et al., 2003). The reported $CaCl_2$ concentrations and Ca/Na ratios are therefore mostly based on the two microthermometric phase transitions, being more accurate than the determination of the Ca concentration by LA-ICP-MS (Schlegel et al., 2012).

All element concentrations are reported as ppm by weight (µg/g). Limits of detection (LOD) were determined for all elements in each inclusion, using the 3σ standard deviation of the background signals (Longerich et al., 1996; Heinrich et al., 2003; Pettke et al., 2012). The LOD values are reported as estimated averages from the best inclusions when all inclusions in an FIA are below the LOD. Average concentrations were computed from all measured values in each FIA, and uncertainties were calculated as standard deviations (± 1σ value). Additional information on the ablation of host minerals other than quartz are detailed in Schlegel (2010) and Schlegel et al. (2012).

Table A2. Microthermometry data of fluid inclusion assemblages from Prominent Hill IOCG deposit

ID	Sample	FI-type	FIA-No.	Host	Model	T ice	±	T HH	+-	T_h lh-l	+-	T_h lv-l	+-	n (tot)	n
Hematite-aluminosilicate breccia matrix															
88	238	LV10	2	Fl	A	−25.5	0.5	−19.1	3.5					7	7
85*	238	LV10S	1	Fl	A	−28.6	1.0	−23.6	2.1					20	20
87	238	LV2S	6	Fl	A	−19.9	1.5	−28.5	0.9					14	14
84*	238	LV2S	1	Fl	A	−20.3	2.1	−24.5	1.3					20	20
86	238	LV2S	5	Fl	A	−21.1	1.4	−25.8	0.9					19	19
82	238	LV2S	4a	Fl	A	−21.3	2.2	−26.6	1.4					8	8
83	238	LV2S	3b	Fl	A	−21.8	1.4	−27.5	0.5					7	7
81*	238	LV2S	2	Fl	A	−25.7	1.0	−4.4	1.0					11	10
131	238	LV2S	1	Fl	B	n.d.	n.d.					>194	n.d.	n.d.	n.d.
132	245	LV10	1	Fl	B	n.d.	n.d.					>135	n.d.	n.d.	n.d.
102	245	LV10S	8	Fl	A	−26.4	0.6	−13.6	0.9					8	8
99	245	LV10S	7	Fl	A	−24.0	1.0	−3.7	1.4					16	14
93	245	LV10S	3	Fl	A	−25.1	0.7	−5.5	0.9					9	9
96	245	LV10S	1	Fl	A	−26.1	0.8	−5.9	2.5					23	19
91	245	LV10S	2	Fl	A	−27.3	0.3	−4.4	1.0					16	1
95	245	LV10S	4	Fl	A	−27.6	0.5	−5.0	0.5					6	1
101	245	LV15	1	Fl	A	−23.0	0.8	−29.0	0.6					16	10
94	245	LV20S	1	Fl	B	−17.8	0.3							7	7
92*	245	LV2S	2	Fl	A	−24.9	0.4	−9.0	1.7					22	22
98	245	LV2S	3	Fl	A	−23.6	1.0	−3.6	1.5					18	17
90	245	LV2S	1	Fl	A	−26.5	0.4	−4.0	1.1					17	3
100	245	LVoS	1	Fl	B	−12.6	0.4	0.0	0.0					9	9
97	245	LV	1	Fl	A	−19.4	2.4	−28.4	0.7					12	12
110	475	LV10	1	Fl	B	−2.5	0.3							7	7
109	475	LV10	2	Fl	B	−8.1	2.7							8	8
108	475	LV10	3	Fl	A	−31.3	1.0	−27.4	2.6					14	14
107	475	LV2S	5	Fl	A	−24.6	0.6	−24.4	0.4					14	14
105*	475	LV2S	1	Fl	A	−24.9	0.6	−9.4	0.4					14	14
111	475	LV2S	3	Fl	A	−24.9	0.3	−4.1	0.3					15	15
106	475	LV2S	1a	Fl	A	−25.4	0.6	−5.5	0.6					10	10
104	475	LV2S	a	Fl	A	−26.2	0.7	−2.1	1.2					17	0
118	503	LV1	4	Fl	B	−10.5	0.8							7	7
117	503	LV1	1	Fl	B	−11.4	0.7							8	8
116	503	LVoN	2	Fl	A	−21.1	0.9	−20.4	0.8					3	3
115	503	LVoN	1	Fl	A	−25.2	1.0	−25.3	0.5					3	3
119	503	LVrS	2	Fl	A	−13.7	1.4	−24.9	2.8					4	4
121	503	LVrS	1	Fl	A	−18.2	1.2	−24.9	2.8					7	7
120	503	LVrS	3	Fl	A	−17.8	1.9	−24.9	2.8					5	5
80	81	LV1	2	Brt	A	−30.1	2.3	−8.5	n.d.			108.3	3.3	6	2
79*	81	LV10	1	Brt	B	n.d.	n.d.								
77	81	LV10	3	Brt	B	−0.3	0.1							6	6
78	81	LV10	2	Brt	B	n.d.	n.d.					145.9	12.1		
112*	462	LV10	1	Fl	B	−9.5	0.5							7	7
113*	462	LV10	2	Fl	B	−9.7	0.7							6	6
114*	462	LV10	3	Fl	A	−12.4	2.1	−22.2	0.6					11	11
135	251	LV1	1	Brt	B	−2.0	0.3							7	7
127*	251	LV10	2 c	Brt	B	−2.3	0.2					>220	n.d.	5	5
128*	251	LV10	3	Brt	B	n.d.	n.d.							n.d.	n.d.
129	251	LV10	1 d	Brt	B	−2.9	0.2					167.8	8.1	4	4
134	251	LV10	4	Brt	B	n.d.	n.d.							n.d.	n.d.
133	251	LV10	1	Brt	B	n.d.	n.d.							n.d.	n.d.
130	251	LV10	1 d2	Brt	B	−3.2	0.8					>200	n.d.	7	7
Hematite-aluminosilicate clast replacement															
123	505	LV10	2	Cal	A	−23.8	0.4	−9.6	0.8					15	15
125	505	LV10S	3	Fl	A	−25.2	0.5	−18.4	2.4					8	8
126	505	LV10S	1	Fl	A	−24.0	0.8	−12.2	3.0					13	13
124	505	LV10S	4	Fl	A	−27.2	0.5	−3.3	1.0					8	0
122*	505	LVoS	1	Fl	A	−16.1	1.2	−28.0	0.5					8	8

Table A2. *(Continued)*

ID	Sample	FI-type	FIA-No.	Host	Model	T ice	±	T HH	+-	T_h lh-l	+-	T_h lv-l	+-	n (tot)	n
Siderite + quartz + fluorite + chalcopyrite veins															
65	15.2	LH5HS	2	Qtz	A	−27.4	0.0	14.7	0.3	260.6	4.6	133.4	5.8	5	5
27	15	LH5HS	1	Qtz	A	−27.5	0.1	15.8	1.9	259.2	8.9	119.9	9.8	10	10
28	15	LH5HS	2	Qtz	A	−27.4	n.d.	n.d.	n.d.	264.2	n.d.			n.d.	n.d.
29	15	LH5HS	4	Qtz	A	−27.3	1.4	14.2	3.8	269.3	4.1	108.4	5.9	8	8
67	15.2	LH5HS	4	Qtz	A	−32.2	1.9	n.d.	n.d.	267.1	4.6	131.9	5.4	5	5
66*	15	LV40	1	Qtz	B	−0.9	0.2					332.0	20.0	6	6
63	17	LH5HS	2	Qtz	A	−26.5	2.1	7.5	2.1	248.9	n.d.	106.8	1.3	5	5
64	15.2	LH5HS	1	Qtz	A	−27.4	0.6	16.1	2.9	258.7	8.6	130.1	10.8	9	9
Calcite + barite + pyrite + fluorite veins															
19	27	LV10S	17	Fl	A	−30.3	1.5	−22.3	n.d.					2	0
11	27	LV10S	5	Fl	A	−29.9	0.3	−11.8	0.8	7.2	0.3			5	5
16	27	LV10S	13	Fl	A	−27.5	0.1	6.9	n.d.					3	0
17	27	LV10S	15	Fl	A	n.d.	n.d.	n.d.	n.d.					n.d.	n.d.
20	27	LV10S	20	Fl	A	−30.7	0.2	−0.3	0.1					2	0
10	27	LV10S	3	Fl	A	−31.6	0.1	−4.8	1.0	11.3	0.3			5	0
14	27	LV10S	11	Fl	A	−30.3	2.9	8.3	2.0					6	0
12	27	LV10S	6	Fl	A	−29.6	2.2	11.1	0.6			> 140	n.d.	5	0
18	27	LV10S	16	Fl	A	−31.6	0.5	4.4	1.3					6	0
13	27	LV10S	7	Fl	A	−31.5	0.6	13.3	0.8					4	0
15	27	LV10S	12	Fl	A	−33.6	0.2	9.4	1.4					4	0
40	82	LV10S	6	Fl	A	−27.2	2.5	−28.6	1.0					7	7
49	82	LV10S	7	Fl	A	−27.5	0.9	−28.9	0.2					8	8
52	82	LV10S	9	Fl	A	−29.0	1.6	−27.2	1.9					9	9
53	82	LV10S	8	Fl	A	−29.4	1.0	−26.0	4.4					14	14
30	82	LV10S	1	Fl	A	−29.4	1.6	−26.0	3.7					5	5
32	82	LV10S	2	Fl	A	−30.1	0.8	−26.5	1.4					9	9
44	82	LV10S	BrCl	Fl	A	n.d.	n.d.	n.d.	n.d.					n.d.	n.d.
47	82	LV10S	5	Fl	A	−30.2	1.5	−24.5	6.1					8	8
35	82	LV15	1	Fl	A	−25.9	3.3	−22.0	n.d.					6	0
59	82	LV15	3	Fl	A	−29.7	0.9	−22.5	5.2					8	8
61	82	LV15	5	Fl	A	−29.6	0.8	−21.0	3.6			decrip. > 200	n.d.	14	14
62	82	LV15	4	Fl	A	−28.7	0.7	−20.1	3.1					6	6
42	82	LV20S	9	Fl	A	−29.5	0.9	−25.9	3.7					12	12
55	82	LV20S	11	Fl	A	−29.3	1.8	−23.9	4.3					10	10
34	82	LV20S	5	Fl	A	−31.4	0.6	−31.1	0.1					6	6
37	82	LV20S	6	Fl	A	−30.1	0.5	−20.9	2.7					4	3
31	82	LV20S	4	Fl	A	−30.6	2.5	−23.1	n.d.					4	4
38	82	LV20S	mix	Fl	A	−30.7	1.5	−20.6	4.0					6	6
41	82	LV20S	8	Fl	A	−31.1	2.1	−20.1	6.9					6	6
58	82	LV20S	12	Fl	A	−30.6	1.2	−16.9	4.5					19	19
60*	82	LV30S	Cp2	Fl	A	−29.1	1.6	−23.1	3.4					12	12
46	82	LV30S	4	Fl	A	−30.0	0.5	−20.8	3.6					6	6
56*	82	LV30S	Cp1	Fl	A	−30.1	1.2	−19.3	4.9					17	17
45	82	LV30S	3	Fl	A	n.d.	n.d.	n.d.	n.d.					n.d.	n.d.
33	82	LV30S	1	Fl	A	−31.7	1.1	−12.5	5.1					5	5
36	82	LV30S	2	Fl	A	−32.8	1.9	−17.6	1.0					11	9
50	82	LV40	2	Fl	A	−25.8	4.2	−7.7	n.d.					7	5
57	82	LV40	4	Fl	A	−31.8	0.3	−8.5	0.9					4	0
39	82	LV40	1	Fl	A	−33.4	0.8	−9.0	1.4					2	0
51	82	LVoS X	2	Fl	A	−16.2	13.1	−23.2	n.d.					4	3
43	82	LVoS X	1	Fl	A	−15.4	4.1	−28.0	0.6					10	9
54	82	LVoS U	2	Fl	B	−4.2	n.d.							1	1
48	82	LVoS U	1	Fl	B	−3.4	2.1							4	4
23	83	LV20S	2	Fl	A	−22.2	0.5	−19.5	n.d.					6	6
25	83	LV20S	6	Fl	A	−29.1	1.6	−28.8	0.1					7	7
22	83	LV20S	1	Fl	A	−27.9	0.3	−2.4	1.6					13	0
26	83	LV20S	5	Fl	A	−30.3	2.0	−10.3	0.8					7	7
24	83	LV30S	1	Fl	A	−31.0	2.6	−4.6	n.d.					2	0
21	83	LV30S	2	Fl	A	−32.3	3.3	−12.0	n.d.					2	1
6	98	LV10S	1	Fl	A	−25.9	0.7	−17.4	0.3					7	7
3	98	LV10S	1	Fl	A	−26.4	1.7	−5.7	0.6			111.3	13.0	11	10
2	98	LV15	1	Fl	A	−27.1	1.0	−27.6	0.9			322.7	19.4	6	6
4	98	LV20S	1	Fl	A	−29.6	2.4	−2.4	3.2			162.8	n.d.	6	6
1	98	LV40	1	Fl	A	−28.6	3.7	−5.6	0.8					4	3
9	98	LV5	3	Fl	A	−6.1	0.8	−25.0	n.d.					7	7

| 7 | 98 | LV5 | 1 | Fl | A | −6.4 | 0.8 | −24.0 | 0.1 | | | | | 4 | 4 |

Table A2. Cont.

ID	Sample	FI-type	FIA-No.	Host	Model	T ice	±	T HH	+-	T_h lh-l	+-	T_h lv-l	+-	n (tot)	n
Calcite + barite + pyrite + fluorite veins															
8	98	LV5	2	Fl	A	−20.6	0.8	−18.9	3.6					6	6
5	98	LVoS	1	Fl	B	−8.9	1.1							2	2
Hematite + quartz vein															
89	06	LV40	1	Qtz	A	n.d.	n.d.	n.d.	n.d.			353.7	28.0		
Magnetite + quartz vein															
69	50	LH5H	1	Qtz	A	−43.1	1.7	n.d.	n.d.	325.2	5.8	138.2	8.7	8	8
68	50	LH5H	4	Qtz	A	−43.1	n.d.	n.d.	n.d.	323.8	6.8	199.5	5.3	13	13
75	50	LV1	1	Qtz	A	−23.6	0.4	14.3	1.3			118.6	6.1	6	0
72	50	LV40	2	Qtz	A	−11.5	1.8	−24.5	0.3			475.4	13.9	4	2
70	50	LV5	1	Qtz	B	−1.1	0.1					> 210	n.d.	2	2
71	50	LV5	2	Qtz	B	−18.4	0.5					154.6	11.2	4	4
73	50	LV5H	3	Qtz	A	−25.3	1.7	9.2	5.5	324.5	n.d.	141.1	12.7	3	0
74	50	LV5H	2	Qtz	A	−38.8	n.d.	n.d.	n.d.	324.5	n.d.	182.0	9.4	7	7
76	50	LV5HSS	1	Qtz	A	−40.0	0.0	n.d.	n.d.	277.8	12.9	170.4	11.2	9	0

Abbreviations ID, Unique identification number for the fluid inclusion assemblage (FIA) used in this study

A, H_2O–NaCl–$CaCl_2$ and B, H_2O–NaCl fluid model

T ice, ice melting, T HH, hydrohalite melting; T lh-l, total homogenization by halite dissolution; T lv-l, homogenization by vapor disappearance

±, standard deviation; n(tot), total inclusions measured per assemblage; n, inclusion without metastable melting

Brt, Barite; Cal, Calcite; Fl, fluorite; Qtz, quartz

X, heterogeneously trapped Fe, Cu and S-rich crystal; U, heterogeneously trapped U-bearing mineral.

n.d., not determined

*, FIA associated with Cu-(Fe) sulfide formation

Table A3. Average NaCl + CaCl₂ salinity data derived by two phase melting temperatures during microthermometry. Data sorted according to sample type, FI-type and total salinity S (in wt.%).

ID	Sample	FI-type	FIA-No	Host	Model	R	+-	S	+-	NaCl	+-	CaCl$_2$	+-	Cl	+-	Na	+-	Ca	+-
Hematite-aluminosilicate breccia matrix																			
88	238	LV10S	2	Fl	A	0.56	0.03	25.6	0.5	14.3	0.7	11.3	0.8	15.9	0.3	5.63	0.26	4.07	0.30
85*	238	LV10S	1	Fl	A	0.38	0.05	26.2	0.4	10.0	1.1	16.2	1.4	16.4	0.3	3.93	0.44	5.86	0.51
87	238	LV2S	6	Fl	A	0.37	0.04	21.1	0.9	7.7	0.9	13.4	0.9	13.2	0.6	3.04	0.35	4.82	0.32
84*	238	LV2S	1	Fl	A	0.62	0.07	21.8	1.2	13.6	1.3	8.2	1.6	13.5	0.7	5.35	0.50	2.97	0.58
86	238	LV2S	5	Fl	A	0.52	0.05	22.1	0.8	11.5	1.2	10.6	1.3	13.8	0.5	4.53	0.47	3.83	0.47
82	238	LV2S	4a	Fl	A	0.47	0.04	22.1	1.3	10.4	1.3	11.8	0.9	13.8	0.8	4.08	0.52	4.25	0.34
83	238	LV2S	3b	Fl	A	0.41	0.01	22.3	0.8	9.3	0.5	13.1	0.4	14.0	0.5	3.64	0.20	4.72	0.15
81*	238	LV2S	2	Fl	A	0.60	0.05	26.9	0.1	16.2	1.3	10.7	1.4	16.7	0.1	6.39	0.50	3.85	0.50
102	245	LV10S	8	Fl	A	0.52	0.03	26.4	0.2	13.8	0.8	12.6	1.0	16.4	0.2	5.43	0.32	4.56	0.36
99	245	LV10S	7	Fl	A	0.72	0.09	26.5	0.2	19.2	2.2	7.3	2.5	16.3	0.2	7.55	0.87	2.65	0.89
93	245	LV10S	3	Fl	A	0.63	0.05	26.7	0.2	16.8	1.1	10.0	1.3	16.5	0.2	6.59	0.45	3.60	0.48
96	245	LV10S	1	Fl	A	0.56	0.05	26.9	0.2	15.2	1.3	11.7	1.5	16.7	0.2	5.96	0.53	4.24	0.55
91	245	LV10S	2	Fl	A	0.50	0.02	27.3	0.1	13.6	0.4	13.8	0.5	17.0	0.1	5.34	0.15	4.98	0.16
95	245	LV10S	4	Fl	A	0.48	0.02	27.4	0.1	13.1	0.6	14.3	0.7	17.1	0.1	5.15	0.23	5.16	0.26
101	245	LV15	1	Fl	A	0.34	0.02	22.8	0.5	7.8	0.7	15.0	0.3	14.3	0.3	3.09	0.26	5.42	0.12
94	245	LV20S	1	Fl	B	1.00		20.8	0.2	20.8	0.2			12.6	0.1	8.19	0.09		
92*	245	LV2S	2	Fl	A	0.63	0.03	26.4	0.2	16.7	0.7	9.7	0.8	16.3	0.2	6.57	0.26	3.50	0.30
98	245	LV2S	3	Fl	A	0.75	0.09	26.5	0.3	19.9	2.3	6.6	2.5	16.3	0.2	7.82	0.89	2.37	0.90
90	245	LV2S	1	Fl	A	0.54	0.02	27.2	0.1	14.6	0.6	12.5	0.7	16.9	0.1	5.76	0.23	4.53	0.24
100	245	LV2oS	1	Fl	B	1.00		16.5	0.2	16.5	0.2			10.0	0.1	6.50	0.09		
97	245	LVx	1	Fl	A	0.37	0.01	20.8	1.5	7.7	0.7	13.1	0.9	13.0	1.0	3.02	0.26	4.74	0.33
110	475	LV10	1	Fl	B	1.00	0.00	4.2	0.4	4.2	0.4			2.6	0.2	1.66	0.14		
109	475	LV10	2	Fl	B	1.00		11.7	2.0	11.7	2.0			7.1	1.2	4.61	0.78		
108	475	LV10	3	Fl	A	0.27	0.02	26.9	0.2	7.3	0.4	19.5	0.6	16.9	0.2	2.87	0.14	7.06	0.20
107	475	LV2S	5	Fl	A	0.60	0.04	24.5	0.2	14.8	0.9	9.7	1.1	15.2	0.2	5.84	0.35	3.50	0.39
105*	475	LV2S	1	Fl	A	0.63	0.05	26.4	0.2	16.6	1.3	9.7	1.5	16.3	0.2	6.55	0.51	3.52	0.54
111	475	LV2S	3	Fl	A	0.64	0.02	26.8	0.1	17.2	0.5	9.5	0.5	16.5	0.1	6.76	0.18	3.46	0.19
106	475	LV2S	1a	Fl	A	0.59	0.04	26.9	0.2	15.8	0.9	11.0	1.1	16.7	0.1	6.23	0.36	3.99	0.39
104	475	LV2S	a	Fl	A	0.56	0.04	27.2	0.2	15.3	1.0	11.9	1.2	16.9	0.1	6.00	0.41	4.31	0.43
118	503	LV1	4	Brt	B	1.00		15.2	0.8	15.2	0.8			9.2	0.5	5.98	0.32		
117	503	LV1	1	Brt	B	1.00		15.4	0.6	15.4	0.6			9.4	0.4	6.07	0.24		
116	503	LVoN	2	Brt	A	0.91	0.07	23.8	0.4	21.6	1.3	2.2	1.7	14.5	0.3	8.51	0.52	0.79	0.61
115	503	LVoN	1	Brt	A	0.53	0.02	24.6	0.6	13.0	0.4	11.7	0.6	15.3	0.4	5.10	0.18	4.21	0.23
119	503	LVrS	2	Brt	A	0.59	0.00	17.2	1.1	10.1	0.6	7.1	0.5	10.6	0.7	3.96	0.26	2.57	0.17
121	503	LVrS	1	Brt	A	0.60	0.11	20.4	0.8	12.1	2.0	8.3	2.2	12.6	0.5	4.76	0.79	2.99	0.81
120	503	LVrS	3	Brt	A	0.59	0.00	20.7	1.1	12.1	0.6	8.6	0.4	12.8	0.7	4.78	0.24	3.10	0.16
80	81	LV1	2	Brt	A	0.48	0.01	27.1	0.0	13.0	0.2	14.1	0.2	16.9	0.0	5.12	0.07	5.09	0.08
79*	81	LV10	1	Brt	B	1.00		0.6	0.1	0.6	0.1			0.3	0.1	0.22	0.05		
77	81	LV10	3	Brt	B	1.00		0.6	0.1	0.6	0.1			0.3	0.1	0.22	0.05		
78	81	LV10	2	Brt	B														
112*	462	LV10	1	Fl	B	1.00		13.4	0.5	13.4	0.5			8.1	0.3	5.25	0.21		
113*	462	LV10	2	Fl	B	1.00		13.6	0.8	13.6	0.8			8.2	0.5	5.33	0.30		
114*	462	LV10	3	Fl	A	0.86	0.07	16.2	1.9	14.0	2.7	2.2	0.9	9.9	1.1	5.53	1.04	0.78	0.33
135	251	LV1	1	Brt	B	1.00		3.5	0.5	3.5	0.5			2.2	0.3	1.39	0.18		
127*	251	LV10	2c	Brt	B	1.00		3.8	0.3	3.8	0.3			2.3	0.2	1.50	0.11		
128*	251	LV10	3	Brt	B	1.00		3.8	0.3	3.8	0.3			2.3	0.2	1.50	0.11		
129	251	LV10	1d	Brt	B	1.00		4.8	0.4	4.8	0.4			2.9	0.2	1.89	0.15		
134	251	LV10	4	Brt	B	1.00		5.0	0.8	5.0	0.8			3.1	0.5	1.98	0.30		
133	251	LV10	1	Brt	B	1.00		5.0	0.8	5.0	0.8			3.1	0.5	1.98	0.30		
130	251	LV10	1d2	Brt	B	1.00		5.3	1.1	5.3	1.1			3.2	0.7	2.07	0.45		
Hematite breccia clast replacement																			
123	505	LV10	2	Cal	A	0.72	0.03	26.0	0.1	18.7	0.6	7.3	0.7	16.0	0.1	7.36	0.25	2.65	0.26
125	505	LV10S	3	Fl	A	0.59	0.04	25.5	0.3	15.0	0.7	10.5	1.0	15.8	0.2	5.91	0.29	3.79	0.36
126	505	LV10S	1	Fl	A	0.70	0.06	25.8	0.3	18.1	1.5	7.8	1.8	15.9	0.2	7.10	0.58	2.80	0.63
124	505	LV10S	4	Fl	A	0.50	0.03	27.4	0.1	13.8	0.7	13.6	0.8	17.1	0.1	5.41	0.27	4.92	0.29
122*	505	LV10oS	1	Fl	A	0.39	0.01	18.8	0.7	7.3	0.2	11.5	0.6	11.8	0.5	2.88	0.09	4.15	0.20

Table A3. *(Continued)*

ID	Sample	FI-type	FIA-No	Host	Model	R	+-	S	+-	NaCl	+-	CaCl₂	+-	Cl	+-	Na	+-	Ca	+-
Siderite + quartz + fluorite + chalcopyrite veins																			
65	15.2	LH5HS	2	Qtz	A	0.73	0.01	37.2	0.3	27.2	0.5	10.0	0.1	22.9	0.2	10.67	0.18	3.62	0.05
27	15.1	LH5HS	1	Qtz	A	0.73	0.01	37.2	0.3	27.0	0.4	10.1	0.2	22.9	0.2	10.63	0.15	3.66	0.05
28	15.1	LH5HS	2	Qtz	A	0.74	n.d.	37.5	n.d.	27.6	n.d.	9.8	n.d.	23.0	n.d.	10.86	n.d.	3.55	n.d.
29	15.1	LH5HS	4	Qtz	A	0.75	0.03	37.8	0.6	28.2	0.9	9.5	1.3	23.2	0.4	11.10	0.34	3.45	0.47
67	15.2	LH5HS	4	Qtz	A	0.66	0.02	39.3	0.4	26.1	0.5	13.2	0.7	24.3	0.3	10.27	0.20	4.77	0.26
66*	15.2	LV40	1	Qtz	B	1.00		1.6	0.2	1.6	0.2			1.0	0.1	0.64	0.08		
63	17	LH5HS	2	Qtz	A	0.75	0.06	36.0	0.8	26.9	1.6	9.1	2.4	22.1	0.6	10.60	0.65	3.28	0.88
64	17	LH5HS	1	Qtz	A	0.73	0.01	37.1	0.5	27.1	0.4	10.0	0.4	22.8	0.3	10.64	0.17	3.62	0.13
Calcite + barite + pyrite + fluorite veins																			
19	27	LV10S	17	Fl	A	0.32	0.05	26.9	0.5	8.7	1.2	18.2	1.6	16.9	0.3	3.43	0.46	6.56	0.59
11	27	LV10S	5	Fl	A	0.36	0.01	27.5	0.1	10.0	0.3	17.5	0.4	17.3	0.1	3.95	0.11	6.32	0.13
16	27	LV10S	13	Fl	A	0.50	0.00	27.8	0.0	13.8	0.1	14.0	0.1	17.3	0.0	5.44	0.05	5.04	0.05
17	27	LV10S	15	Fl	A	0.37	n.d.	28.4	n.d.	10.5	n.d.	17.9	0.0	17.8	n.d.	0.54	n.d.	0.08	n.d.
20	27	LV10S	20	Fl	A	0.37	0.01	28.4	0.1	10.5	0.2	17.9	0.2	17.8	0.0	4.13	0.07	6.47	0.08
10	27	LV10S	3	Fl	A	0.33	0.00	28.4	0.0	9.4	0.1	19.0	0.1	17.9	0.0	3.70	0.05	6.87	0.05
14	27	LV10S	11	Fl	A	0.40	0.08	28.6	0.7	11.4	1.9	17.2	2.6	17.9	0.5	4.48	0.75	6.20	0.94
12	27	LV10S	6	Fl	A	0.39	0.06	28.7	0.6	11.3	1.5	17.4	2.1	18.0	0.5	4.44	0.59	6.28	0.77
18	27	LV10S	16	Fl	A	0.35	0.01	28.9	0.1	10.1	0.3	18.8	0.4	18.1	0.1	3.96	0.14	6.78	0.16
13	27	LV10S	7	Fl	A	0.36	0.02	29.0	0.2	10.5	0.4	18.5	0.6	18.2	0.1	4.12	0.16	6.68	0.22
15	27	LV10S	12	Fl	A	0.31	0.00	29.5	0.1	9.2	0.1	20.3	0.1	18.6	0.0	3.60	0.02	7.35	0.05
40	82	LV10S	6	Fl	A	0.34	0.05	25.0	1.2	8.6	1.0	16.5	1.8	15.7	0.8	3.36	0.37	5.95	0.66
49	82	LV10S	7	Fl	A	0.35	0.01	25.2	0.4	8.8	0.2	21.7	2.4	19.2	1.6	3.45	0.08	7.84	0.88
52	82	LV10S	9	Fl	A	0.36	0.07	26.2	0.7	9.3	1.5	16.8	2.1	16.4	0.5	3.67	0.59	6.08	0.74
53	82	LV10S	8	Fl	A	0.33	0.03	26.3	0.6	8.7	0.7	17.7	1.0	16.6	0.4	3.41	0.27	6.38	0.37
30	82	LV10S	1	Fl	A	0.33	0.02	26.4	0.8	8.6	0.7	17.8	0.7	16.6	0.5	3.38	0.26	6.42	0.26
32	82	LV10S	2	Fl	A	0.31	0.02	26.5	0.3	8.2	0.6	18.3	0.9	16.7	0.2	3.24	0.22	6.60	0.31
44	82	LV10S	BrCl	Fl	A	0.32	n.d.	26.6	n.d.	8.6	n.d.	18.0	n.d.	16.7	n.d.	3.40	n.d.	6.50	n.d.
47	82	LV10S	5	Fl	A	0.31	0.04	26.7	0.8	8.3	0.9	18.3	1.5	16.8	0.5	3.27	0.36	6.62	0.53
35	82	LV15	1	Fl	A	0.56	0.16	25.3	1.0	13.9	3.6	11.4	4.5	15.7	0.7	5.48	1.41	4.11	1.64
59	82	LV15	3	Fl	A	0.34	0.02	26.7	0.5	9.0	0.5	17.6	1.0	16.7	0.4	3.56	0.21	6.36	0.35
61	82	LV15	5	Fl	A	0.35	0.03	26.7	0.4	9.4	0.6	17.4	0.9	16.8	0.3	3.68	0.24	6.28	0.32
62	82	LV15	4	Fl	A	0.39	0.02	26.7	0.3	10.5	0.6	16.2	0.8	16.7	0.2	4.13	0.22	5.86	0.28
42	82	LV20S	9	Fl	A	0.33	0.02	26.3	0.5	8.7	0.4	17.6	0.8	16.5	0.4	3.43	0.16	6.35	0.30
55	82	LV20S	11	Fl	A	0.35	0.06	26.4	0.7	9.3	1.4	17.1	2.0	16.6	0.5	3.64	0.56	6.19	0.71
34	82	LV20S	5	Fl	A	0.26	0.01	26.6	0.2	6.9	0.3	19.8	0.4	16.8	0.1	2.70	0.10	7.14	0.16
37	82	LV20S	6	Fl	A	0.34	0.01	26.9	0.3	9.0	0.3	17.9	0.5	16.9	0.2	3.55	0.12	6.45	0.18
31	82	LV20S	4	Fl	A	0.32	0.08	27.0	0.8	8.7	1.9	18.3	2.6	17.0	0.6	3.42	0.74	6.61	0.95
38	82	LV20S	mix	Fl	A	0.31	0.04	27.0	0.6	8.4	0.9	18.6	1.5	17.0	0.4	3.32	0.37	6.72	0.52
41	82	LV20S	8	Fl	A	0.31	0.06	27.3	0.8	8.3	1.4	18.9	2.0	17.1	0.5	3.28	0.54	6.83	0.74
58	82	LV20S	12	Fl	A	0.33	0.03	27.4	0.5	9.0	0.8	18.3	1.2	17.2	0.3	3.55	0.32	6.64	0.42
60*	82	LV30S	Cp2	Fl	A	0.37	0.05	26.6	0.6	9.9	1.0	16.7	1.5	16.7	0.4	3.88	0.41	6.04	0.55
46	82	LV30S	4	Fl	A	0.33	0.01	26.9	0.4	9.0	0.1	17.9	0.5	16.9	0.3	3.52	0.04	6.48	0.17
56*	82	LV30S	Cp1	Fl	A	0.34	0.04	27.0	0.6	9.2	0.8	17.9	1.3	17.0	0.4	3.61	0.33	6.46	0.48
45	82	LV30S	3	Fl	A	0.30	n.d.	27.5	n.d.	8.3	n.d.	19.2	n.d.	17.3	n.d.	3.25	n.d.	6.94	n.d.
33	82	LV30S	1	Fl	A	0.29	0.03	27.6	0.3	8.0	0.7	19.8	1.5	17.5	0.6	3.16	0.29	7.14	0.56
36	82	LV30S	2	Fl	A	0.28	0.02	27.8	0.2	7.8	0.5	20.0	0.8	17.5	0.2	3.06	0.21	7.21	0.28
50	82	LV40	2	Fl	A	0.75	0.18	26.2	0.0	19.4	4.1	6.7	4.7	16.1	0.5	7.65	1.63	2.43	1.70
57	82	LV40	4	Fl	A	0.32	0.01	28.3	0.0	8.9	0.2	19.3	0.2	17.8	0.0	3.52	0.06	6.97	0.06
39	82	LV40	1	Fl	A	0.28	0.02	28.6	0.1	7.9	0.6	20.7	0.7	18.0	0.1	3.13	0.23	7.46	0.25
51	82	LVoS X	2	Fl	A	0.75	0.00	13.4	7.7	10.0	5.8	3.4	2.0	8.2	4.7	3.93	2.27	1.23	0.71
43	82	LVoS X	1	Fl	A	0.39	0.03	17.9	3.1	6.9	1.0	11.0	2.2	11.2	2.0	2.73	0.40	3.96	0.80
54	82	LVoS U	2	Fl	B	1.00		2.6	0.0	2.6	0.0			1.6	0.0	1.01	0.00		
48	82	LVoS U	1	Fl	B	1.00		5.4	2.5	5.4	2.5			3.3	1.5	2.14	0.99		
23	83	LV20S	2	Fl	A	0.88	0.06	24.2	0.2	21.2	1.3	3.0	1.5	14.8	0.2	8.33	0.49	1.10	0.54
25	83	LV20S	6	Fl	A	0.33	0.04	25.9	0.7	8.4	0.8	17.5	1.4	16.3	0.4	3.32	0.33	6.30	0.52
22	83	LV20S	1	Fl	A	0.47	0.01	27.6	0.1	12.9	0.3	14.7	0.3	17.2	0.1	5.08	0.10	5.31	0.12
26	83	LV20S	5	Fl	A	0.36	0.01	27.7	0.1	9.9	0.2	17.9	0.3	17.4	0.1	3.89	0.08	6.45	0.10
24	83	LV30S	1	Fl	A	0.36	0.08	28.3	0.7	10.1	2.0	18.2	2.7	17.7	0.5	3.97	0.79	6.56	0.96
21	83	LV30S	2	Fl	A	0.33	0.05	28.6	1.5	9.3	1.0	19.4	2.5	18.0	1.0	3.65	0.38	6.99	0.90
6	98	LV10S	1	Fl	A	0.54	0.04	25.9	0.2	14.0	1.0	11.9	1.3	16.1	0.2	5.50	0.40	4.30	0.45
3	98	LV10S	1	Fl	A	0.57	0.02	26.9	0.1	15.3	0.4	11.6	0.5	16.7	0.1	6.03	0.17	4.19	0.18
2	98	LV15	1	Fl	A	0.40	0.02	25.2	0.5	10.2	0.5	15.0	0.8	15.8	0.3	4.02	0.20	5.42	0.28
4	98	LV20S	1	Fl	A	0.41	0.07	28.0	0.5	11.4	1.8	16.6	2.3	17.6	0.4	4.49	0.72	6.01	0.84
1	98	LV40	1	Fl	A	0.44	0.09	27.6	0.6	12.2	2.3	15.4	2.8	17.2	0.4	4.79	0.89	5.57	1.02
9	98	LV5	3	Fl	A	0.58	0.00	9.7	1.0	5.6	0.6	4.1	0.4	6.0	0.6	2.21	0.22	1.48	0.15
7	98	LV5	1	Fl	A	0.67	0.00	10.0	1.0	6.7	0.6	3.3	0.3	6.2	0.6	2.63	0.24	1.20	0.12

Table A3. *(Continued)*

ID	Sample	FI-type	FIA-No	Host	Model	R	+-	S	+-	NaCl	+-	CaCl₂	+-	Cl	+-	Na	+-	Ca	+-
Calcite + barite + pyrite + fluorite veins																			
8	98	LV5	2	Fl	A	1.00	0.00	23.3	1.1	23.2	1.1	0.1	0.0	14.1	0.7	9.13	0.44	0.02	0.00
5	98	LVoS X	1	Fl	B	1.00		12.7	1.2	12.7	1.2			7.7	0.7	4.98	0.47		
Magnetite + quartz vein																			
69	50	LH5H	1	Qtz	A	0.70	0.01	45.4	0.2	31.6	0.4	13.8	0.3	28.0	0.1	12.43	0.17	4.98	0.11
68	50	LH5H	4	Qtz	A	0.70	0.01	45.4	0.4	31.7	0.8	13.8	0.4	28.0	0.2	12.46	0.31	4.97	0.13
75	50	LV1	1	Qtz	A	0.75	0.03	26.6	0.1	19.9	0.7	6.7	0.8	16.3	0.1	7.81	0.27	2.43	0.29
72	50	LV30	2	Qtz	A	0.62	0.01	15.8	1.6	9.8	1.2	6.0	0.5	9.8	1.0	3.84	0.46	2.16	0.18
70	50	LV5	1	Qtz	B	1.00		1.9	0.2	1.9	0.2			1.2	0.1	0.75	0.09		
71	50	LV5	2	Qtz	B	1.00	0.00	21.3	0.4	21.3	0.4			12.9	0.2	8.39	0.15		
73	50	LV5H	3	Qtz	A	0.85	0.03	41.3	0.5	35.2	0.7	6.0	1.3	25.2	0.4	13.86	0.28	2.18	0.46
74	50	LV5H	2	Qtz	A	0.71	0.00	44.8	0.0	31.9	0.0	12.9	n.d.	27.6	0.0	12.54	0.00	4.66	0.00
76	50	LV5HSS	1	Qtz	A	0.62	0.01	41.7	0.4	26.0	0.8	15.7	0.3	25.8	0.2	10.21	0.30	5.69	0.12

Abbreviations FIA-ID: Unique identification number for the fluid inclusion assemblage (FIA) uses in this study.

A, H₂O–NaCl–CaCl₂; B, H₂O–NaCl fluid model; R, NaCl/(NaCl + CaCl₂); S, NaCl + CaCl₂; ±, standard deviation.

Brt, Barite; Cal, Calcite; Fl, fluorite; Qtz, quartz.

X, heterogeneously trapped Fe, Cu and S-rich crystal; U, heterogeneously trapped U-mineral

*, FIA associated with Cu-(Fe) sulfide formation
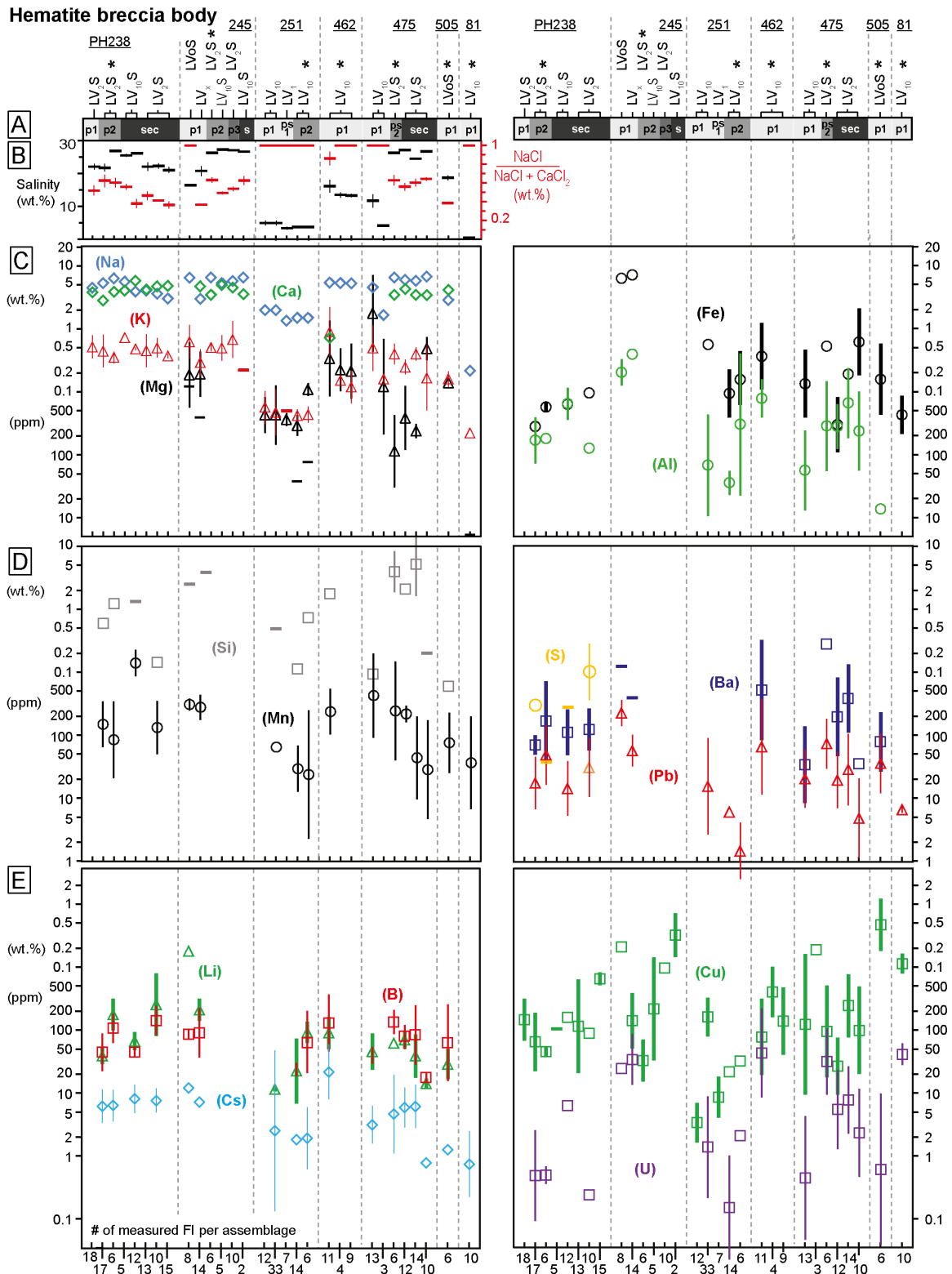
Fig. A1. Data compilation of the chemical composition of fluid inclusion assemblages (FIA) hosted in matrix minerals of the hematite-aluminosilicate breccia. The diagram displays the results of (A) fluid inclusion petrography, (B) microthermometry and (C-E) LA-SF-ICP-MS microanalysis (element concentration in ppm by weight). The FIA are grouped according to samples and sorted within each sample according to the relative timing. Stars (*) mark FIA that are most clearly associated with Cu-(Fe) sulfide precipitation in each sample (cf. Fig. 5). Symbols represent the average values for an element and the error bars are the 1 σ standard deviation. Horizontal lines are limits of detection (LOD) in cases where the element could not be measured in a given FIA. Note the pronounced differences in Ca/Na ratios and concentrations of ore-forming elements such as Fe, Cu and S within petrographically well-constrained FIA. Abbreviations: p: primary, ps: pseudosecondary, sec, s: secondary.

56
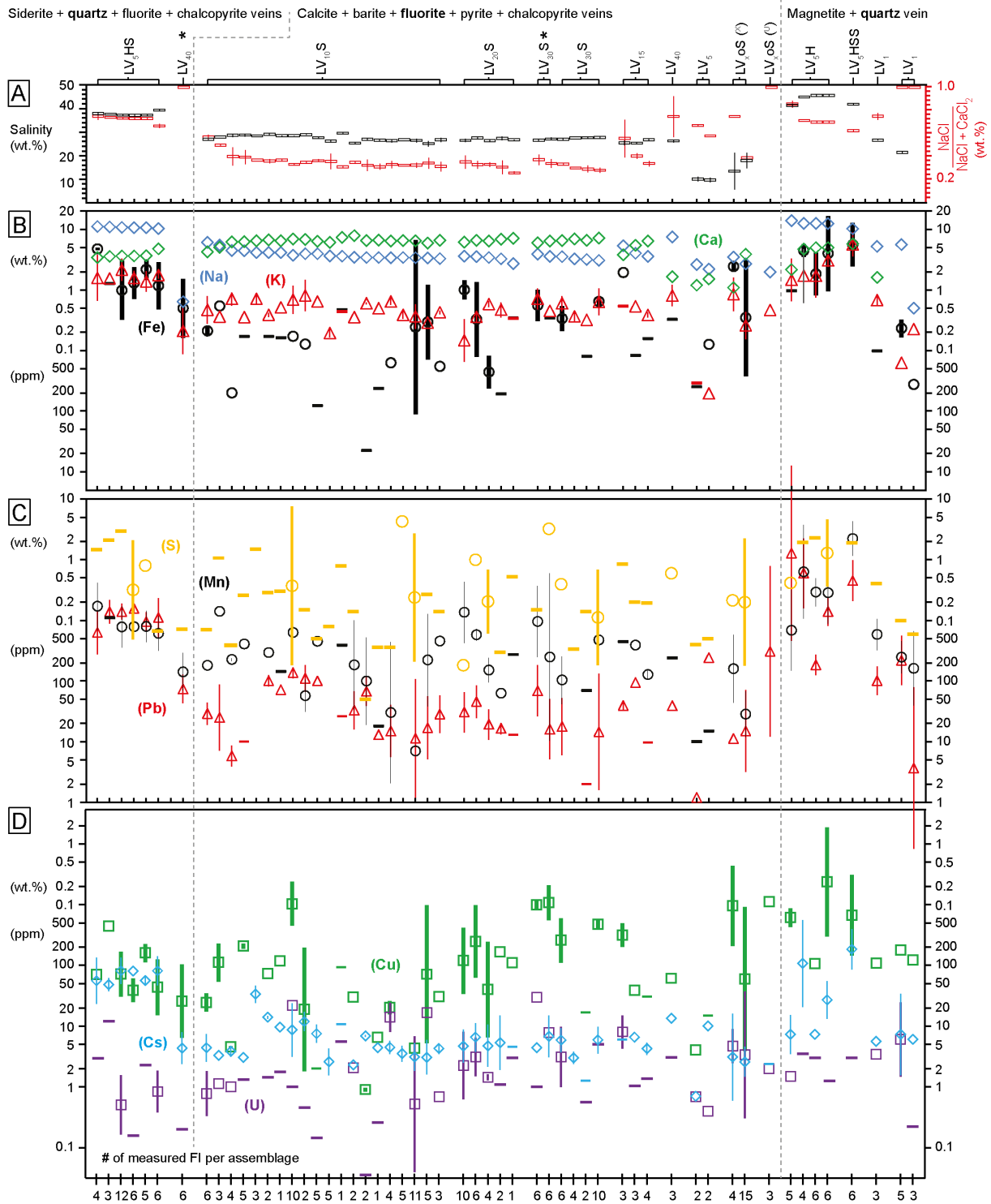
Fig. A2. Data compilation of the chemical composition of fluid inclusion assemblages (FIA) hosted in veins crosscutting the hematite-aluminosilicate breccia and the magnetite skarn. The diagram displays the results of (A) microthermometry and (B-D) LA-Q-ICP-MS microanalysis. Symbols represent the average values for an element and the error bars are the 1 σ standard deviation. Horizontal lines are limits of detection (LOD) in cases where the element could not be measured in a given FIA. Bold mineral names indicate the fluid inclusion host mineral. Stars (*) mark FIA associated with chalcopyrite mineralization. Superscripts X and U denote FIA that accidentally trapped Fe, Cu, Mn, S and U rich minerals, thus concentrations for these elements were not used for calculating assemblage averages. Note the pronounced differences in Ca/Na ratios and concentrations of ore-forming elements such as Fe, Cu and S between FIA of different samples types and within petrographically well-constrained FIA.

Table A4a. Average composition including standard deviation of fluid inclusion assemblages in the hematite-aluminosilicate breccia matrix determined by LA-ICP-SF-MS and microthermometry. Data is ordered according to sample-type, inclusion-subtype and decreasing Na-content. Concentration in ppm.

ID	Sample	Type	FIA-No	n	Li	±	B	±	Na	±	Mg	±	Al	±	Si	±	S	±	Cl	±	K	±
Hematite-aluminosilicate breccia matrix																							
88	238	LV10S	2	5					56000	2600									160000	7500	7200	n.d.
85*	238	LV10S	1	12	63	20	42	7.1	39000	4400			650	360	<13000	n.d.	<210	n.d.			4800	260
81	238	LV2S	2	6	180	84	110	63	64000	5000			160	n.d.	12000	n.d.	<29	n.d.			3900	1200
84*	238	LV2S	1	17	62	22	51	44	54000	5000			180	140	6000	n.d.	230	n.d.			5000	1800
86	238	LV2S	5	18					45000	4700									170000	33000	5600	2200
82	238	LV2S	4a	13					41000	5200									160000	37000	5200	2500
83	238	LV2S	3b	10	320	220	140	67	36000	2000			120	n.d.	1400	n.d.	950	830			5300	1900
87	238	LV2S	6	5					30000	3500									110000	6500	3700	330
93	245	LV10S	3	2					66000	4500									<60000	n.d.	<2200	n.d.
91	245	LV10S	2	5					53000	1500									160000	43000	5300	2100
100	245	LV2oS	1	8	1600	n.d.	78	14	65000	870	2500	2100	2000	1000	<25000	n.d.					7200	4100
92*	245	LV2S	2	6					66000	2600									190000	91000	5100	700
90	245	LV2S	1	10					58000	2300									170000	32000	8200	6500
97	245	LVx	1	14	200	77	100	80	30000	2600	2300	2200	4700	n.d.	<42000	n.d.					3200	1500
109	475	LV10	2	13	49	26	38	12	46000	8000	26000	18000	95	92	930	n.d.					6500	4500
110	475	LV10	1	3					17000	1400	2000	2300							70000	27000	1600	190
111	475	LV2S	3	10	13	2.1	16	2.9	68000	1900	4900	2500	420	560	<2000	n.d.					2600	2100
105*	475	LV2S	1	6	56	n.d.	130	60	66000	5100	150	150	530	510	45000	31000					4200	1300
107	475	LV2S	5	14	46	37	140	185	58000	3500	220	56	1000	950	74000	61000					4100	1100
104	475	LV2S	a	12	67	20	77	34	60000	4200	560	530	340	330	21000	n.d.					2600	620
114*	462	LV10	3	11	94	51	220	316	55000	10000	5200	5200	780	500	18000	n.d.					14000	19000
113*	462	LV10	2	4					53000	3000	2400	1700							110000	63000	1500	210
112*	462	LV10	1	9					53000	2000	2500	1800							110000	17000	1300	570
79	81	LV10	1	10					2200	470									11000	18000	220	n.d.
135	251	LV1	1	7					14000	1900	330	69							360000	5200	<500	n.d.
134	251	LV10	4	12					20000	n.d.	460	270							40000	8200	640	290
133	251	LV10	1	33	10	0.7			20000	3000	610	590	160	160	<4900	n.d.			46000	7400	630	520
128*	251	LV10	3	6	87	33	81	58	15000	1100	980	230	830	770	7400	n.d.					450	140
127*	251	LV10	2c	14	28	27	22	5.3	15000	1100	280	96	35	15	1100	n.d.					430	97
Hematite-aluminosilicate clast replacement																							
122	505	LV10oS	1	6	29	17	170	320	29000	900	1200	n.d.	13	n.d.	590	n.d.					1600	480

Table A4a. *(Continued)*

ID	Sample	Type	FIA-No	n	Ca	±	Mn	±	Fe	±	Cu	±	Br	±	As	±	Cs	±	Ba	±	Pb	±	U	±
Hematite-aluminosilicate breccia matrix																								
88	238	LV10S	2	5	41000	3000					<95	n.d.	<2300	n.d.										
85*	238	LV10S	1	12	59000	5100	1500	670	640	n.d.	150	n.d.			<110	n.d.	8.2	4.4	130	110	21	19	5.7	n.d.
81	238	LV2S	2	6	39000	5000	130	140	580	92	42	7			<25	n.d.	6.6	4.0	310	420	69	50	0.5	0.2
84*	238	LV2S	1	17	30000	5800	190	140	310	n.d.	90	93			<31	n.d.	6.7	4.9	66	21	24	17	0.8	0.7
86	238	LV2S	5	18	38000	4700					170	120	2900	280										
82	238	LV2S	4a	13	43000	3400					500	1200	780	470										
83	238	LV2S	3b	10	47000	1500	190	180	960	n.d.	81	n.d.			<25	n.d.	7.3	2.8	140	120	53	74	0.2	n.d.
87	238	LV2S	6	5	48000	3200					600	140	<880	n.d.										
93	245	LV10S	3	2	36000	4800					3400	2500	<4900	n.d.										
91	245	LV10S	2	5	50000	1600					400	490	<1200	n.d.										
100	245	LV2oS	1	8			310	68	65000	n.d.	1900	n.d.					11	n.d.	<1100	n.d.	240	98	22	n.d.
92*	245	LV2S	2	6	35000	3000					34	24	1100	n.d.										
90	245	LV2S	1	10	45000	2400					880	n.d.	2500	110										
97	245	LVx	1	14	47000	3300	300	110	79000	n.d.	160	140					6.5	n.d.	<350	n.d.	64	36	42	42
109	475	LV10	2	13			910	990	2500	3300	910	1700					3.4	2.0	56	60	31	25	2.2	3.5
110	475	LV10	1	3							1030	n.d.	420	190										
111	475	LV2S	3	10	35000	1900	74	90	870	8500	160	130					0.7	n.d.	32	n.d.	10	12	3.6	4.2
105*	475	LV2S	1	6	35000	5400	470	410	5300	n.d.	190	200					4.6	4.6	2400	n.d.	110	120	41	29
107	475	LV2S	5	14	35000	3900	100	150	1900	n.d.	390	420					8.0	9.4	600	620	60	86	14	21
104	475	LV2S	a	12	43000	4400	220	65	400	300	35	31					6.9	6.3	350	450	30	28	9.0	8.8
114*	462	LV10	3	11	7800	3300	310	250	6300	6700	200	370					34	50	1100	1300	180	280	69	79
113*	462	LV10	2	4							480	410	520	n.d.										
112*	462	LV10	1	9							180	110	357	58										
79*	81	LV10	1	10			130	220	490	270	1100	380	<130	n.d.			1.0	0.8			6.5	1	40	16
135	251	LV1	1	7							9.0	6.2	210	n.d.										
134	251	LV10	4	12							3.8	3.0	240	88										
133	251	LV10	1	33			64	n.d.	2400	1500	230	180	260	79			9.3	13			37	36	3.6	3.9
128*	251	LV10	3	6			64	84	5800	n.d.	29	n.d.					2.3	2.2			1.9	1.3	1.9	n.d.
127*	251	LV10	2c	14			36	20	1200	710	20	n.d.					1.7	n.d.			6.0	n.d.	0.5	1.0
Hematite-aluminosilicate clast replacement																								
122*	505	LV10oS	1	6	42000	2020	110	112	2800	3500	6000	5440					1.1	n.d.	92	83	49	40	2.0	2.7

Abbreviations	ID: Unique identification number for the fluid inclusion assemblage (FIA) used in this study
	n: Numbers of fluid inclusions measured in this assemblage
	n.d. not determined, <: indicating the limit of detection, h.t. heterogeneous trapping

Table A4b. Average elemental composition of fluid inclusion assemblages in veins cross-cutting the hematite breccia body determined by LA-ICP-Q-MS and microthermometry. Data is ordered according to sample-type, inclusion-subtype and decreasing Na-content. Concentrations in ppm.

ID	Sample	Type	FIA-No	n	Na	±	S	±	Cl	±	K	±	Ca	±	Mn	±	Fe	±	Cu	±	Br	±	Cs	±	Pb	±	U	±
Siderite + quartz + fluorite + chalcopyrite veins																												
29	15.1	LH5HS	4	4	110000	3400	<15000	n.d.			19000	14500	35000	4700	2100	1400	47000	2400	71	n.d.			71	58	760	440	<3.4	n.d.
28	15.1	LH5HS	2	3	190000	n.d.	<2100	n.d.			16000	n.d.	36000	n.d.	<1100	n.d.	<13000	n.d.	440	n.d.			49	12	1400	620	<12	n.d.
65	15.2	LH5HS	2	12	110000	1800	<30000	n.d.			23000	10200	36000	480	990	700	17000	19500	97	83			91	45	1500	400	0.8	0.8
27	15.1	LH5HS	1	5	110000	1500	8100	n.d.			15000	5170	37000	540	890	410	23000	8630	170	55			57	10	100	270	<2.3	n.d.
67	17	LH5HS	4	6	100000	2000	<680	n.d.			18000	2420	48000	2600	690	280	16000	14000	65	59			90	38	1300	720	1.0	0.7
64	17	LH5HS	1	6	110000	1700	6500	n.d.			16000	4300	36000	1300	820	260	14000	6100	42	21			83	n.d.	1600	250	<0.2	n.d.
66	15	LV40	1	6	6400	790	<720	n.d.			2800	2130			110	84	6600	6200	61	95			5.0	2.5	83	45	<0.2	n.d.
Calcite + barite + pyrite + fluorite veins																												
16	27	LV10S	13	3	54000	470	<11000	n.d.			3600	n.d.	50000	530	1400	n.d.	5400	n.d.	130	73			3.3	n.d.	35	35	1.1	n.d.
14	27	LV10S	11	4	45000	7500	390	n.d.			7300	1700	62000	9400	230	12	200	n.d.	4.6	0.1			3.9	0.7	6.0	2.3	<0.9	n.d.
18	27	LV10S	16	4	40000	1400	<1500	n.d.			8800	5000	68000	1600	62	36	1300	n.d.	51	67			12	4.3	120	57	<0.5	n.d.
12	27	LV10S	6	5	44000	5900	<2600	n.d.			3600	n.d.	63000	7700	410	n.d.	<1700	n.d.	210	19			3.0	n.d.	<10	n.d.	<1.3	n.d.
20	27	LV10S	20	1	41000	670	<3000	n.d.			5100	n.d.	65000	800	<140	n.d.	<1600	n.d.	120	n.d.			9.6	n.d.	71	n.d.	<1.8	n.d.
17	27	LV10S	15	3	41000	n.d.	<15000	n.d.	33000	33000	1700	1700	65000	n.d.							820	290	35	12				
13	27	LV10S	7	2	41000	1600	<2900	n.d.			3900	310	67000	2200	290	n.d.	<1700	n.d.	73	n.d.			14	0.7	100	21	<1.4	n.d.
11	27	LV10S	5	2	40000	1100	<500	n.d.			6400	n.d.	63000	1300	450	n.d.	<120	n.d.	<2	n.d.			7.7	3	100	n.d.	<0.1	n.d.
10	27	LV10S	3	10	37000	540	14000	12000	170000	63000	7700	3500	69000	500	640	120	1700	n.d.	1300	860	850	1000	13	12	140	27	22	n.d.
15	27	LV10S	12	1	36000	250	<7900	n.d.			<4400	n.d.	74000	460	<390	n.d.	<4700	n.d.	<94	n.d.			<11	n.d.	<26	n.d.	<5.5	n.d.
19	27	LV10S	17	2	34000	4600	<50	n.d.			6000	190	66000	5900	180	210	<22	n.d.	0.9	0.1			6.9	0.3	73	38	0.0	n.d.
52	82	LV10S	9	5	37000	5900	<800	n.d.	200000	41200	2000	300	61000	7400							1800	650	2.8	1.3				
49	82	LV10S	7	2	35000	780	<1400	n.d.			3600	n.d.	78000	8900	330	390			30	n.d.			2.3	n.d.	37	25	2.1	n.d.
32	82	LV10S	2	1	34000	2300	<360	n.d.			5000	n.d.	66000	3200	<18	n.d.	<230	n.d.	6.5	n.d.			4.4	n.d.	13	n.d.	<0.3	n.d.
53	82	LV10S	8	4	34000	2700	<360	n.d.			6400	800	64000	3800	160	250	630	n.d.	21	5.0			4.6	1.2	20	18	15	8
44	82	LV10S	BrCl	5	34000	n.d.	44000	n.d.	200000	90000	3900	580	65000	n.d.							900	1100	4.8	1.5				
30	82	LV10S	1	11	34000	2600	14000	18000	140000	23000	4000	1600	64000	2600	7	n.d.	13000	18000	4.3	n.d.	390	25	3.5	1.4	86	160	1.6	2.2
40	82	LV10S	6	5	34000	3700	<2700	n.d.			2900	n.d.	60000	6600	420	500	4600	4900	230	310			3.1	1.8	23	23	17	n.d.
47	82	LV10S	5	3	33000	3600	<1400	n.d.			4300	310	66000	5300	460	n.d.	550	n.d.	31	n.d.			4.3	0.8	32	21	0.7	n.d.
35	82	LV15	1	3	55000	14000	<8600	n.d.			<5400	n.d.	41000	16000	<450	n.d.	19000	n.d.	330	150			<6.0	n.d.	40	7	8.8	5.2
59	82	LV15	3	4	36000	2100	<2000	n.d.			3900	360	64000	3500	130	25	<1600	n.d.	<30	n.d.			4.3	1.0	<10	n.d.	<1.4	n.d.
55	82	LV20S	11	10	36000	5600	180	n.d.	160000	18700	2000	1700	62000	7100	2100	2200	10000	3700	170	170	310	180	5.5	3.1	39	35	3.6	3.8
58	82	LV20S	12	6	36000	3200	10000	n.d.			3700	770	65000	4200	590	140	6300	5800	400	340			7.2	3.4	52	31	3.8	2.9
42	82	LV20S	9	4	34000	1600	2900		2800		5900	640	64000	3100	160	71	480	280	78	94			4.8	2.5	21	10	1.4	0.2
41	82	LV20S	8	2	33000	5400	<300	n.d.			4800	1400	68000	7400	63	n.d.	<190	n.d.	170	n.d.			5.6	3.7	3		<1.1	n.d.
34	82	LV20S	5	1	27000	1000	<5300	n.d.			<3400	n.d.	71000	1600	<270	n.d.	<3400	n.d.	110	n.d.			<4.6	n.d.	<13	n.d.	<3.0	n.d.
60*	82	LV30S	Cp2	6	39000	4100	<1500	n.d.			7400	2800	60400	5500	1800	2400	6200	3600	100	150			4.4	n.d.	93	80	30	n.d.
56*	82	LV30S	Cp1	6	36000	3300	33000	n.d.			4500	n.d.	65000	4800	1200	1600	<3400	n.d.	1200	750			8.4	6.9	22	16	7.8	n.d.
46	82	LV30S	4	6	35000	410	4000	n.d.			6200	1700	65000	1700	130	99	3500	1600	310	230			6.3	2.3	26	25	4.5	4.3

Table A4b. *(Continued)*

ID	Sample	Type	FIA-No	n	Na	±	S	±	Cl	±	K	±	Ca	±	Mn	±	Fe	±	Cu	±	Br	±	Cs	±	Pb	±	U	±
Calcite + barite + pyrite + fluorite veins																												
45	82	LV30S	3	4	**33000**	n.d.	**<340**	n.d.	**140000**	68400	**3700**	680	**69000**	n.d.							**330**	250	**3.0**	0.7				
33	82	LV30S	1	2	**32000**	2900	**<140**	n.d.			**3200**	n.d.	**71000**	5600	**<70**	n.d.	**<800**	n.d.	**<17**	n.d.			**<1.3**	n.d.	**<2.0**	n.d.	**<0.6**	n.d.
36	82	LV30S	2	10	**31000**	2100	**2200**	2700	**190000**	102800	**7200**	4300	**72000**	2800	**480**	n.d.	**6500**	1200	**480**	88	**680**	240	**6.6**	4	**46**	63	**<5.0**	n.d.
50	82	LV40	2	3	**77000**	16000	**6100**	n.d.			**8400**	3300	**24000**	17000	**<240**	n.d.	**<3250**	n.d.	**61**	n.d.			**15**	n.d.	**39**	n.d.	**<3.0**	n.d.
51	82	LVoS X	2 h.t.	4	**39000**	23000	**2100**	n.d.			**9600**	5000	**12000**	7100	**280**	330	**25000**	4700	**1600**	1700			**5.7**	4.7	**13**		**5.2**	3.1
43	82	LVoS X	1 h.t.	15	**27000**	4000	**17000**	34000			**2900**	1200	**40000**	8000	**38**	31	**24000**	46000	**1100**	2780			**3.0**	1.8	**46**	86	**9.5**	9.3
48	82	LVoS U	1 h.t.	3	**21000**	9900	*h.t.*	*n.d.*			**4600**	n.d.			**9100**	n.d.	*h.t.*	*n.d.*	**1100**	n.d.			**<2.4**	n.d.	**1400**	1200	*h.t.*	*n.d.*
3	98	LV10S	1	6	**60000**	1700	**<700**	n.d.			**5200**	3000	**42000**	1800	**180**	n.d.	**2100**	340	**26**	9			**4.9**	2.3	**30**	12	**0.9**	0.6
2	98	LV15	1	3	**40000**	2000	**<2000**	n.d.			**5400**	n.d.	**54000**	2800	**390**	n.d.	**<830**	n.d.	**39**	n.d.			**6.6**	n.d.	**94**	n.d.	**<1.0**	n.d.
7	98	LV5	1	2	**26000**	2400	**<400**	n.d.			**<290**	n.d.	**12000**	1200	**<10**	n.d.	**<250**	n.d.	**4.0**	n.d.			**0.7**	n.d.	**1.2**	n.d.	**0.7**	n.d.
9	98	LV5	3	2	**22000**	2200	**<500**	n.d.			**200**	n.d.	**15000**	920	**<15**	n.d.	**1300**	n.d.	**<15**	n.d.			**10**	n.d.	**240**	n.d.	**0.4**	n.d.
Magnetite + quartz vein																												
68	50	LH5H	4	6	**120000**	3100	**<23000**	n.d.			**22000**	17000	**50000**	1300	**3400**	2300	**23000**	16000	**110**	n.d.			**7.3**	n.d.	**200**	70	**<3.0**	n.d.
69	50	LH5H	1	6	**120000**	1700	**18700**	18900			**31000**	7100	**50000**	1100	**4300**	3200	**74000**	77000	**5400**	6900			**31**	15	**1510**	640	**<1.2**	n.d.
75	50	LV1	1	3	**78000**	2700	**<4100**	n.d.			**10000**	1900	**24000**	2900	**950**	530	**<1500**	n.d.	**110**	n.d.			**5.6**	n.d.	**162**	83	**3.4**	n.d.
71	50	LV5	2	5	**84000**	1500	**<1000**	n.d.			**940**	n.d.			**420**	240	**3600**	1200	**180**	n.d.			**18**	27	**480**	520	**11**	13
70	50	LV5	1	3	**7500**	920	**<600**	n.d.			**3400**	n.d.			**370**	400	**410**	n.d.	**120**	n.d.			**6.0**	n.d.	**24**	33	**<0.2**	n.d.
73	50	LV5H	3	5	**140000**	2800	**4200**	n.d.			**18000**	12000	**22000**	4600	**1200**	1100	*h.t.*	n.d.	**630**	220			**8.8**	5.6	**5700**	7300	**1.5**	n.d.
74	50	LV5H	2	4	**130000**	n.d.	**<20000**	n.d.			**22000**	19000	**47000**	n.d.	**12000**	12000	**45000**	10000	n.d.				**200**	160	**9300**	7200	**<3.5**	n.d.
76	50	LV5HSS	1	6	**100000**	3000	**<19000**	n.d.			**61000**	22000	**57000**	1200	**26000**	15000	**73000**	66000	**1600**	2200			**250**	260	**5500**	3100	**<3.0**	n.d.

Abbreviations   ID: Unique identification number for the fluid inclusion assemblage (FIA) used in this study
n: Numbers of fluid inclusions measured in this assemblage
n.d. not determined, <: indicating the limit of detection, h.t. heterogeneous trapping